AGU PUBLICATIONS

JGR

Journal of Geophysical Research: Solid Earth

RESEARCH ARTICLE

10.1002/2016JB013457

Key Points:
- 1936 academic and industrial seismic surveys from oceanic crust have been analyzed
- Oceanic residual depth anomalies have wavelengths of thousands of kilometers and amplitudes of ±1 km
- Correlation with gravity anomalies, magmatism, and seismic tomography imply convective origin

Supporting Information:
- Supporting Information S1
- Data Set S1
- Data Set S2
- Data Set S3
- Data Set S4
- Data Set S5
- Data Set S6
- Data Set S7
- Data Set S8
- Data Set S9
- Data Set S10
- Data Set S11
- Data Set S12
- Data Set S13
- Data Set S14

Correspondence to:
M. J. Hoggard,
mjh217@cam.ac.uk

Citation:
Hoggard, M. J., J. Winterbourne, K. Czarnota, and N. White (2017), Oceanic residual depth measurements, the plate cooling model, and global dynamic topography, *J. Geophys. Res. Solid Earth*, *122*, 2328–2372, doi:10.1002/2016JB013457.

Received 11 AUG 2016
Accepted 26 JAN 2017
Accepted article online 30 JAN 2017
Published online 15 MAR 2017
Corrected 1 MAY 2017

This article was corrected on 1 MAY 2017. See the end of the full text for details.

Oceanic residual depth measurements, the plate cooling model, and global dynamic topography

Mark J. Hoggard[1], Jeff Winterbourne[2], Karol Czarnota[3], and Nicky White[1]

[1]Department of Earth Sciences, Bullard Laboratories, Cambridge, UK, [2]BP Exploration Operating Co. Ltd, Middlesex, UK, [3]Geoscience Australia, Canberra, ACT, Australia

Abstract Convective circulation of the mantle causes deflections of the Earth's surface that vary as a function of space and time. Accurate measurements of this dynamic topography are complicated by the need to isolate and remove other sources of elevation, arising from flexure and lithospheric isostasy. The complex architecture of continental lithosphere means that measurement of present-day dynamic topography is more straightforward in the oceanic realm. Here we present an updated methodology for calculating oceanic residual bathymetry, which is a proxy for dynamic topography. Corrections are applied that account for the effects of sedimentary loading and compaction, for anomalous crustal thickness variations, for subsidence of oceanic lithosphere as a function of age and for non-hydrostatic geoid height variations. Errors are formally propagated to estimate measurement uncertainties. We apply this methodology to a global database of 1936 seismic surveys located on oceanic crust and generate 2297 spot measurements of residual topography, including 1161 with crustal corrections. The resultant anomalies have amplitudes of ±1 km and wavelengths of ~1000 km. Spectral analysis of our database using cross-validation demonstrates that spherical harmonics up to and including degree 30 (i.e., wavelengths down to 1300 km) are required to accurately represent these observations. Truncation of the expansion at a lower maximum degree erroneously increases the amplitude of inferred long-wavelength dynamic topography. There is a strong correlation between our observations and free-air gravity anomalies, magmatism, ridge seismicity, vertical motions of adjacent rifted margins, and global tomographic models. We infer that shorter wavelength components of the observed pattern of dynamic topography may be attributable to the presence of thermal anomalies within the shallow asthenospheric mantle.

1. Introduction

Elevation of the Earth's surface is principally maintained by thickness and density variations within the crust and lithospheric mantle [*Pratt*, 1855; *Airy*, 1855]. Thus, mountain ranges are isostatically supported by deep crustal roots, while thin crust underlies many depressed regions such as sedimentary basins. However, some component of topography and bathymetry is generated and maintained by the changing pattern of convective circulation within the underlying mantle [*Pekeris*, 1935]. Upwellings and downwellings elevate or depress the surface of the overlying lithosphere [*Griggs*, 1939]. This time-dependent dynamic topography has been defined in a range of different ways. Here we define dynamic topography as that component of vertical surface deflection which is generated by density variations and flow within the convecting mantle. The spatial and temporal distribution of this dynamic topography can be used to place constraints on the fluid dynamical properties of the convecting mantle.

Our understanding of convection within the Earth has developed substantially over the last 100 years. The Rayleigh number of the Earth is estimated to be 10^6–10^9, which implies that the mantle convects vigorously with a time-dependent planform [*Knopoff*, 1964; *Turcotte and Schubert*, 2002]. Numerical experiments of mantle convection predict a wide range of features, including long-lived stationary plumes, transient sheets, and rolls as well as single or many layers of convective circulation [e.g., *McKenzie et al.*, 1973; *Yuen et al.*, 1994; *Davies and Davies*, 2009]. Consequently, dynamic topography can be expected to vary as a function of time and space. These variations ought to be manifest throughout the geological record—an important challenge is to identify and quantify these transient features.

Our knowledge of the present-day planform of mantle convection is limited by a paucity of observational databases. Mapping dynamic topographic anomalies is complicated by the need to correct for isostatic

elevation generated by thickness and density contrasts within the crust and lithospheric mantle [*Flament et al.*, 2013]. Continental lithospheric architecture is heterogeneous as a result of protracted geological histories that give rise to a range of thermal and chemical changes [*Jordan*, 1975]. One particularly important issue is the variable degree of depletion of cratonic lithosphere caused by a cumulative history of previous melting events. Fortunately, oceanic lithosphere appears to be significantly simpler, providing a more secure setting within which dynamic topography can be unambiguously identified and accurately measured. Oceanic bathymetry is primarily characterized by increasing subsidence with age that is caused by cooling and thickening of the lithospheric plate [*McKenzie*, 1967]. This behavior is globally consistent and predictable, so that deviations from it provide useful insights into other potential mechanisms of bathymetric evolution.

Menard [1965] suggested that since mantle convection is transient, resultant vertical motions should continuously evolve through space and time. He identified prominent midplate rises, such as the Darwin Rise in the southwest Pacific Ocean, as important present-day surface expressions of this transient phenomenon [*Menard*, 1969]. Oceanic bathymetry can also be regionally modulated by isostatic responses to sedimentary loading, by crustal thickness variations, and by flexural effects adjacent to subduction zones and seamounts [*Watts and Ribe*, 1984]. Removal of these isostatic and flexural responses, as well as the age-depth trend, yields a distribution of residual "depth anomalies" that define the pattern of dynamic topography, a term first coined by *Menard* [1973]. It is important to note that, in practice, residual depth anomalies represent an upper limit for the amplitude of dynamic topography, since local variations in the thickness and density of the lithospheric mantle are not yet resolvable and so are neglected.

Classic residual depth studies focused on the central portions of substantial oceanic basins as a result of significant uncertainties in sediment thickness adjacent to continental margins. Corrections for sediment loading assumed Airy isostasy and constant sediment density, but a correction for anomalous crustal thickness was not applied. Depth anomalies of $\pm$300 m within the East Pacific Ocean, which occur on length scales of 500–2000 km, were found to be more common than hotspot volcanism and showed a weak correlation with free-air gravity anomalies [*Menard*, 1973]. A global analysis by *Cochran and Talwani* [1977] confirmed these observations and noted positive anomalies >500 m within the North Atlantic Ocean, in the vicinity of Hawaii, and near the Rio Grande, Azorean, and Kerguelen rises. Depressions deeper than −500 m were mapped along the East Pacific Rise and at the Australia-Antarctic Discordance.

Isostatic corrections in regions with thicker sedimentary cover were subsequently addressed by accounting for differential compaction, which causes increases in density and acoustic velocity as a function of depth through the sedimentary pile [*Le Douaran and Parsons*, 1982; *Tucholke et al.*, 1982; *Crough*, 1983a; *Carlson et al.*, 1986]. Residual depths were later refined for the Pacific Ocean [*Schroeder*, 1984], the southeast Indian Ocean, and the South Atlantic Ocean [*Hayes*, 1988], culminating in a preliminary global analysis [*Cazenave et al.*, 1988]. These studies confirmed the existence of $\pm$1 km anomalies on length scales of 500–2500 km. Table 1 collates known oceanic residual depth studies.

A significant and enduring problem with the accuracy and interpretation of residual topographic anomalies concerns the general omission of the crustal correction [*Cazenave et al.*, 1986; *Lecroart et al.*, 1997; *Flament et al.*, 2013]. For example, substantial positive anomalies were mapped in regions where large crustal thicknesses are now known to occur (e.g., Rio Grande Rise and Ontong Java Plateau). Since there is a relative paucity of well-resolved crustal thickness measurements within the oceanic realm, initial attempts to sidestep this problem were based on excising regions of anomalous crustal thickness with the aid of bathymetric databases and high-pass-filtered gravity anomalies [*Hillier and Watts*, 2005; *Crosby et al.*, 2006; *Zhong et al.*, 2007]. More recently, isostatic corrections have been used to account for anomalous crustal thicknesses at spot locations where seismic wide-angle and reflection imaging permits direct measurement [*Winterbourne et al.*, 2009; *Czarnota et al.*, 2013; *Winterbourne et al.*, 2014].

In this contribution, our aims are threefold. First, we present an updated methodology that includes a comprehensive treatment of error propagation associated with each correction. Second, an augmented global database of 2297 residual depth measurements relative to a revised plate model is presented. Previously, many of these measurements were utilized as the basis of a spectral analysis of dynamic topography [*Hoggard et al.*, 2016]. Since this study, our digital database has been significantly updated and, where necessary, corrected. We subsequently describe a series of regional examples which illustrate how residual depth measurements can be corroborated with independent and disparate geological and geophysical observations.

Table 1. Summary of Locations, Methodologies, and Corrections for Oceanic Residual Depth Studies[a]

Reference	Location	Age-Depth Model	Sediment Correction
Menard [1973]	East Pacific	Plate	Constant density
Cochran and Talwani [1977]	Global (basin centers)	Plate-like	Constant density
Heestand and Crough [1981]	North Atlantic	Half-space	Constant density
Crough and Jarrard [1981]	Central Pacific	Plate	Compaction
Crough [1983b]	Global (basin centers)	Plate	Compaction
Schroeder [1984]	Pacific	Plate	Compaction
Watts et al. [1985a]	Pacific	Plate	Not applied
Cazenave et al. [1986]	Global	Plate	Not applied
McNutt and Fischer [1987]	South Pacific	Plate	Compaction
Hayes [1988]	SE Indian and South Atlantic	Half-space	Compaction
Cazenave et al. [1988]	Global	Plate	Compaction
Colin and Fleitout [1990]	Global	Plate-like	Compaction
Cazenave and Lago [1991]	Global	Half-space	Compaction
Johnson and Carlson [1992]	Global DSDP and ODP sites	Plate	Compaction
Forte et al. [1993]	Global	Not applied	Not applied
Davies and Pribac [1993]	Pacific	Half-space	Compaction
Kido and Seno [1994]	Global	Plate-like	Compaction
Nyblade and Robinson [1994]	Africa	Plate and half-space	Compaction
Le Stunff and Ricard [1995]	Global	Plate-like	Constant density
Hohertz and Carlson [1998]	Argentine Basin	Half-space	Compaction
Lithgow-Bertelloni and Silver [1998]	South Atlantic	Half-space	Not Applied
Pari and Peltier [2000]	Global	Not applied	Crust 5.1 densities
Panasyuk and Hager [2000]	Global	Plate and half-space	Not applied
Pari [2001]	Global	Not applied	Crust 5.1 densities
Steinberger et al. [2001]	Global	Plate-like	Crust 5.1 densities
Kaban et al. [2003]	Global	Plate	Crust 5.1 densities
Louden et al. [2004]	North Atlantic	Plate	Compaction
Hillier and Watts [2005]	North Pacific	Plate	Compaction
Crosby et al. [2006]	Global	TBL instability	Compaction
Steinberger [2007]	Global	Plate like	Crust 2.0 densities
Zhong et al. [2007]	Pacific	Plate and Half-space	Compaction
Ito and van Keken [2007]	Global	Plate	Applied (compaction unclear)
Müller et al. [2008a]	Global	Plate and TBL instability	Compaction
Winterbourne et al. [2009]	Central and South Atlantic	TBL instability	Compaction
Crosby and McKenzie [2009]	Global	TBL instability	Compaction
Whittaker et al. [2010]	SE Indian	Half-space	Compaction
Flament et al. [2013]	Global	Plate	Compaction
Czarnota et al. [2013]	Australia	TBL instability	Compaction
Winterbourne et al. [2014]	Global	TBL instability	Compaction
King and Adam [2014]	Global	Plate	Constant density
Wobbe et al. [2014]	South Pacific	Plate	Compaction
Steinberger [2016]	Global	Plate-like	Crust 1.0 densities
Hoggard et al. [2016]	Global	TBL instability	Compaction

[a]TBL = thermal boundary layer [e.g., *Crosby et al.*, 2006]. Plate cooling, plate-like (i.e., half-space cooling for young lithosphere followed by constant depth), and TBL instability relationships all flatten at older oceanic ages.

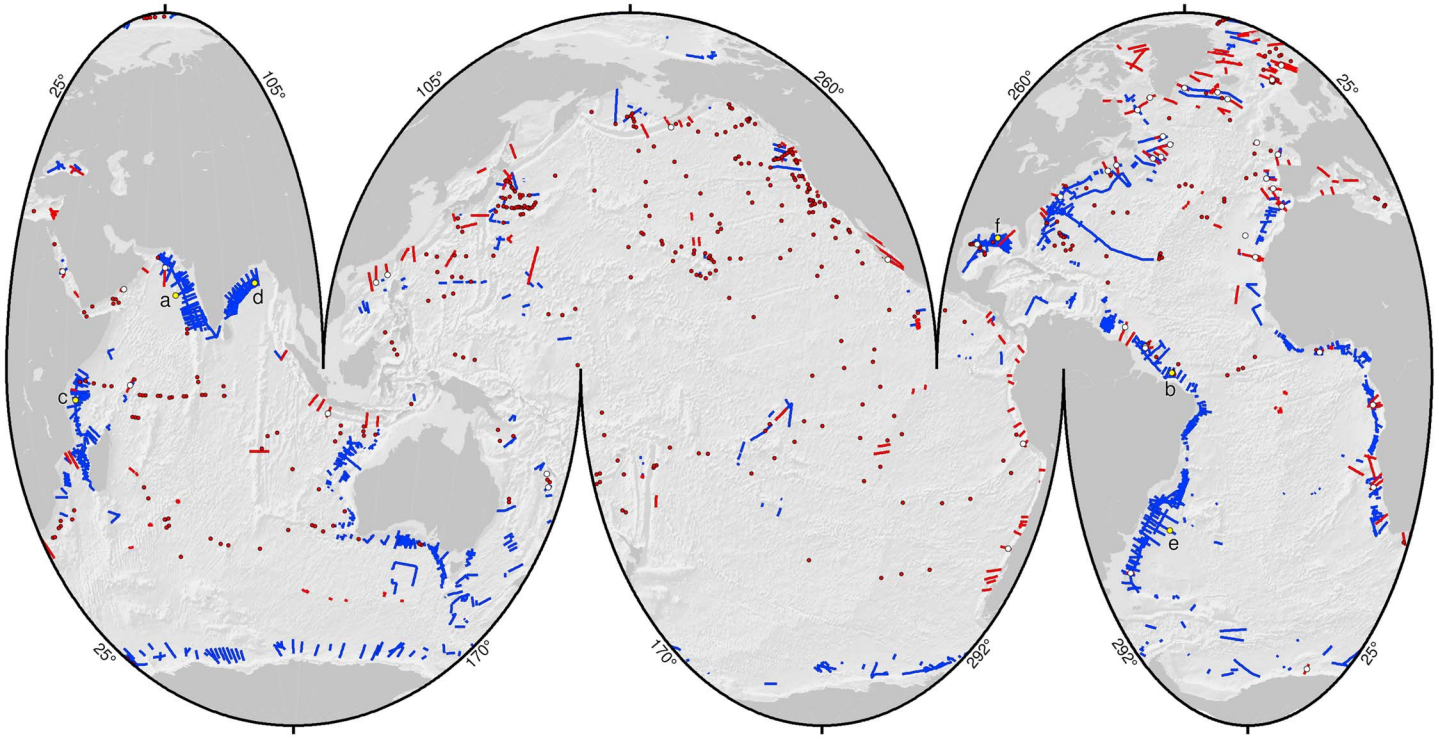

Figure 1. Seismic database collated in this study. Locations and sources are tabulated in the supporting information. Blue lines = 1240 reflection profiles. Red lines/circles = 302 waveform-modeled, wide-angle and 395 legacy slope-intercept, refraction experiments. Yellow circles = locations of six example seismic reflection images (Figure 2). White circles = 43 coincident wide-angle and reflection experiments used to constrain sedimentary acoustic velocities (Figure 4). Segmented Mollweide projection shaded with SRTM30-PLUS global bathymetry [*Becker et al.*, 2009].

Finally, a brief analysis illustrates the importance of our well-resolved spot measurements of oceanic residual depth for constraining the amplitude of the long-wavelength components of dynamic topography.

2. Oceanic Crust Database

Accurate knowledge of the thickness and density structure of oceanic crust is required in order to apply corrections for sedimentary and crustal loading. Such measurements can be locally obtained from seismic reflection and wide-angle experiments that image both basement and Moho. A database has been compiled that comprises 1240 reflection lines, 302 modern (i.e., waveform-modeled) wide-angle experiments, and 395 vintage (i.e., slope-intercept) refraction experiments (Figure 1). Data sources include vintage academic experiments and profiles acquired by the seismic contracting industry and are tabulated in the supporting information. These experiments and profiles range over more than 300,000 km and provide comprehensive coverage of the oceanic realm, particularly at thickly sedimented continental margins where accurate isostatic corrections are essential. There is inevitably a bias toward continental margins where the activities of the hydrocarbon industry are concentrated. Regions where flexural bending occurs or where large-amplitude, short-wavelength gravity anomalies are visible have been excluded.

On each image, *bona fide* oceanic crust is identified by its characteristic acoustic architecture in conjunction with the pattern of magnetic anomalies [*Müller et al.*, 2008a], with free-air gravity anomalies [*Sandwell et al.*, 2014], and with regional studies of continent-ocean boundaries. Figure 2 shows six examples from this global inventory. Generally, the sediment-basement interface is clearly visible. The base of the crust (i.e., Moho) often consists of a single bright reflection, marking the base of typically cross-hatched lower crustal reflectivity (e.g., Figure 2e). Sometimes, the Moho reflection is patchy or even invisible, particularly along margins with uneven bathymetry, thick sedimentary piles, or rugose sediment-basement interfaces.

The reliability of crustal models determined from seismic wide-angle and refraction surveys depends upon the vintage of the experiment and upon the modeling technique employed. Optimal results come from modern, densely sampled experiments where observed and calculated travel times, together with waveforms, are

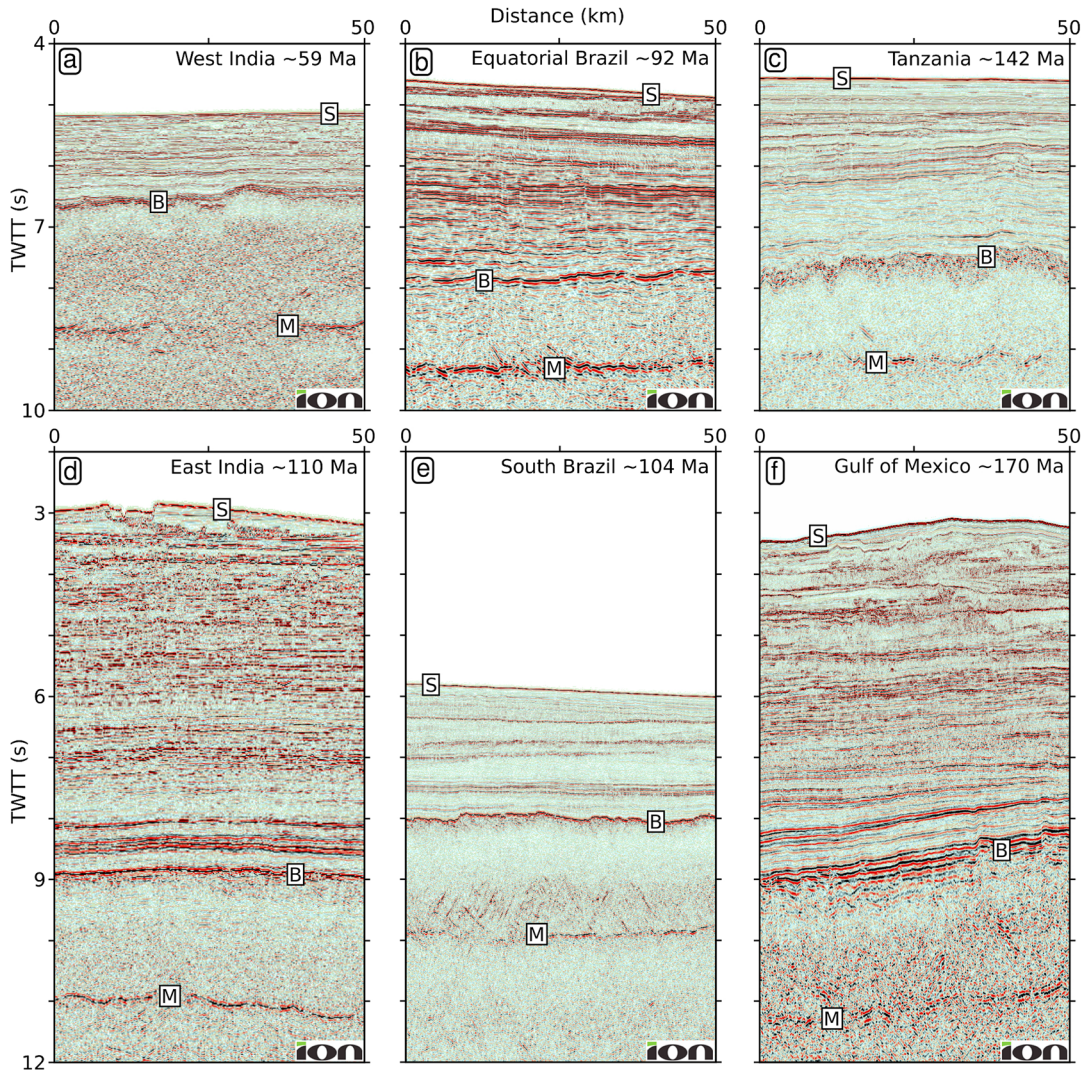

Figure 2. Images of oceanic crust. (a) Seismic reflection profile of 59 Ma oceanic crust west of India. S = seabed; B = sediment-basement interface; M = Moho discontinuity. (b) Equatorial Brazil (92 Ma). (c) Tanzania (142 Ma). (d) East India (110 Ma). (e) South Brazil (104 Ma). (f) Gulf of Mexico (170 Ma). Crustal ages from magnetic reversal history [*Müller et al.*, 2008a]. Approximate locations are shown in Figure 1. Seismic data are shown courtesy of ION Geophysical Corporation.

matched using either forward or inverse modeling [e.g., *Zelt and Smith*, 1992; *Holmes et al.*, 2008]. To ensure accurate Moho identification, it is essential that these wide-angle experiments have been reversed and that the horizontal range is large enough to observe diving waves that turn within the upper mantle (i.e., P_n phases). Older refraction experiments were generally analyzed using slope-intercept methods that typically underpredict true crustal thickness by ~20%, which results in underestimation of the crustal correction [*White et al.*, 1992].

3. Sedimentary Correction

To remove the effect of sedimentary loading, an isostatic correction is applied where the mass of sediment is replaced with an equivalent water load balanced by asthenospheric mantle (Figure 3). The sedimentary correction, C_s, is given by

$$C_s = \left(\frac{\rho_a - \overline{\rho_s}}{\rho_a - \rho_w} \right) z_s \tag{1}$$

where ρ_a is the density of the asthenosphere, ρ_w is the density of water, $\overline{\rho_s}$ is the average density of the sedimentary column, and z_s is the thickness of the sedimentary column (Table 2).

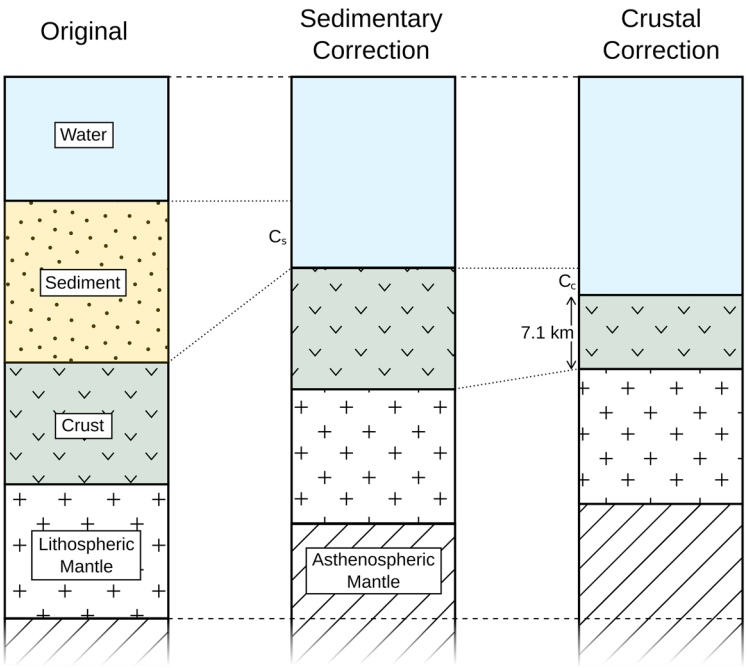

Figure 3. Isostatic balances for sedimentary and crustal corrections. Sedimentary correction, C_s, replaces sedimentary mass with equivalent mass of water and asthenospheric mantle. Crustal correction, C_c, replaces mass of oceanic crust with mass of reference 7.1 km of crust, water, and asthenospheric mantle. Columns not to scale.

Maps of sedimentary thickness are plentiful but of uncertain pedigree and variable accuracy. For example, global sedimentary thickness grids [e.g., *Laske and Masters*, 1997; *Divins*, 2003] have adequate spatial resolution but are prone to significant error where sedimentary deposits are thick, especially adjacent to continental margins or where there is significant basement topography (supporting information). Accurate measurements are best made when sediment-basement interfaces are imaged in seismic reflection or wide-angle experiments.

Seismic reflection profiles are recorded in two-way travel time which must be converted into thickness using a velocity model. The velocity model used here for the sedimentary pile is a revised version of that used by *Winterbourne et al.* [2009] that allows for compaction within the sedimentary pile. Two-way travel time, t, is related to the vertical acoustic velocity by

$$t = 2\int_0^z \frac{dz}{v(z)} \tag{2}$$

where $v(z)$ is the bulk velocity as a function of depth, z. This velocity depends upon the contributions from the pore space and from the solid grains, which are related in the time domain by

$$\frac{1}{v(z)} = \frac{\phi(z)}{v_w} + \frac{1-\phi(z)}{v_{sg}} \tag{3}$$

where v_w is the pore fluid velocity, v_{sg} is the solid grain velocity, and $\phi(z)$ is the porosity as a function of depth [*Wyllie et al.*, 1956]. An empirical function is used to parameterize the decrease of porosity as a function of depth given by

$$\phi(z) = \phi_\circ \exp\left(\frac{-z}{\lambda}\right) \tag{4}$$

where $\phi_\circ$ is the initial porosity and λ is the compaction decay length scale [*Athy*, 1930]. By combining these equations, we obtain

$$\frac{t}{2} = \frac{z}{v_{sg}} + \phi_\circ \lambda \left(\frac{1}{v_w} - \frac{1}{v_{sg}}\right)\left[1 - \exp\left(\frac{-z}{\lambda}\right)\right] \tag{5}$$

Table 2. Notation Table

Symbol	Description	Value	Units
C_s	Correction for sedimentary loading		km
C_c	Correction for crustal loading		km
z_s	Sedimentary thickness		km
z_c	Crustal thickness		km
z_w	Water depth		km
z_r	Zero age depth of oceanic crust		km
z_p	Lithospheric plate thickness		km
t	Two-way travel time		s
v_w	Acoustic velocity of water	1.50 ± 0.01	km s^{-1}
v_{sg}	Acoustic velocity of solid grains	5.50 ± 0.50	km s^{-1}
$\overline{v_c}$	Bulk acoustic velocity of oceanic crust	6.28 ± 0.34	km s^{-1}
ρ_w	Density of seawater	1.03 ± 0.01	Mg m^{-3}
$\overline{\rho_s}$	Bulk sediment density		Mg m^{-3}
ρ_{sg}	Density of solid grains	2.65 ± 0.05	Mg m^{-3}
$\overline{\rho_c}$	Mean density of oceanic crust	2.86 ± 0.03	Mg m^{-3}
ρ_a	Density of asthenospheric mantle	3.20 ± 0.02	Mg m^{-3}
$\rho_\circ$	Density of mantle at 0°C	3.30	Mg m^{-3}
α	Thermal expansivity	3×10^{-5}	$°C^{-1}$
κ	Thermal diffusivity	1×10^{-6}	m^2 s^{-1}
ϕ	Fractional porosity of sediment		dimensionless
$\phi_\circ$	Initial porosity of sediment	0.61	dimensionless
λ	Compaction decay length scale	3.9	km

A set of intersections between seismic reflection and refraction profiles provide the means to calibrate equation (5) since both thickness and two-way travel time for the sedimentary pile are known. Here a global distribution of 43 intersections is used to calibrate the velocity model shown in equation (5) by carrying out a parameter sweep through $\phi_\circ$-λ-v_{sg} space (Figure 1). Each $\phi_\circ$-λ-v_{sg} triplet yields a velocity relationship for which the root-mean-square (RMS) misfit is calculated with respect to the time-depth observations.

This simple analysis determines the optimal values of $\phi_\circ$ and λ, but it does not constrain v_{sg} (Figures 4b–4d). Since the principal constituents of abyssal sediments are quartz and clay minerals, laboratory-based solid grain velocity measurements can be exploited [e.g., *Christensen*, 1982]. A value of $v_{sg} = 5.5 \pm 0.5$ km s^{-1} embraces typical variations encountered within abyssal sedimentary piles. This value and its uncertainty have been incorporated within the sedimentary correction.

The smallest RMS misfit when $v_{sg} = 5.5$ km s^{-1} is 0.354 and yields a velocity model with $\phi_\circ = 0.61$ and $\lambda = 3.9$ km. Uncertainty is calculated by incrementally increasing the misfit value and selecting all $\phi_\circ$-λ combinations for $v_{sg} = 5.5$ km s^{-1} that have misfit values which fall beneath this threshold. The *t*-*z* curve for each combination was calculated using equation (5), and upper and lower bounds of the resultant velocity curves were determined. When 67% of the original time-depth sediment thickness observations fall within this envelope, the RMS misfit threshold reached is 0.434 (Figure 4).

Bulk sedimentary density, $\overline{\rho_s}$, also increases with compaction as it depends upon the relative contributions from fluid in the pore space and the solid grains.

$$\overline{\rho_s}(z) = \int_0^z \rho_w \phi(z) + \rho_{sg}[1 - \phi(z)]dz \tag{6}$$

where ρ_w is the density of water and ρ_{sg} is the solid grain density, which is assumed to be a mixture of quartz and clay (i.e., 2.65 ± 0.05 Mg m^{-3}) [*Christensen*, 1982]. By combining this relationship with equation (4), we obtain

$$\overline{\rho_s}(z) = \rho_{sg} + \frac{\phi_\circ \lambda}{z}(\rho_w - \rho_{sg})\left[1 - \exp\left(\frac{-z}{\lambda}\right)\right] \tag{7}$$

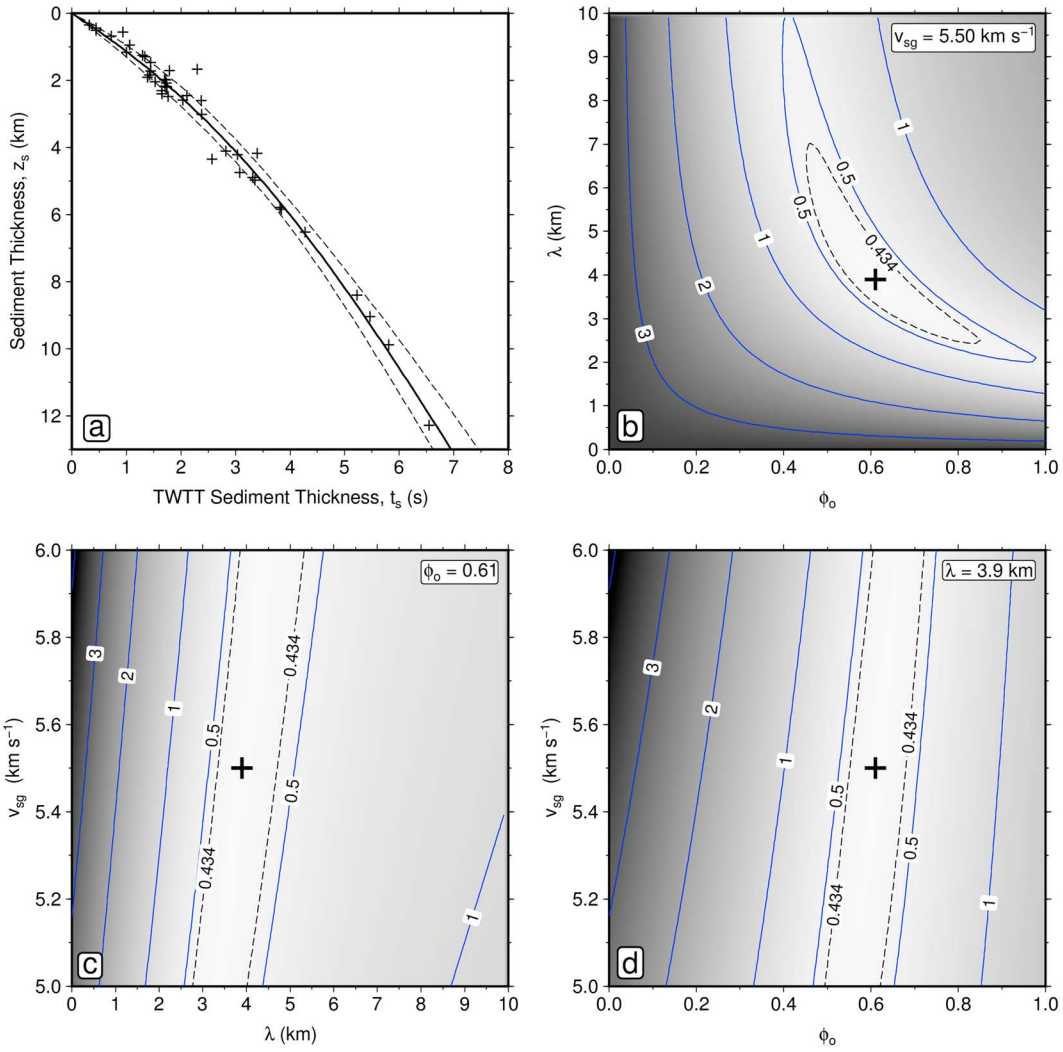

Figure 4. Sedimentary velocity and compaction. (a) Black crosses = 43 TWTT-depth pairs of sedimentary thickness from coincident reflection and wide-angle experiments (Figure 1). Solid/dashed lines = optimal velocity model with standard deviation (i.e., RMS misfit $\leq$0.434). (b) Misfit plotted as a function of $\phi_\circ$ and λ parameter sweep for v_{sg} =5.5 km s^{-1}. Black cross = global minimum at $\phi_\circ$ = 0.61 and λ = 3.9 km; dashed contour (0.434) = all $\phi_\circ$-λ pairs for v_{sg} = 5.5 km s^{-1} that yield adequate fit to 67% of TWTT-depth pairs. (c) Misfit plotted as a function of v_{sg} and λ for $\phi_\circ$ = 0.61. (d) Misfit plotted as a function of v_{sg} and $\phi_\circ$ for λ = 3.9 km. Note that optimal compaction parameters show weak dependence upon v_{sg}.

The previously obtained optimal compaction parameters are used. Cumulative errors arising from uncertainties in all variables used for the sedimentary correction are difficult to analytically propagate. Instead, a practical *Monte Carlo* approach was used in which the sedimentary correction is calculated 200 times by randomly sampling each parameter from a Gaussian distribution based on the mean and standard deviations given in Table 2. For each test, a selected value of v_{sg} is used to extract all corresponding $\phi_\circ$-λ combinations that yield misfit values which fall beneath the misfit threshold. In this way, uncertainties in compaction parameters, the densities of water, solid grains, and asthenospheric mantle together with uncertainties in the velocities of water and solid grains are propagated into the sedimentary correction. The results are shown in Figure 5 and are consistent with the more limited sedimentary loading corrections presented by *Crough* [1983a], *Sykes* [1996], and *Louden et al.* [2004].

This analysis has been used to calculate sedimentary thicknesses along each of the 1936 seismic experiments shown in Figure 1. The sedimentary correction was then applied to remove the effects of sedimentary loading. The resultant estimates have been averaged over 1° bins to yield 2297 individual measurements with associated uncertainties.

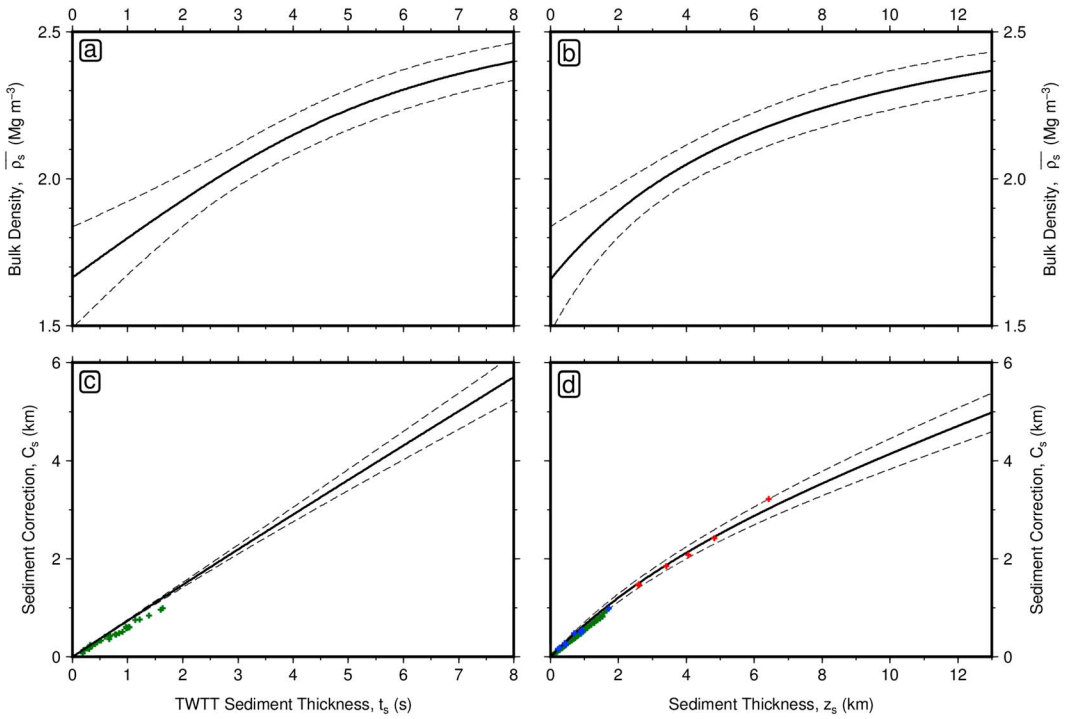

Figure 5. Sedimentary density and isostatic corrections. (a) Bulk sedimentary density plotted as a function of sediment TWTT using equation (7). Standard deviation arises from uncertainties in compaction parameters, velocities, and densities of water and solid grains. (b) Same plotted as a function of sediment thickness where standard deviation arises from compaction parameters and densities only. (c) Sedimentary correction plotted as a function of sediment TWTT using equation (1). Standard deviation includes uncertainties in all input parameters (Table 2). (d) Same plotted as a function of sediment thickness. Green crosses = corrections from *Crough* [1983a]; red crosses = corrections from *Louden et al.* [2004]; blue crosses = corrections from *Sykes* [1996] based upon observations from core samples only. Note that trade-off between sediment velocity and density reduces effect of compaction parameter uncertainty in Figure 5c compared to Figure 5d.

4. Crustal Correction

The crustal correction, C_c, concerns the isostatic replacement of crustal thickness that differs from a reference crustal thickness with an equivalent water load. Usually, observed crustal thickness is normalized with respect to the global average thickness of 7.1 km [*White et al.*, 1992]. The correction is given by

$$C_c = \left(\frac{\rho_a - \overline{\rho_c}}{\rho_a - \rho_w}\right)(z_c - 7.1) \tag{8}$$

where z_c and $\overline{\rho_c}$ are the thickness and average density of oceanic crust, respectively.

A reliable global database of oceanic crustal thickness does not currently exist. However, there are many local and regional studies which we have collated into a useful compilation. The principal challenge is to convert two-way travel time measurements into depth. The data sets analyzed here are mostly located along the oldest oceanic crust that abuts continental margins. The bulk acoustic velocity of oceanic crust does not appear to vary significantly with age after ~30 Ma since compaction and alteration of porosity within oceanic Layer 2 are complete by this time [*Carlson and Herrick*, 1990]. A bulk velocity of $\overline{v_c} = 6.28 \pm 0.34$ km s^{-1} is calculated from a compilation of velocity-depth profiles based upon waveform modeling of modern wide-angle experiments (supporting information). Figure 6 shows that there is, in fact, a small systematic increase in bulk velocity with age. Fortunately, this increase has only a minor effect on crustal thickness estimates since it represents a smaller source of uncertainty compared with the uncertainty in bulk velocity itself. The average density of oceanic crust estimated by *Carlson and Herrick* [1990] is 2.86 ± 0.03 Mg m^{-3}. This value is based upon analysis of core material from drilling programs, ophiolitic samples, and the observed seismic velocity structure of oceanic crust. Errors arising from uncertainties in the thickness and density of the crust and other isostatic parameters have been analytically propagated (Appendix A).

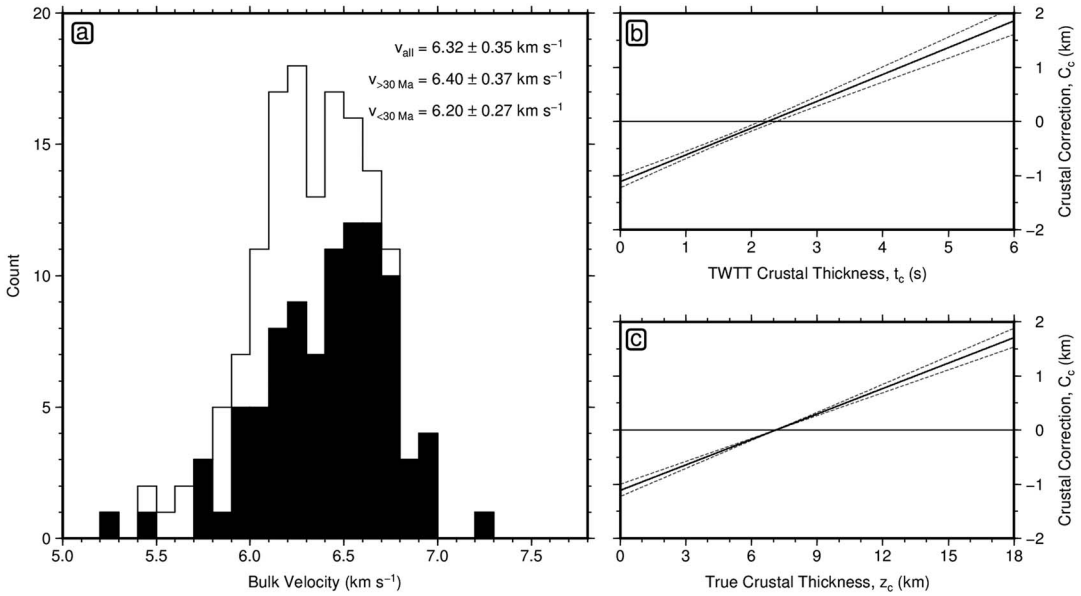

Figure 6. Crustal velocities and corrections. (a) Histogram of bulk velocities for oceanic profiles listed in the supporting information. Black polygon = crust >30 Ma; white polygon = crust <30 Ma; mean and standard deviation of each group is given in top right-hand corner. (b) Solid/dashed line = crustal correction plotted as a function of TWTT with 1σ standard deviation arising from uncertainties in velocity and density. (c) Solid/dashed line = crustal correction plotted as a function of true crustal thickness with 1σ standard deviation arising from uncertainty in density only.

This analysis is used to calculate and apply the crustal correction for 1161 measurements that have been averaged in 1° bins. However, there are seismic reflection profiles within our database upon which the Moho is either not visible or poorly imaged. In these cases, regional estimates, based upon adjacent profiles and upon the presence of seamounts or fracture zones, are used to gauge whether oceanic crust might be either thicker or thinner than the reference value. In this way, the sign of the crustal correction is estimated but not its magnitude. The median size of the crustal correction is 200 m, which is generally considerably smaller than the sedimentary correction. The non-crustal corrected residual topography estimates therefore still provide important and useful upper or lower bounds. In subsequent figures, circles are locations where both sedimentary and crustal corrections have been applied. Upper and lower limits are represented as downward and upward pointing triangles, respectively. An additional uncertainty of 200 m is added to all triangles to represent the absence of a local crustal correction. Finally, since vintage (i.e., slope-intercept) refraction analyses generally underpredict true crustal thickness, measurements based upon these data sets are represented with downward pointing triangles.

5. Age-Depth Correction

Many studies address the water-loaded depth of oceanic basement as a function of crustal age. Empirical relationships are estimated directly from global observational databases, while theoretical relationships are usually based upon conductive cooling of either half-space or plate models [e.g., *Parsons and Sclater*, 1977; *Stein and Stein*, 1992; *Crosby et al.*, 2006]. Here we revisit this well-known and debated topic using our new database of water-loaded basement depths corrected for sedimentary and crustal loading. In order to correct for subsidence as a function of time, oceanic crustal ages have been assigned to each observation. We use ages calculated from the global synthesis of *Müller et al.* [2008a]. Where necessary, this synthesis has been supplemented using additional regional studies of oceanic crustal ages (supporting information).

5.1. Empirical Relationships

Our previously published compilations of residual depth measurements exploited an empirical age-depth relationship derived from the observation-based analysis of *Crosby and McKenzie* [2009]. They used long-wavelength ($\lambda > 3000$ km) free-air gravity anomalies as a proxy to identify and remove significant dynamic topographic signals (see *Crosby et al.* [2006] for further details). In contrast to older age-depth studies, particular care was taken to remove contamination caused by crustal thickness variations. Oceanic plateaux

and regions with anomalously thin crust were identified using a combination of gravity anomalies and bathymetric maps and manually excised. Here we first repeat our previous approach and analyze our measurements using this published empirical relationship. The curve has been adjusted to remove discontinuities and to account for the effect of cooling by hydrothermal circulation at mid-oceanic ridges which tends to lower the temperature of the youngest crust [e.g., *Grose and Afonso*, 2013]. The corrected water-loaded depth to oceanic basement in meters, z_w, is given by

$$z_w(t) = \begin{cases} 2700 & 0 \le t < 1 \\ 2652 + 324\sqrt{t} & 1 \le t \le 73 \\ 5028 + 5.26t - 250 \sin\left(\frac{t-75}{30}\right) & 73 < t \le 156 \\ 5750 & t > 156 \end{cases} \quad (9)$$

where t is plate age in millions of years (Figure 7a). The majority of water-loaded depths to basement fall within ±1 km of this empirical relationship with a mean residual depth of −90 m and a standard deviation of ±710 m. Figure 7b shows an alternative empirical relationship that has been calculated using a 50 Ma Gaussian moving window. In this case, the mean residual depth is 0 m and the standard deviation is ±650 m.

5.2. Theoretical Relationships

Since our revised and augmented global database now consists of 2297 accurate spot measurements, it is both appropriate and desirable to revisit rival theoretical models that attempt to account for plate subsidence as a function of age. The two best-known descriptions are the half-space cooling model and the plate cooling model. The half-space cooling model neglects horizontal heat flow and solves the one-dimensional heatflow equation for vertical diffusion within a semi-infinite half-space [*Turcotte and Oxburgh*, 1969]. This calculation yields the temperature distribution within oceanic lithosphere as a function of age. This predicted behavior can be combined with thermal expansivity and isostasy to obtain an analytical solution for the water-loaded depth of ocean floor, z_w, as a function of age, t, such that

$$z_w(t) = z_r + \left[\frac{2\rho_\circ \alpha \Delta T \kappa^{\frac{1}{2}}}{(\rho_\circ - \rho_w)\pi^{\frac{1}{2}}}\right]\sqrt{t} \quad (10)$$

where z_r is the zero-age depth, $\rho_\circ$ is the density of mantle at surface temperature, α is the coefficient of thermal expansion, κ is the thermal diffusivity, and ΔT is the temperature difference between the surface and the mid-ocean ridge [*Turcotte and Schubert*, 2002]. z_r and $B = 2\rho_\circ \alpha \Delta T \kappa^{\frac{1}{2}}/(\rho_\circ - \rho_w)\pi^{\frac{1}{2}}$ can be independently varied to generate a parameter sweep through z_r-B space. The misfit, M, between water-loaded basement depth observations, z_w^{obs}, and the age-depth relationship, z_w^{model}, is given by

$$M = \frac{1}{N}\sum_{i=1}^{N}\left(z_w^{\text{obs}} - z_w^{\text{model}}\right)^2 \quad (11)$$

where N is the total number of observations. M is not weighted by uncertainties arising from the crustal and sedimentary corrections. This omission is important since some portions of oceanic floor may have negligible sedimentary cover and average crustal thickness, yielding negligible uncertainties in water-loaded basement depths. However, given that the effect of present-day dynamic topography has not been removed, it would be inappropriate to weight the age-depth relationship strongly in favor of these locations.

An optimal half-space cooling model is located at $z_r = 2.67$ km and $B = 284$ m Ma$^{-0.5}$ and has a residual misfit of $M = 0.460$ (Figures 8a and 9a). Using published values for constant parameters (Table 2), this value of B yields a ridge axis temperature of 1027°C, which is significantly smaller than the generally accepted value of ∼1330 ± 50°C that is consistent with the thickness and chemical composition of mid-oceanic ridge basalts (MORB) [e.g., *Klein and Langmuir*, 1987; *McKenzie and Bickle*, 1988; *White et al.*, 1992; *Herzberg et al.*, 2007; *Matthews et al.*, 2016]. On these grounds, we conclude that the half-space cooling model is inadequate.

We note that our retrieved value of $B = 284$ m Ma$^{-0.5}$ is significantly lower than previous estimates of B = 315–365 m Ma$^{-0.5}$ [e.g., *Parsons and Sclater*, 1977; *Stein and Stein*, 1992; *Korenaga and Korenaga*, 2008]. These previous estimates are larger because, in all three cases, a half-space cooling model was fitted to observations from young oceanic lithosphere (typically <70 Ma). By restricting our fitting procedure in the same way,

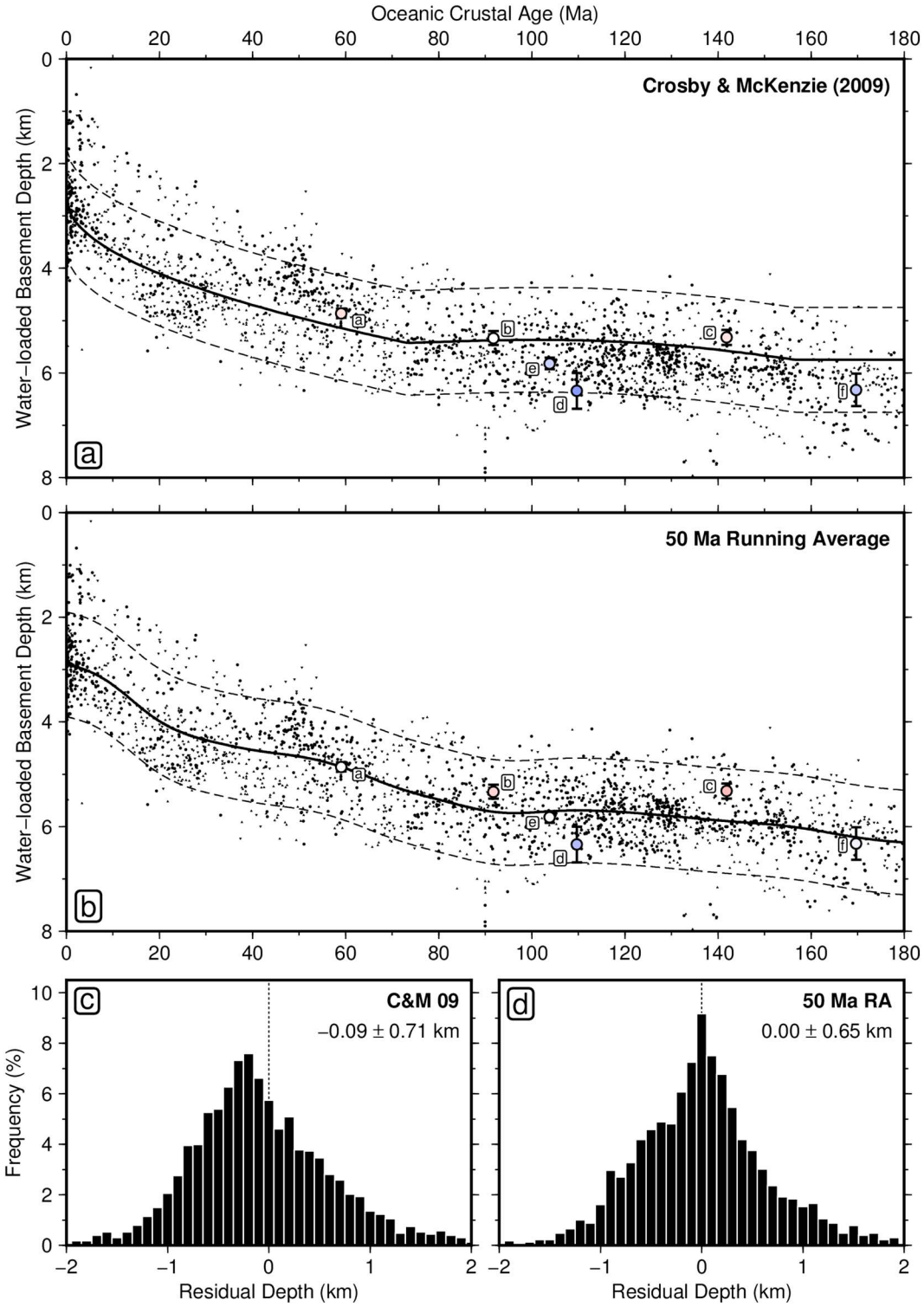

Figure 7. Empirical age-depth relationships. (a) Water-loaded basement depths averaged over 1° bins plotted as a function of age. Circles = 1161 depths corrected for sedimentary and crustal loading; upward/downward triangles = 1136 lower/upper bounds corrected for sedimentary loading only; solid/dashed lines = relationship of *Crosby and McKenzie* [2009] with ±1 km bounds; colored circles with error bars = six residual depth measurements made from profiles shown in Figure 2. (b) Water-loaded depths as before. Solid/dashed lines = 50 Ma Gaussian running average of age-depth measurements with ±1 km bounds. (c) Histogram, mean, and standard deviation of residual depths with respect to *Crosby and McKenzie* [2009] relationship. (d) Histogram, mean, and standard deviation of residual depths with respect to 50 Ma Gaussian running average.

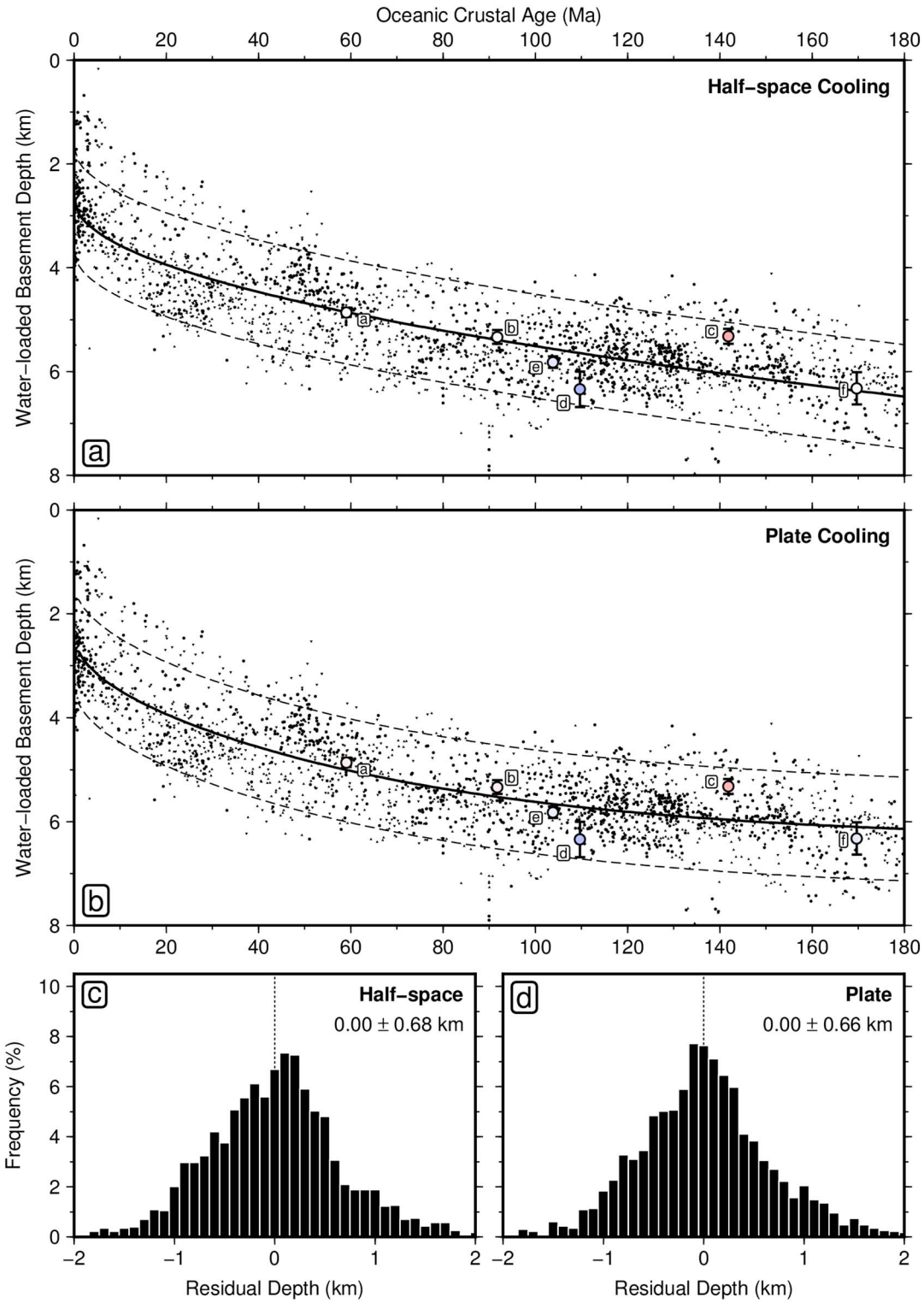

Figure 8. Theoretical age-depth relationships. (a) Water-loaded basement depths averaged over 1° bins plotted as a function of age. Circles = 1161 depths corrected for sedimentary and crustal loading; upward/downward triangles = 1136 lower/upper bounds corrected for sedimentary loading only; solid/dashed lines = best-fitting half-space cooling model with ±1 km bounds; colored circles with error bars = six residual depth measurements made from profiles shown in Figure 2. (b) Water-loaded depths as before. Solid/dashed lines = best-fitting plate cooling model with ±1 km bounds. (c) Histogram, mean, and standard deviation of residual depths with respect to half-space cooling model. (d) Histogram, mean, and standard deviation of residual depths with respect to plate cooling model.

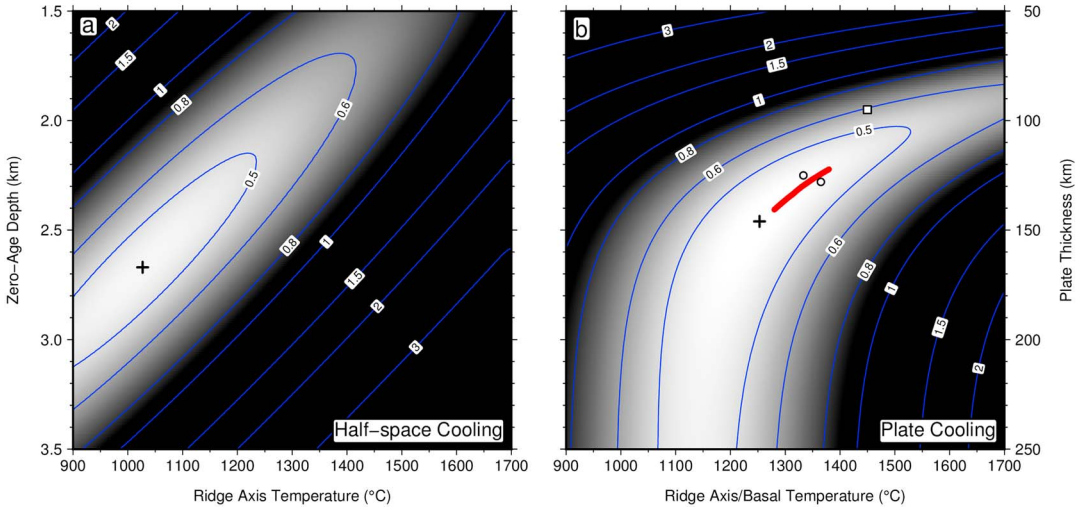

Figure 9. Half-space and plate cooling misfits. (a) Misfit, M, as a function of ridge axis temperature, ΔT, and zero-age depth, z_r, for half-space cooling model. Black cross = global minimum where $M = 0.460$. Values of other parameters are shown in Table 2. (b) M as a function of ridge axis/basal temperature, ΔT, and plate thickness, z_p, at zero-age depth, $z_r = 2.38$ km, for plate cooling model. Black cross = global minimum where $M = 0.442$; red line = misfit minima for mantle potential temperature range of 1330 ± 50°C, compatible with MORB geochemistry [*Herzberg and Asimow*, 2015; *Matthews et al.*, 2016]; white circles = plate models for the North Pacific and North Atlantic Oceans from *Parsons and Sclater* [1977]; white square = plate model obtained by *Stein and Stein* [1992].

we obtain $B = 330$ m Ma$^{-0.5}$, which agrees with this earlier work and corresponds to a ridge axis temperature of 1195°C. However, it is important to emphasize that the more crucial test of the half-space cooling model is whether or not it can be applied to a complete database of age-depth measurements. In this regard, the half-space cooling model fails.

The mismatch between predicted ridge axis temperature and that expected from basalt geochemistry suggests that a half-space cooling model is not a physically realistic description of subsidence as a function of age. This issue was originally resolved by introducing a plate model whereby the ridge axis temperature is also applied along the base of a lithospheric plate whose thickness is stabilized at ages greater than ~60 Ma by the onset of small-scale convective overturn or growth of a Rayleigh-Taylor instability in this thermal boundary layer [*McKenzie*, 1967; *Sclater and Francheteau*, 1970]. In this case, water-loaded depth as a function of time is given by

$$z_w(t) = z_r + \left(\frac{\rho_\circ \alpha \Delta T z_p}{2(\rho_\circ - \rho_w)}\right)\left[1 - \frac{8}{\pi^2}\sum_{n=0}^{\infty}\frac{1}{(1+2n)^2}\exp\left(\frac{-\kappa(1+2n)^2\pi^2 t}{z_p^2}\right)\right] \quad (12)$$

where z_p is the thickness of the lithospheric plate and n has integer values [*Turcotte and Schubert*, 2002]. This equation has four independent variables (i.e., z_r, $C = \frac{1}{2}\rho_\circ \alpha \Delta T/(\rho_\circ - \rho_w)$, κ, and z_p). In order to identify the optimal plate cooling model, we have calculated how the misfit between observed residual depths and this relationship varies as a function of these four variables. If $\kappa = 1 \times 10^{-6}$ m^2 s^{-1}, a global minimum misfit is identified by carrying out a parameter sweep through z_r-ΔT-z_p space with values of all other constants fixed (Table 2). A slice through ΔT-z_p space containing this global minimum is shown in Figure 8b. This minimum occurs at $z_r = 2.38$ km, $\Delta T = 1253$°C, and $z_p = 146$ km and has a misfit value of $M = 0.442$, which is similar to the minimum $M = 0.460$ for the half-space model.

The recovered value of z_p is consistent with surface wave tomographic models that show a pattern of age-dependent shear-wave velocity anomalies which die out below a depth of 150 km [e.g., *Priestley and McKenzie*, 2013]. The recovered value of ΔT is slightly smaller than independent estimates of $\sim 1330 \pm 50$°C derived from basalt geochemistry and oceanic crustal thickness measurements [*Herzberg and Asimow*, 2015; *Matthews et al.*, 2016]. However, it is crucial to emphasize that a negative trade-off exists between basal temperature and plate thickness. This trade-off indicates that $\Delta T = \sim 1330 \pm 50$°C yields an equally good fit to the

global database of age-depth measurements for a slightly smaller plate thickness of 130 ± 10 km (see red bar in Figure 9b). Significantly, translating across the misfit well in the direction of trade-off has a minimal effect on the shape of the age-depth relationship. Thus, any changes in calculated residual depth measurements are negligible. The values of both ΔT and z_p recovered by this analysis are consistent with the classic results obtained by *Parsons and Sclater* [1977] for the North Pacific and North Atlantic Oceans. However, our revised values are not consistent with the higher basal temperature and lower plate thickness obtained by *Stein and Stein* [1992].

In summary, our revised and augmented global database of water-loaded oceanic basement depths comprises the largest and most robust set of observations against which different models of oceanic lithosphere can be tested. Results indicate that the plate cooling model provides the most satisfactory explanation for subsidence of oceanic lithosphere as a function of age. The revised plate model is attractive on physical grounds and also yields a symmetric distribution of residual depths with minimal skewness (Figure 8b). Crucially, the distributions of residual depth measurements are fairly similar, irrespective of which of the different empirical and theoretical age-depth relationships are used (Figures 7 and 8). The consequences arising from using the alternative age-depth relationships are summarized in the supporting information.

6. Flexure and Geoid Height Corrections

Flexure of oceanic lithosphere due to loading by seamounts, sedimentary deposits, and subduction zones is a well-known source of bathymetric variation within the oceanic realm [*Watts*, 2001]. The wavelength of this flexural deformation depends upon the rigidity of the lithosphere and is usually manifested by large free-air gravity anomalies [*Gilbert*, 1895]. Many studies of the elastic properties of oceanic lithosphere have been carried out since the 1940s, and the general consensus is that elastic thickness is typically 10–20 km [*Watts*, 2001]. There is limited evidence that elastic thickness varies with plate age from near zero at active spreading centers up to a maximum of ~40 km within the oldest oceanic basins [e.g., *McKenzie and Fairhead*, 1997; *Watts and Burov*, 2003; *Bry and White*, 2007; *Mouthereau et al.*, 2013; *Craig and Copley*, 2014].

The spatial scale of sedimentary loading is typically large, with major deposits such as the Amazon Cone and Nigerian Delta extending over distances of 500–1000 km. In these instances, Airy (i.e., local) isostasy is generally an adequate approximation. In Appendix B, deformation associated with the Bengal Fan is used to illustrate potential flexural effects (Figure B1). Significant flexural bending is confined to locations with the largest gradients of loading (e.g., coastlines), and minimal deflection is observed within the bulk of the adjacent oceanic basins. Furthermore, flexural signals have wavelengths on the order of ~100 km for the expected range of elastic thicknesses. These length scales are significantly shorter than residual depth anomaly variations which occur on scales of ~1000 km. In order to avoid any flexural contamination, residual depth measurements have therefore been averaged within 1°, 2°, and 4° bins, which acts as a spatial smoothing filter [e.g., *Watts and Ribe*, 1984]. The longitudinal width of each bin is multiplied by 5 at latitudes above 70°. Short-wavelength flexural features adjacent to subduction zones and seamounts are clearly manifest by high-amplitude free-air gravity anomalies and have been excised from our observational database.

Finally, it is important to point out that residual depth anomalies are normally calculated with respect to the local sea-level. This reference is necessarily an equipotential surface (i.e., the geoid). Since the height of the non-hydrostatic geoid varies by tens of meters, we should correct spot measurements of residual depth for variations in geoid height using the shape of the undeformed hydrostatic surface as the reference [*Nakiboglu*, 1982; *Chambat et al.*, 2010]. The amplitude of this correction is generally minor with an RMS amplitude of 49 m. The largest correction is −145 m and occurs in the Ross Sea. When comparing our corrected observational database with a given predictive model of dynamic topography, it should be ascertained whether the predicted dynamic topography is calculated with respect to the geoid height anomalies or to the hydrostatic surface. Both geoid-corrected and geoid-uncorrected oceanic residual depth measurements are listed in the supporting information.

7. Residual Depth Anomalies

The majority of residual depth observations fall within ±1 km of the expected age-depth relationship with outliers of up to ±2 km (Figures 7 and 8). There is little evidence for an overall offset toward either positive or negative excursions. The mean and standard deviation for spot measurements is 0 ± 660 m. The steepest

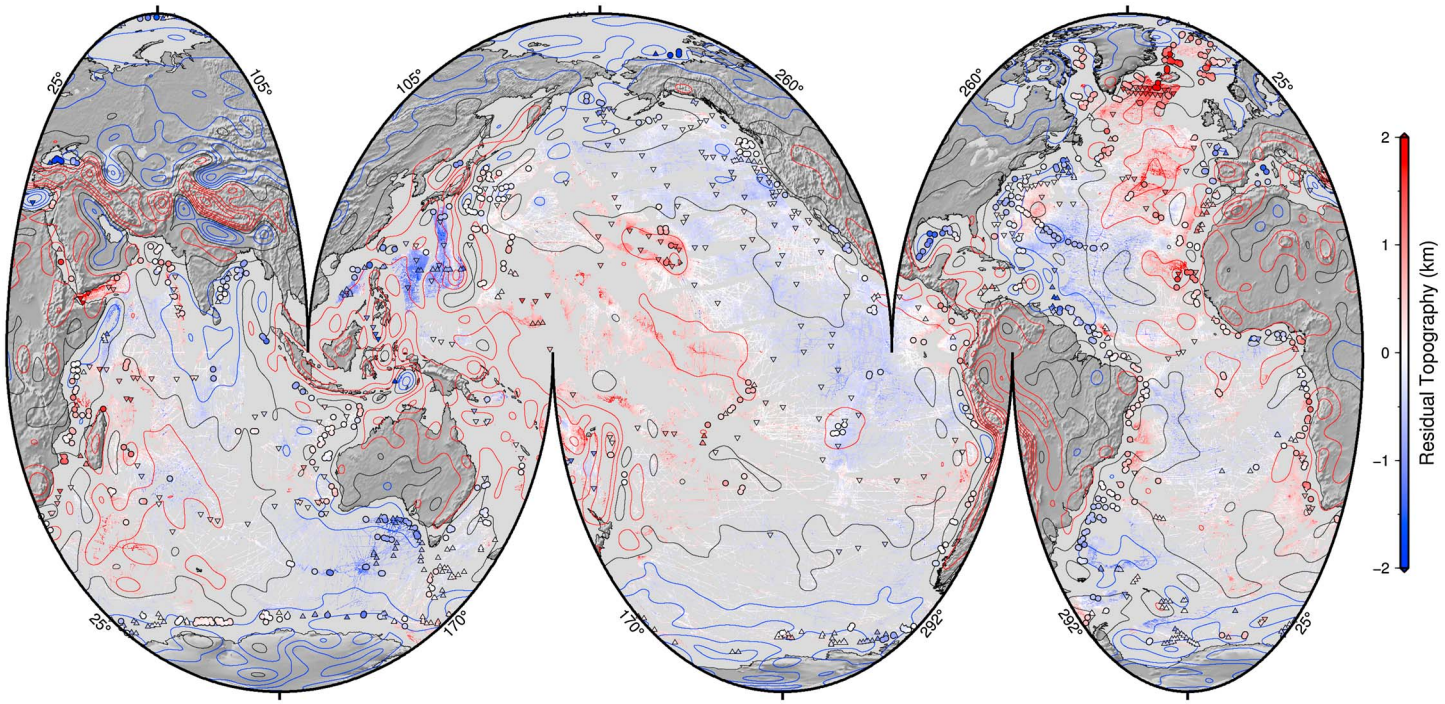

Figure 10. Global oceanic residual topography. Circles = residual depth measurements for which sedimentary and crustal corrections are applied; upward/downward pointing triangles = lower/upper limits for which only a sedimentary correction is applied (sign of crustal correction inferred from regional constraints). Observations are averaged in 2° bins. Criss-crossing network = ship-track residual depth grid (see Appendix C); red/black/blue contours = positive/zero/negative GOCO05S non-hydrostatic free-air gravity anomalies low-pass (> 730 km) filtered and plotted every 20 mGal [*Mayer-Guerr*, 2015].

gradients of residual depth are up to 1.5 m km^{-1} and occur south of Newfoundland, at the southern end of the Argentine Abyssal Plain, in the Gulf of Mexico, and at the eastern end of the Great Australian Bight. Oceanic crust in the vicinity of Iceland and Afar exhibits the largest positive anomalies, while the Beaufort Sea, the Gulf of Mexico, and the eastern portion of the Banda Arc have the largest negative anomalies (Figure 10). The spatial pattern of anomalies varies from spectacular ~1000 km undulations that occur along the west coast of Africa to a gigantic (~2500 km) swell in the North Atlantic Ocean centered on Iceland. These patterns exceed flexural length scales and most likely manifest sub-lithospheric density variations within the convecting interior.

A comprehensive spectral analysis of this observational database is described by *Hoggard et al.* [2016], whose results suggest that shallow convective circulation directly beneath the lithosphere makes a significant contribution to variations of dynamic topography. Here we primarily restrict our discussion to the relationship between this observational database and independent geological and geophysical observations (e.g., topography, free-air gravity anomalies, volcanism, earthquake seismicity, and tomographic models). The comparison between residual depth patterns and earthquake tomographic models presented here is visual and qualitative. A more quantitative approach is important but represents a significant undertaking [e.g., *Steinberger*, 2016; *Richards et al.*, 2016]. Here we concentrate on using the SL2013sv tomography model because it is specifically aimed at imaging upper mantle shear-wave velocity anomalies without imposing an a priori crustal model [*Schaeffer and Lebedev*, 2013]. We note that many similar anomalies are evident in numerous other models [e.g., *French et al.*, 2013; *Priestley and McKenzie*, 2013]. Four regional case studies are presented here, with three additional localities described in Appendix D.

7.1. Icelandic Swell

A major swell centered beneath Iceland extends across the entire North Atlantic Ocean from Baffin Island to western Norway and from Svalbard to Newfoundland (Figure 11). Peak residual depths are +2.3 km for measurements to which both sedimentary and crustal corrections have been applied. The amplitude of this swell decreases approximately radially away from Iceland. Anomaly size drops to +1.1 km on the southern Hatton Bank margin, to +700 m south of Greenland, to +500 m on the northern Vøring margin of Norway, and to +900 m in the Greenland Sea west of Svalbard. The swell extends southeastward as far as the Porcupine

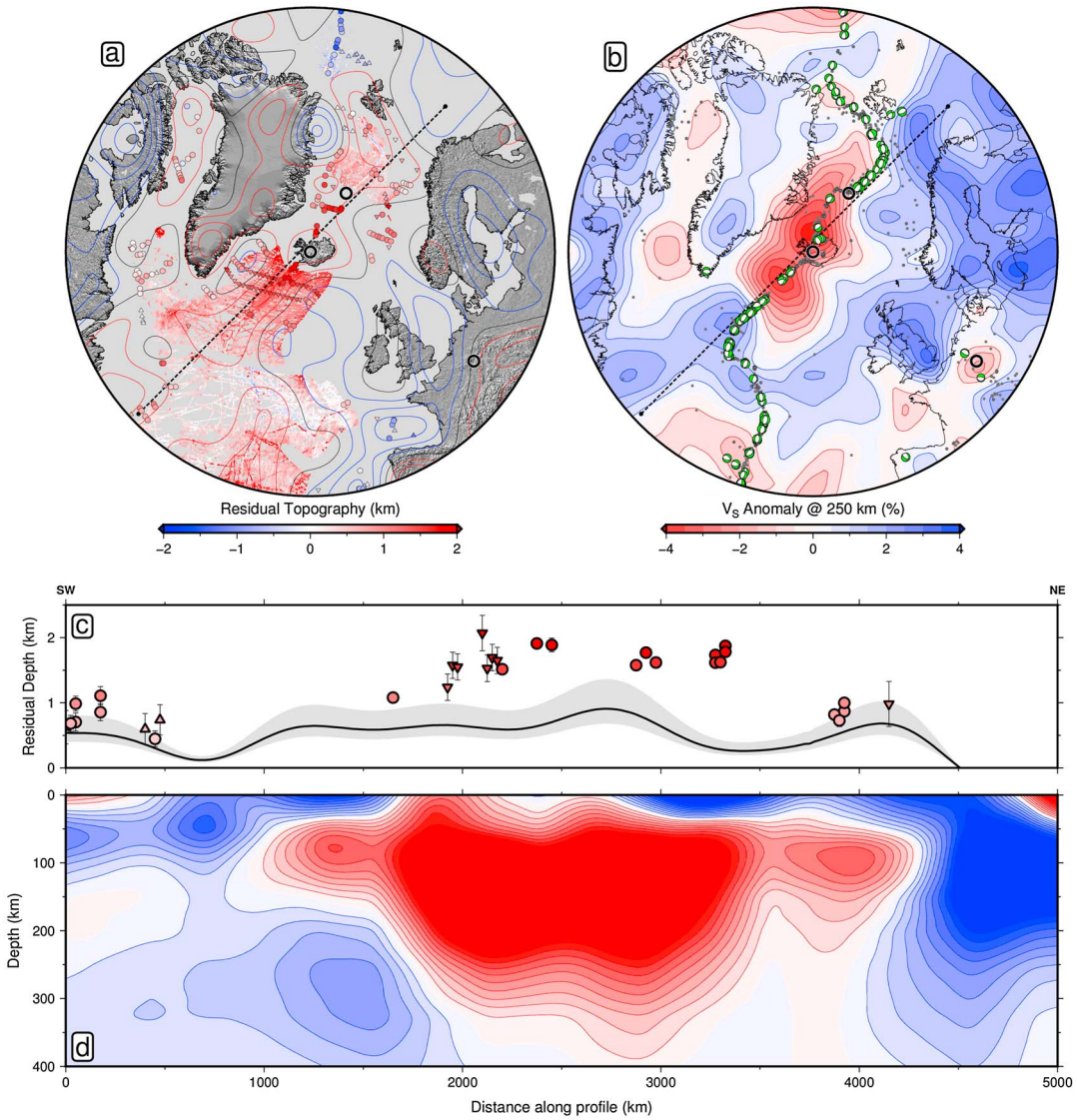

Figure 11. Residual topography of North Atlantic region. (a) Residual depth anomalies averaged in 1° bins. Symbols and ship-track data as in Figure 10; contours = non-hydrostatic free-air gravity anomalies from GOCO05S database, band-pass ($9000 > \lambda > 730$ km) filtered and plotted every 10 mGal [*Mayer-Guerr*, 2015]; black rings = Icelandic, Jan Mayen, and Eifel magmatic hotspots [*Courtillot et al.*, 2003]; dashed line = transect shown in Figure 11c. (b) Horizontal slice at depth of 250 km through SL2013sv tomographic model contoured every 0.5% [*Schaeffer and Lebedev*, 2013]. Gray dots = earthquakes ($M > 4$) from ANSS (1898–1975), CEC (1900–1975), and CMT (1976–2016) catalogues [*Engdahl and Villasenor*, 2002; *Dziewonski et al.*, 1981]; green beachballs = normal faulting focal mechanisms with $M_W > 5$ from CMT catalogue [*Ekström et al.*, 2012]. (c) Transect showing residual depth measurements within 80 km corridor with 1σ uncertainties often smaller than symbol size; black line with gray band = dynamic topography predicted from free-air gravity anomalies scaled using an admittance, $Z = 30 \pm 10$ mGal km^{-1}. (d) Vertical slice along transect showing shear-wave velocity anomalies from SL2013sv model [*Schaeffer and Lebedev*, 2013].

Basin offshore Ireland and southwestward to the Newfoundland margin. Westward, positive residual depth anomalies occur throughout the Labrador Sea including Baffin Bay but die out toward the northern reaches of this basin.

This large-scale bathymetric swell correlates both with free-air gravity anomalies and with upper mantle shear-wave velocity anomalies. The center of the swell is associated with a gradual reduction in earthquake seismicity along the mid-oceanic ridge where the number of large ($M_W > 5$) normal earthquakes decreases. This reduction may be consistent with a decrease in the thickness of the seismogenic layer [*Brace and Byerlee*, 1970; *Watts et al.*, 1980]. These different observations are consistent with the presence of a hot thermal

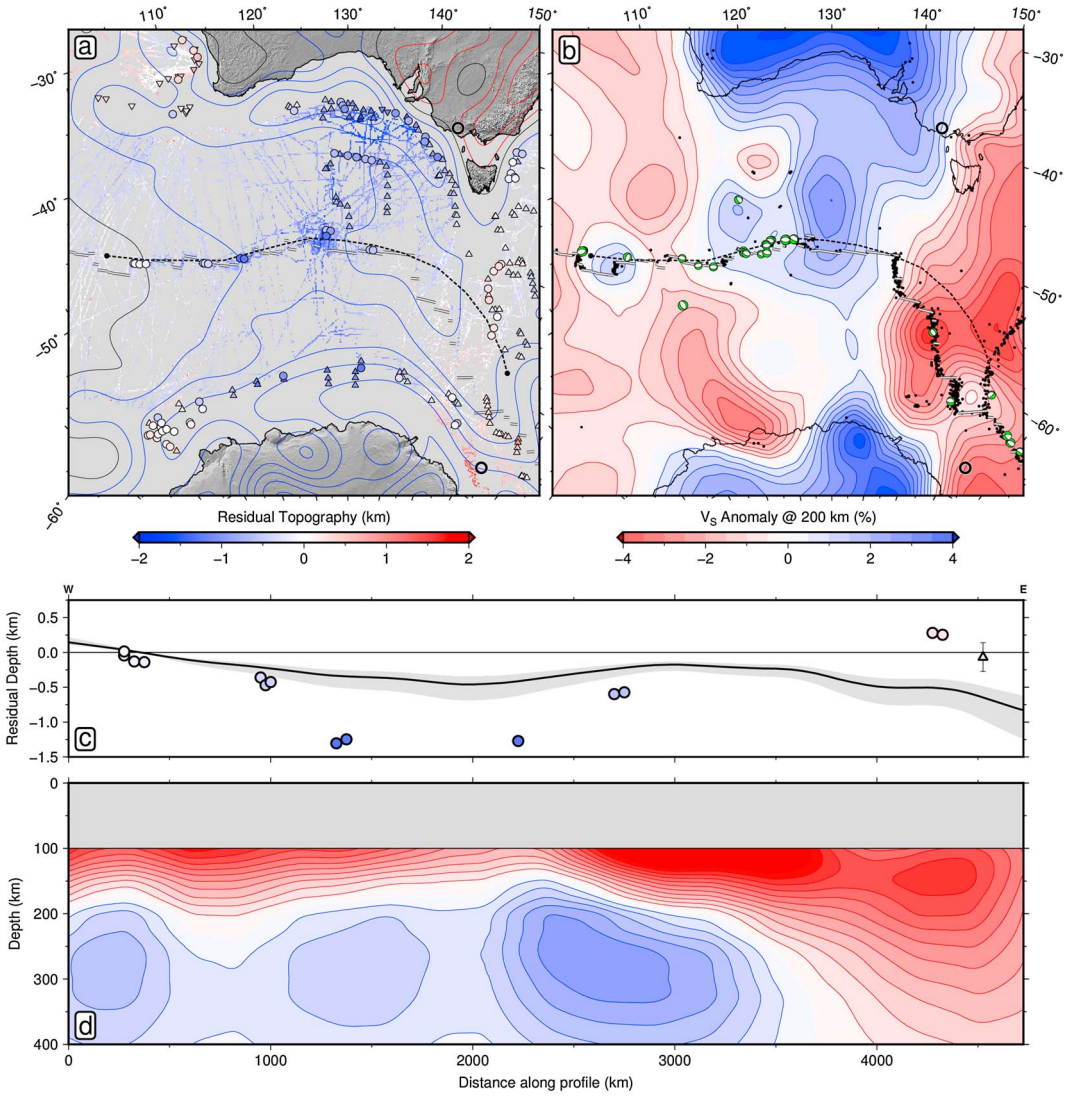

Figure 12. Residual topography of Australian-Antarctic Discordance. (a) Residual depth anomalies averaged in 1° bins. Symbols and ship-track data as in Figure 10; contours = non-hydrostatic free-air gravity anomalies from GOCO05S database, low-pass ($\lambda > 730$ km) filtered and plotted every 10 mGal [*Mayer-Guerr*, 2015]; black rings = Balleny and East Australian magmatic hotspots [*Courtillot et al.*, 2003]; gray tramlines = spreading segments along mid-oceanic ridge [*Gale et al.*, 2013]; dashed line = transect shown in Figure 12c. (b) Horizontal slice at depth of 200 km through SL2013sv tomographic model contoured every 0.5% [*Schaeffer and Lebedev*, 2013]. Gray dots = earthquakes as in Figure 11; green beachballs = normal faulting focal mechanisms ($M_W \geq 5$) from CMT catalogue [*Ekström et al.*, 2012]. (c) Transect showing residual depth measurements within 80 km corridor with 1σ uncertainties often smaller than symbol size; black line with gray band = dynamic topography calculated from free-air gravity anomalies using an admittance, $Z = 30 \pm 10$ mGal km^{-1}. (d) Vertical slice along transect showing shear-wave velocity anomalies from SL2013sv model [*Schaeffer and Lebedev*, 2013]. Note that anomalous velocities have been excluded within upper 100 km, associated with high homologous temperatures and partial melting beneath the ridge axis.

anomaly in the uppermost mantle beneath Iceland that may be fed by an upwelling mantle plume. Other tomographic studies have imaged a low-velocity sub-plate channel within which the plume head is localized. *Delorey et al.* [2007] used surface wave tomography to image a ~150 ± 50 km thick, slow shear-wave velocity anomaly beneath the Reykjanes Ridge, south of Iceland. *Rickers et al.* [2013] carried out full-waveform inverse modeling which shows that this thin layer has an irregular planform that reaches beneath the fringing continental margins of the North Atlantic Ocean.

Other studies show that rapidly varying temporal changes in Icelandic plume activity occur which provide additional support that dynamic topography may be generated by transient anomalies within a sub-plate

asthenospheric channel. Plume initiation is associated with the emplacement of intrusive and extrusive volcanic rocks across a ~2000 km wide region stretching from Baffin Island to the Faroes that constitute the North Atlantic Igneous Province [*White and McKenzie*, 1989]. Rare Earth element and $^{40}Ar/^{39}Ar$ analyses indicate that initial excess temperatures peaked at 100–200°C around 56 Ma, before decreasing by 50 Ma [*White and McKenzie*, 1989; *White et al.*, 1995; *Storey et al.*, 2007]. The extent of smooth versus highly fractured oceanic crust away from Iceland down the Reykjanes Ridge suggests that the radius of the plume head reduced dramatically to ~300 km by 46 Ma, before steadily increasing to a present-day lateral extent of ~900 km [*Jones et al.*, 2002].

In addition to these dramatic changes in swell radius, corroborating evidence for channelized sub-plate flow is provided by the pattern of V-shaped ridges on either side of the Reykjanes Ridge. These diachronous ridges track anomalously hot ripples of plume material that spread away from the Icelandic plume [*Vogt*, 1971]. The ripples travel radially outward at ~40 cm yr^{-1} which is an order of magnitude faster than plate spreading rates [*Parnell-Turner et al.*, 2014]. Older transient perturbations are inferred to have generated a series of ancient ephemeral landscapes that have been mapped along fringing continental margins [*Underhill*, 2001; *Smallwood and Gill*, 2002; *Hartley et al.*, 2011; *Millett et al.*, 2016]. Uplift and subsidence of a spectacular buried landscape in the Faroe-Shetland basin has been modeled using radial Poiseuille flow, which suggests that this landscape formed when a hot ripple was laterally advected beneath the plate within a low-viscosity, 200 km thick channel [*Hartley et al.*, 2011].

7.2. Australian-Antarctic Discordance

The Australian-Antarctic Discordance is a second region where sub-plate asthenospheric flow can be linked to the bathymetric expression of dynamic topography. A ~2000 km wide negative residual depth anomaly, or drawdown, with an amplitude of ~1 km is centered on the southeast Indian Ridge and extends southward to Wilkes Land and northward to the Great Australian Bight (Figure 12). There are several lines of evidence that support the presence of anomalously cold temperatures and downwelling flow within the upper mantle beneath this portion of the mid-oceanic ridge. First, there is a notable increase in the number of large ($M_W > 5$) earthquakes with normal faulting mechanisms along the ridge axis where the maximum drawdown occurs, potentially consistent with an increase in the thickness of the seismogenic layer. Second, the magnetization and geochemistry of mid-oceanic ridge basalts are consistent with low magmatic crystallization temperatures [*Anderson et al.*, 1980; *Klein et al.*, 1991; *Christie et al.*, 2004; *Dalton et al.*, 2014]. Third, seismological studies show that shear-wave velocities are anomalously fast within the top 200 km of the mantle [*Forsyth et al.*, 1987; *Ritzwoller et al.*, 2003]. Finally, geoid and free-air gravity analyses demonstrate that a broad negative anomaly straddles the region, consistent with the proposal that active mantle downwelling causes the Australian-Antarctica Discordance [*Marks et al.*, 1991]. These different observations have been combined in geodynamical models of mantle flow which require the existence of a shallow channel of low viscosity [*Buck et al.*, 2009].

7.3. Antarctica

Oceanic residual depth anomalies often vary over length scales as short as ~1000 km and are best illustrated along transects whose margins are largely unaffected by active tectonics since continental rifting and breakup. One excellent and illuminating example is a near-complete circum-Antarctica transect (Figure 13). Starting in the Weddell Sea south of the Falkland Islands and east of the Antarctica Peninsula, residual depths show a minimum of −400 m rising eastward up to +600 m offshore Dronning Maud Land. Continuing clockwise around Antarctica, a substantial negative anomaly peaking at −800 m occurs offshore Enderby Land. Residual depths then steadily increase to a value of +300 m near Kemp Land, which occurs along the southern margin of the Indian Ocean. Wilhelm II Land has anomalies ranging from +200 m down to −500 m, which continue to decrease toward Wilkes Land where they reach a maximum of −1.2 km, marking the southernmost extent of the Australian-Antarctica Discordance.

Continuing clockwise around Antarctica into Oates Land, a positive residual depth anomaly of +500 m occurs in the vicinity of the Balleny Islands. These seamounts are active stratovolcanoes that produce enriched basaltic melts generated by the proposed Balleny plume [*Lanyon et al.*, 1993]. The Ross Sea has neutral to −500 m residual depth anomalies. The Amundsen Sea, offshore Marie Byrd Land, is characterized by positive residual depth anomalies varying from +600 m proximal to the shelf down to zero in more distal regions. This swell is associated with volcanic edifices known as the Marie Byrd seamounts that were mostly formed

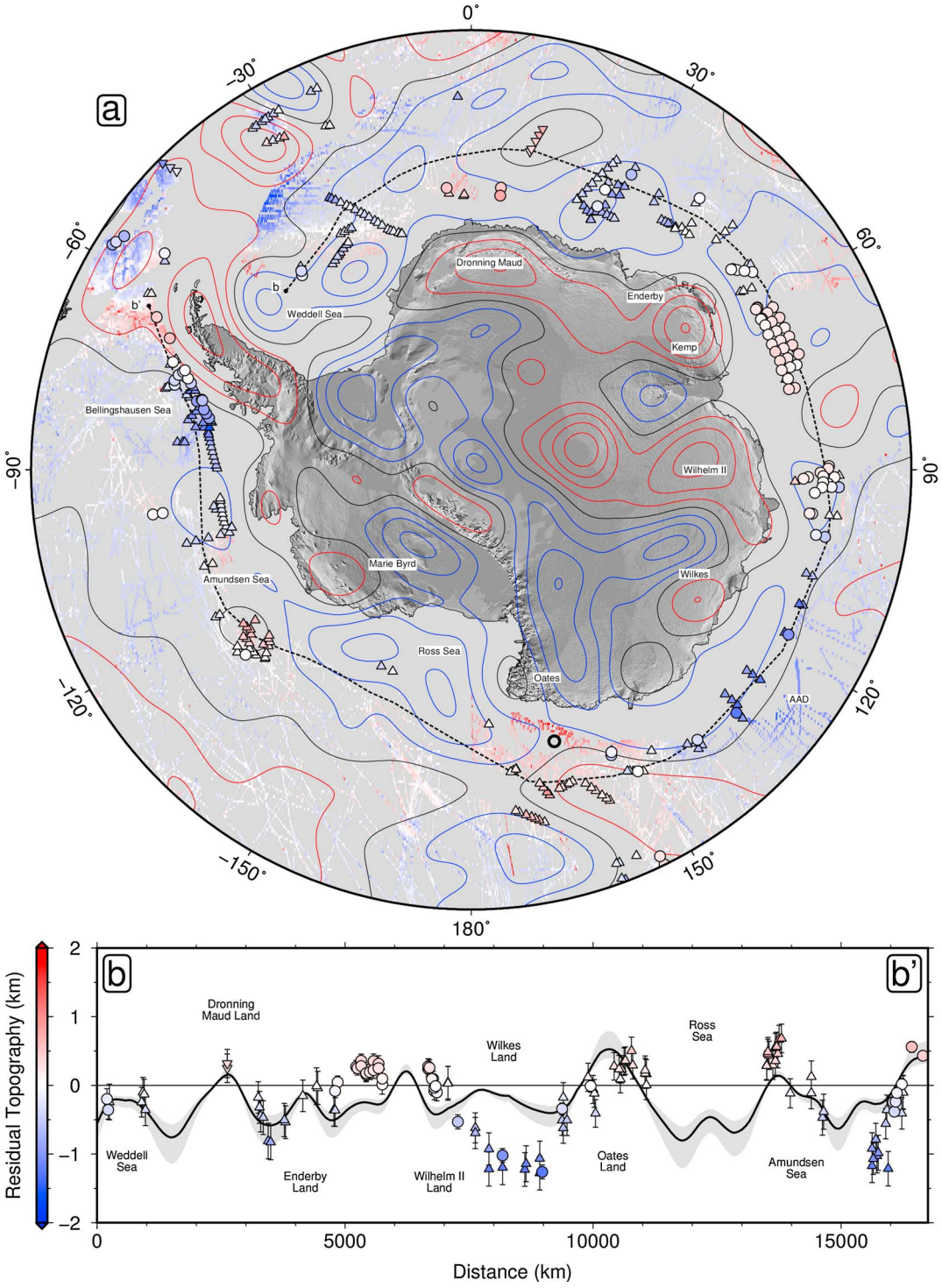

Figure 13. Residual topography of Antarctica. (a) Residual depth anomalies averaged in 1° bins. Symbols and ship-track data as in Figure 10; contours = non-hydrostatic free-air gravity anomalies from GOCO05S database, band-pass ($9000 > \lambda > 730$ km) filtered and plotted every 10 mGal [*Mayer-Guerr*, 2015]; black ring = Balleny hotspot [*Courtillot et al.*, 2003]; dashed line labeled b-b′ = locus of transect shown below. (b) Transect showing residual depth measurements within 80 km corridor with 1σ uncertainties often smaller than symbol size; black line with gray band = dynamic topography calculated from free-air gravity anomalies using an admittance, $Z = 30 \pm 10$ mGal km^{-1}.

in early Cenozoic (65–56 Ma) times but have been rejuvenated with minor Pliocene activity [*Kipf et al.*, 2014]. This broadly uplifted region is also evident in the residual depth study of *Wobbe et al.* [2014]. However, their recovered amplitudes are probably too large because they did not carry out crustal corrections and they also used an age-depth relationship based exclusively upon North Pacific bathymetric observations [*Crosby et al.*, 2006]. Finally, the Bellingshausen Sea has crustal-corrected negative anomalies as low as −1.2 km which steadily rise up to +500 m along the western flank of the Antarctic Peninsula toward the South Sandwich Islands.

This circum-Antarctica pattern of residual depth anomalies is generally mirrored by changes in free-air gravity anomalies. This match suggests that scaling the free-air gravity field by a constant value of admittance, $Z = 30 \pm 10$ mGal/km, sometimes yields a reasonable proxy for dynamic topography within the oceanic realm, in agreement with many previous studies [*Crosby et al.*, 2006; *Winterbourne et al.*, 2009]. However, correlation between these residual depth measurements and a range of seismic tomographic models is notably poor. The quality of this correlation probably reflects the limited resolution of these global tomographic models as a result of sparse ray coverage for Antarctica, particularly within the upper mantle.

7.4. South Atlantic Ocean

The pattern of residual depth anomalies along either side of the South Atlantic Ocean is particularly striking (Figure 14). A notable feature are smoothly varying cycles that define a regular series of domes and depressions with amplitudes of ±1 km and wavelengths of ~1000 km.

At the northern end of the South American margin, negative residual depths of −800 m occur in the vicinity of the Amazon Cone. These low values persist within the Demerara abyssal plain and then start to steadily climb southward. The Pernambuco abyssal plain has minor positive residual depth anomalies which grow southward reaching amplitudes of +600 m before decreasing again. This portion of the continental margin occurs on the flanks of the onshore Borborema Plateau. The seaboard of this plateau is characterized by emergent Miocene coastal deposits [*Rossetti et al.*, 2013]. There is also a series of Holocene and Pleistocene marine terraces that yield uplift rates of 0.1–0.5 mm yr^{-1} [*Barreto et al.*, 2002; *Bezerra et al.*, 2003; *Angulo et al.*, 2006; *Hein et al.*, 2014]. Within the center of the plateau, late Miocene and Pliocene volcanic rocks have ocean island basalt source affinities, which suggests that regional uplift may be caused by decompression melting of anomalously hot asthenospheric mantle [*Cordani*, 1970; *Knesel et al.*, 2011].

South of the Borborema Plateau, residual depth measurements have positive values of up to +700 m. At about 25°S, a steep gradient occurs and residual depths decrease toward the Argentine Abyssal Plain which is characterized by a −600 m residual depth anomaly. This substantial negative anomaly is ~2000 km wide and is thought to be one of the largest convective drawdowns on Earth [*Hohertz and Carlson*, 1998].

A contrasting set of residual depth anomalies are observed along the West African margin. Starting in the north, offshore Liberia has +300 m residual topography which decreases to −600 m within the Guinea abyssal plain. Values climb to +1 km at the Cameroon Volcanic Line. This elongated swell is associated with Oligocene to present-day seamounts with ocean island basalt affinities that are consistent with a sub-plate thermal anomaly. Offshore Gabon, negative anomalies of −400 m steadily increase southward, peaking at +1.2 km adjacent to the onshore Angolan dome. Here the amplitude and wavelength of residual depth measurements are in striking agreement with the location of this topographic dome which straddles the continental margin. There is an excellent match between these residual depth measurements, the long-wavelength free-air gravity anomaly, and shear-wave velocity anomalies. The cyclic character of residual depth is clearly visible and well matched by assuming an admittance value of $Z = 30 \pm 10$ mGal km^{-1}.

The West African coastline exhibits multiple lines of independent evidence that support rapid and ongoing regional uplift and subsidence (Figure 15). The present-day continental shelf edge is characterized by a striking angular unconformity that truncates Oligocene to Pliocene deltaic foreset deposits. Denudation estimates from the overcompaction of these sediments suggest that deltaic topset deposits have been removed by uplift and erosion. Inverse modeling of stacking velocities indicates that up to 500 m of post-Pliocene uplift occurred, which steadily decays away to zero to the north [*Al-Hajri et al.*, 2009]. This uplift gradient is consistent with the amplitude and wavelength of residual depth measurements, suggesting that a component of regional uplift of the Angolan dome occurred within the last 5–10 Ma. Quaternary uplift rates of 0.3 mm yr^{-1} have been estimated from the age and height of emergent marine terraces that flank the dome south of Luanda [*Giresse et al.*, 1984; *Jackson et al.*, 2005; *Guiraud et al.*, 2010]. An optically stimulated luminescence

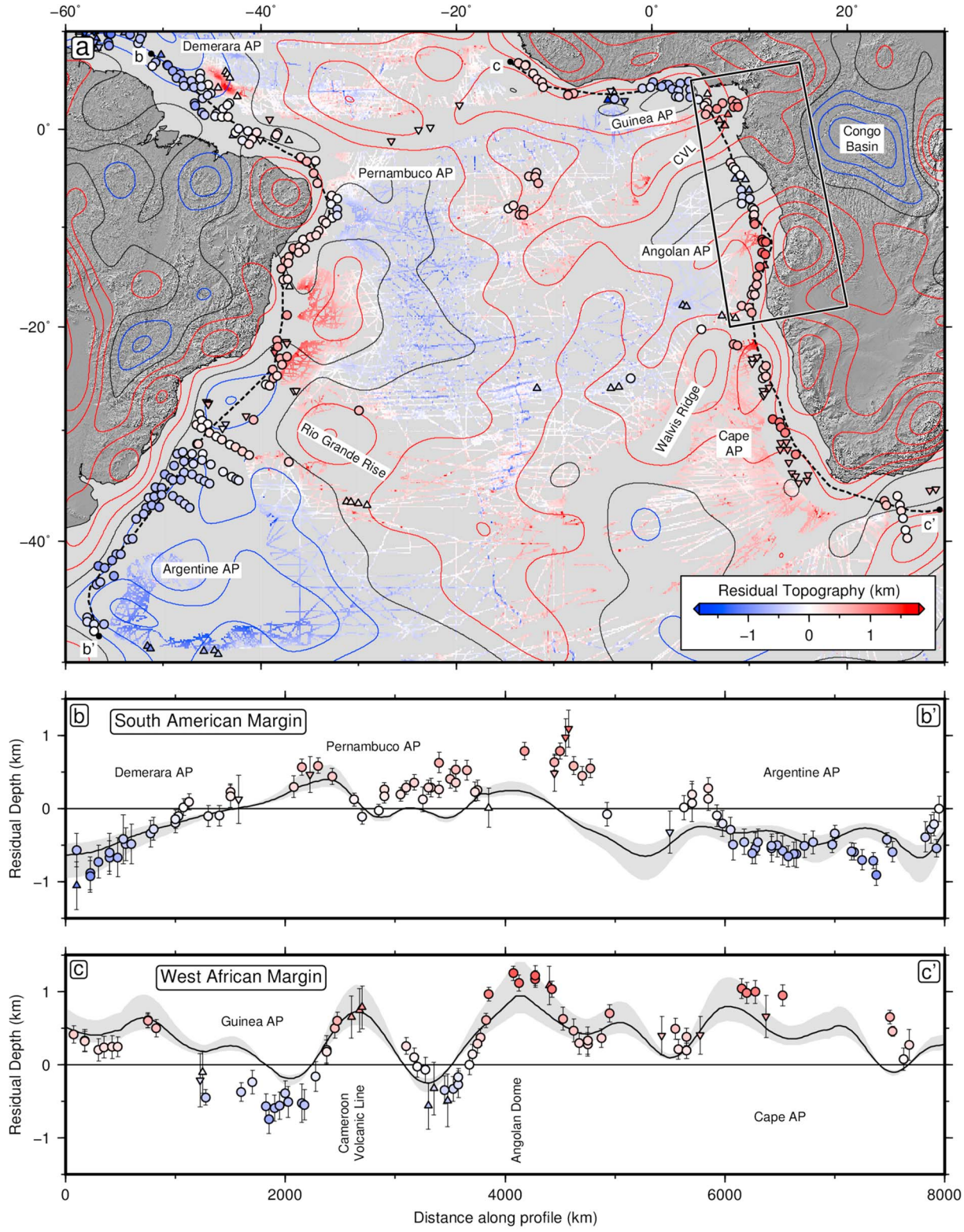

Figure 14. Residual topography of South Atlantic Ocean. (a) Residual depth anomalies averaged in 1° bins. Symbols and ship-track data as in Figure 10; contours = non-hydrostatic free-air gravity anomalies from GOCO05S database, low-pass (> 730 km) filtered and plotted every 10 mGal [*Mayer-Guerr*, 2015]; major bathymetric features are labeled; AP = abyssal plain; box = location of Figure 15; dashed lines labeled b-b′ and c-c′ = transects shown below. (b) Transect along South American margin showing residual depth measurements within 80 km corridor with 1σ uncertainties often smaller than symbol size; black line with gray band = dynamic topography calculated from free-air gravity anomalies using an admittance, $Z = 30 \pm 10$ mGal km^{-1}. (c) Transect along West African margin.

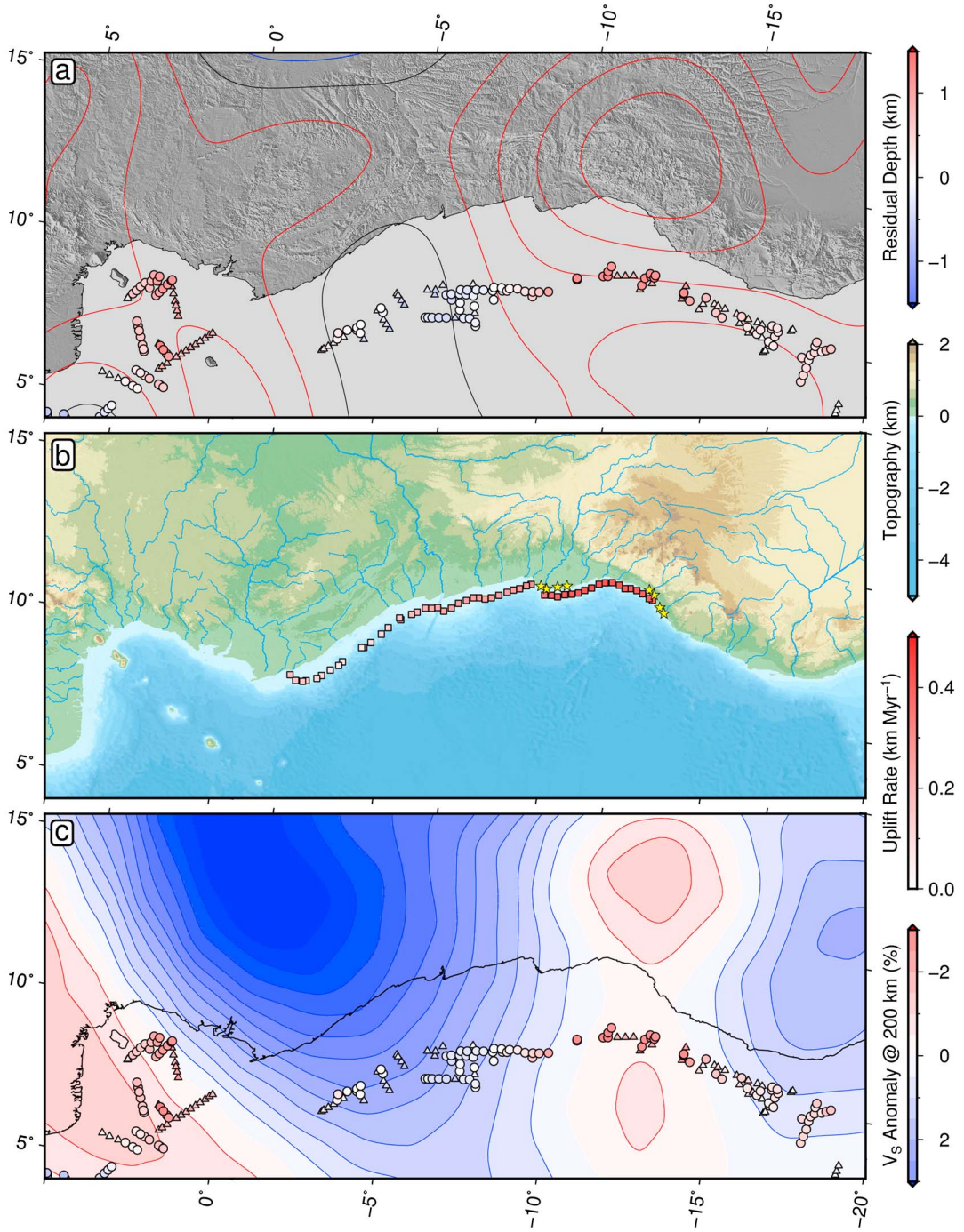

Figure 15. Residual topography of West Africa. (a) Residual depth anomalies averaged in 1° bins. Symbols and ship-track data as in Figure 10; contours = non-hydrostatic free-air gravity anomalies from GOCO05S database, low-pass (> 730 km) filtered and plotted every 10 mGal [*Mayer-Guerr*, 2015]. (b) Topographic map overlain with major drainage (SRTM30_PLUS database) [*Becker et al.*, 2009]. Red squares = uplift rate values calculated from post-Pliocene shelf denudation estimates [*Al-Hajri et al.*, 2009]; yellow stars = emergent marine terraces [*Giresse et al.*, 1984; *Jackson et al.*, 2005; *Guiraud et al.*, 2010; *Walker et al.*, 2016]. (c) Horizontal slice at depth of 200 km through SL2013sv tomographic model contoured every 0.5% [*Schaeffer and Lebedev*, 2013]. Symbols = residual depth anomalies from Figure 15a.

study of a prominent terrace complemented by ^{14}C dating of cockle and bivalve shells suggests that uplift rates might be as fast as 1.5–2 mm yr^{-1} [*Walker et al.*, 2016].

Onshore, the radial drainage pattern suggests that growth of this dome has influenced regional geomorphology. Many Angolan rivers rise within the Bié Plateau which has elevations of 1.5–2 km. A regional uplift history calculated by inverting an inventory of longitudinal river profiles suggests that the Angolan dome grew in two stages [*Roberts and White*, 2010]. The first stage occurred in Oligo-Miocene (~25 Ma) times when about 500 m of uplift occurred. This event is corroborated by calibrated seismic reflection profiles from the continental shelf on which a ~25 Ma sequence stratigraphic boundary separating aggrading and prograding sedimentary packages is clearly visible [*Walford and White*, 2005]. The second stage of domal growth occurred within the last 10 Ma. This second stage coincides with the offshore truncation of Pliocene deltaic sedimentary rocks [*Al-Hajri et al.*, 2009].

Finally, the Congo River and its tributaries drain the northern portion of the Angolan dome and deliver clastic sediments onto the adjacent Atlantic margin at a position where a negative residual depth anomaly occurs. Reconstructions of solid sedimentary flux show that there are notable increases at different stages during Neogene times that are consistent with the inferred uplift history of this dome [*Lavier et al.*, 2001].

In summary, a range of disparate independent observations demonstrates the first-order control that spatial and temporal changes of dynamic topography can exert on the structural geometry of continental margins. As elsewhere, shear-wave velocity anomalies immediately beneath the lithospheric plate correlate with residual depth anomalies and other geological observations. This correlation underlines the role that shallow mantle convection, potentially within a low-viscosity channel, appears to play in generating and maintaining bathymetric and topographic features [e.g., *Phipps Morgan et al.*, 1995].

8. Consequences for Long-Wavelength Dynamic Topography

Since the 1980s, there has been considerable debate about the spatial and temporal pattern of dynamic topography produced by convective circulation of the Earth's mantle. This debate has centered on differences between the amplitude and wavelength of observed and predicted dynamic topography. *Hoggard et al.* [2016] used an earlier version of the database of oceanic residual depth anomalies presented here to generate a spherical harmonic representation. Their aims were twofold. First, they showed that residual depth observations can be accurately fitted up to and including a maximum spherical harmonic degree $\iota_{max} = 30$ (i.e., wavelengths down to and including $\lambda = 1300$ km). This maximum degree was chosen based upon the decrease of residual misfit with increasing ι_{max}. Second, *Hoggard et al.* [2016] showed that the long-wavelength components of this spherical harmonic representation (i.e., $\iota = 1–3$ corresponding to $\lambda \geq 11,500$ km) broadly agree with the pattern of geoid anomalies. The amplitude of this long-wavelength dynamic topography is non-zero but is significantly smaller than amplitudes obtained from some predictive models of dynamic topography. Thus, the peak amplitude of observed dynamic topography at $\iota = 1–3$ is about 500 m, compared with 1–2 km suggested by many, but not all, predictive models.

Subsequently, *Yang and Gurnis* [2016] have used the observational database of *Hoggard et al.* [2016] to argue that the maximum degree to which a spherical harmonic representation can be inferred is only $\iota_{max} < 5$ (i.e., $\lambda > 7300$ km). This assertion is predicated upon a statistical analysis known as the cross-validation procedure that seeks to assess the ability of a given model to successfully predict new data [see *Arlot and Celisse*, 2010; and references therein]. When only a limited amount of data is available, the philosophy of cross-validation is applied by splitting these data into a training set and a validation set. A model is fitted to the training set, and its predictive ability is evaluated on the withheld validation data as an estimate of model performance.

In their cross-validation analysis, *Yang and Gurnis* [2016] randomly select 80% of the oceanic spot measurements and compute the spherical harmonic fit for increasing values of ι_{max}. This procedure is repeated 30 times for each ι_{max}, before the average misfit between the model and both the 80% training set and 20% validation set is computed. When $\iota_{max} \geq 5$, they assert that the misfit for the validation set is significantly larger than that for the training set. *Yang and Gurnis* [2016] therefore conclude that a spherical harmonic representation of oceanic spot measurements should be restricted to $\iota_{max} = 5$. This spherical harmonic fit has the important consequence of yielding peak amplitudes of 1.2 km for the $\iota = 1–3$ long-wavelength components.

It is not immediately obvious that this approach is a useful test of the main conclusions presented by *Hoggard et al.* [2016]. Cross-validation is principally designed to test the predictive power of a model with respect to

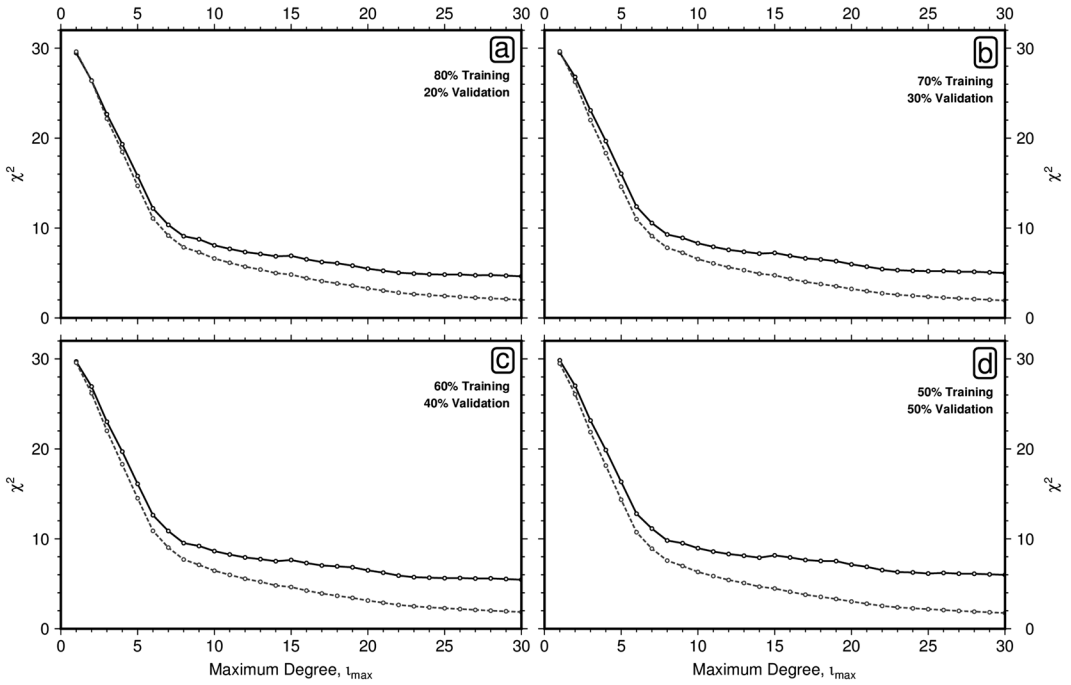

Figure 16. Monte Carlo cross-validation. (a) Residual misfit, χ^2, plotted as a function of maximum spherical harmonic degree, ι_{max}. Gray circles/dashed lines = median χ^2 value for ensemble of 1000 randomly chosen training sets that comprise 80% of spot measurements. Black circles/lines = same for ensemble of validation sets that comprise the remaining 20% of spot measurements. (b) Results for 70%–30% split. (c) Results for 60%–40% split. (d) Results for 50%–50% split.

new data. The aim of *Hoggard et al.* [2016] was simply to investigate the spherical harmonic contents of the existing oceanic residual depth measurements. Nevertheless, we take this opportunity to re-examine these issues using a revised database of 2297 spot measurements that is analyzed within the same cross-validation framework employed by *Yang and Gurnis* [2016].

Our spot measurements of oceanic residual topography data are randomly split 1000 times into an 80% training set and a 20% validation set, in accordance with the Monte Carlo cross-validation scheme [*Picard and Cook*, 1984]. Spherical harmonic fitting is then carried out for increasing values of ι_{max} using the approach described by *Hoggard et al.* [2016]. The model misfit, χ^2, is subsequently calculated for both the training and validation sets. The median value at each ι_{max} for 1000 ensembles is shown in Figure 16a. This procedure was repeated for 70%–30%, 60%–40%, and 50%–50% training-validation set splits.

Two important conclusions can be drawn from this Monte Carlo cross-validation analysis. First, χ^2 for the ensemble of validation sets is greater than for the ensemble of training sets. This conclusion accords with the well-known classic statistical phenomenon—any model fitted to a data set always provides a more optimistic fit to data used in its derivation than to any new data [e.g., *Larson*, 1931; *Mosteller and Tukey*, 1977; *Picard and Cook*, 1984]. Second, and more importantly, χ^2 for both ensembles of training and validation sets continues to significantly reduce up to, and well beyond, $\iota_{max} = 5$. Thus, for an 80%–20% split, the median value for the ensemble of training sets yields $\chi^2 = 14.7$ for $\iota_{max} = 5$, decreasing to $\chi^2 = 2.0$ for $\iota_{max} = 30$. The median value for the equivalent ensemble of validation sets yields $\chi^2 = 15.8$ for $\iota_{max} = 5$, decreasing to $\chi^2 = 4.6$ for $\iota_{max} = 30$. Thus, a spherical harmonic representation where $\iota_{max} = 5$ yields a significantly poorer match to oceanic spot measurements compared to a spherical harmonic representation where $\iota_{max} = 30$.

This robust and significant conclusion is confirmed by visually comparing spot measurements and spherical harmonic representations (Figure 17). Transects of oceanic spot measurements both from the West African margin and from the northwest Pacific Ocean have been fitted using spherical harmonic representations with $\iota_{max} = 5$, 10, and 30. When $\iota_{max} = 5$ or 10, the global distribution of residual misfits is large (Figures 17c and 17g). When $\iota_{max} = 30$, the global distributions of residual misfits are significantly lower and both transects are fitted (Figure 17i–17k).

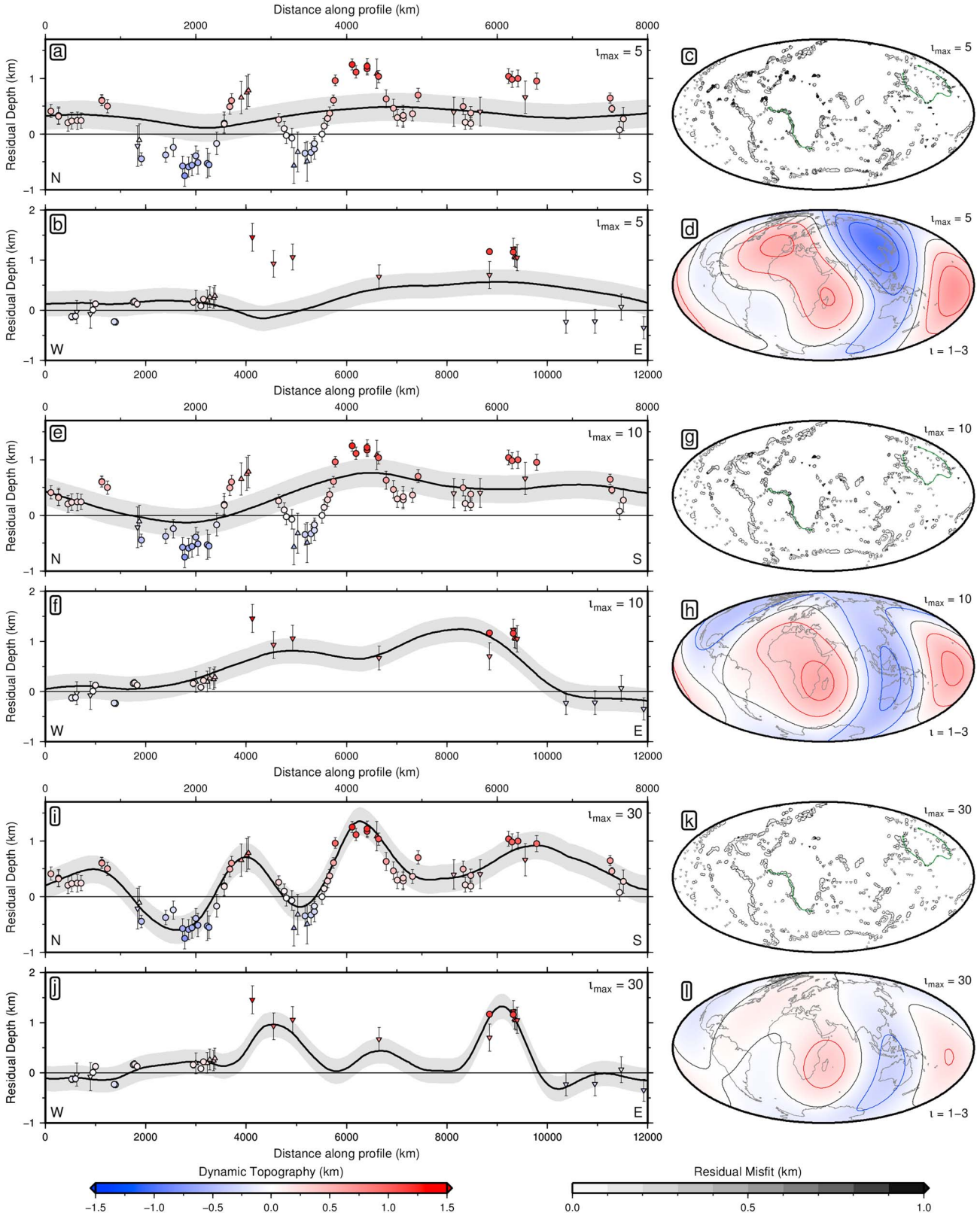

Figure 17. Spherical harmonic fitting of residual depth anomalies. (a) Transect down West African margin from Figure 14c. Residual depth data averaged within 1° bins within 80 km corridor with 1σ uncertainties. Black line with gray bounds = spherical harmonic fit to global residual depth spot measurements alone for ι_{max} = 5 with ±250 m envelope. (b) Same for transect in northwest Pacific Ocean. (c) Global map of residual misfit between observations and ι_{max} = 5 fit. Green lines = transect locations. (d) ι = 1–3 components of the ι_{max} = 5 fit, contoured every 250 m. (e–h) Same for ι_{max} = 10 fit. (i–l) Same for ι_{max} = 30 fit.

The Monte Carlo cross-validation procedure crucially highlights the pitfalls of not carrying out a damped spherical harmonic representation to a sufficiently large value of ι_{max}. If the chosen ι_{max} is too low, higher-degree power present within the observational database is forced to bleed into lower degree coefficients, which yields excessively large amplitudes of dynamic topography for the $\iota = 1-3$ components. Figures 17d, 17h, and 17l demonstrate that the peak amplitude for the $\iota = 1-3$ components decreases from 1.0 km down to 0.6 km and then 0.4 km for $\iota_{max} = 5$, 10, and 30, respectively. We suggest that the large amplitude of dynamic topography for the $\iota = 1-3$ components recovered by *Yang and Gurnis* [2016] is probably an artifact arising from their choice of a low $\iota_{max} = 5$.

9. Conclusions

A comprehensive global database of 2297 oceanic residual depth measurements is built from a combination of seismic reflection, modern wide-angle, and vintage refraction experiments throughout the oceanic realm. Careful analysis has been carried out to remove the isostatic consequences of variable sedimentary loading and also crustal thickness for a subset of 1161 of these spot measurements. Uncertainties have been propagated to ensure the robustness of these measurements and to formally estimate their errors. This database has been used to reassess subsidence of oceanic lithosphere as a function of age. We conclude that an analytical plate model with a basal temperature of ~1250°C and an equilibrium thickness of 150 km yields the optimal fit to the observational database. Although a half-space cooling model can also be used to fit this database, the resultant ridge axis temperature is ~300°C smaller than that required to generate the thickness and composition of mid-oceanic ridge basalts.

Residual depth anomalies can be measured with respect to either the plate or half-space cooling models or by fitting an empirical relationship. These anomalies have wavelengths of 1000–2500 km and amplitudes of ±1 km. Peak amplitudes of +2 km are associated with the Icelandic and Afar plume centers. Many other plume swells are manifest by positive residual depth anomalies. Drawdown up to −2 km is observed in the Gulf of Mexico, in the Beaufort Sea, and in the Banda Sea. Broad regions of negative residual depth occur across Southeast Asia, across the Australia-Antarctic Discordance, and within the Argentine Abyssal Plain.

Cross-validation analysis of spherical harmonic representations of oceanic spot measurements demonstrates that these observations are optimally fitted using spherical harmonic degrees up to and including $\iota = 30$ (i.e., wavelengths down to and including $\lambda = 1300$ km). A significant corollary is that the longest wavelength $\iota = 1-3$ components (i.e., corresponding to wavelengths of $\lambda \geq 11,500$ km) have amplitudes that are considerably smaller than those predicted by many dynamic topographic models.

Independent geological observations suggest that at least some of these positive and negative anomalies grow and decay on timescales of millions of years, which implies that they are generated and maintained by convective circulation of the Earth's sub-lithospheric mantle. Considerable geological, geophysical, and geochemical evidence corroborate the notion that these anomalies have undergone significant growth and decay within the Neogene period. There is reasonable agreement between observed dynamic topographic patterns and tomographic models of seismic velocity anomalies within the uppermost mantle. We suggest that some dynamic topographic anomalies are generated and maintained by thermal anomalies within shallow sub-plate asthenospheric channels. Independent evidence for rapid lateral asthenospheric flow has been reported for the Icelandic plume and for the Australian-Antarctic Discordance that is consistent with the existence of a low-viscosity channel immediately beneath the lithospheric plates.

Appendix A: Crustal Correction Uncertainties

An error analysis of crustal corrections is carried out by assuming that uncertainties in different parameters are uncorrelated. This assumption permits the use of the variance formula, where for any function $x = f(a, b, \ldots)$, the standard deviation, σ_x, is given by

$$\sigma_x = \sqrt{\left(\frac{\partial x}{\partial a}\right)^2 \sigma_a^2 + \left(\frac{\partial x}{\partial b}\right)^2 \sigma_b^2 + \ldots} \tag{A1}$$

where σ_a is the standard deviation of an example variable [*Ku*, 1966]. Differentiating equation (8) with respect to each variable and exploiting the quotient rule for the case of mantle density yields

$$\frac{\partial C_c}{\partial \rho_a} = \frac{(z_c - 7.1)(\rho_c - \rho_w)}{(\rho_a - \rho_w)^2} \tag{A2}$$

$$\frac{\partial C_c}{\partial \rho_c} = \frac{7.1 - z_c}{\rho_a - \rho_w} \tag{A3}$$

$$\frac{\partial C_c}{\partial \rho_w} = \frac{(z_c - 7.1)(\rho_a - \rho_c)}{(\rho_a - \rho_w)^2} \tag{A4}$$

The magnitude of these errors as a function of crustal thickness is presented in the supporting information. There is additional uncertainty associated with the depth conversion from two-way travel time for crustal thicknesses estimated from seismic reflection profiles. The above differential terms can be adapted by replacing z_c with $\frac{1}{2}v_c t_c$, where t_c is crustal thickness measured in two-way travel time. In addition, the differential term associated with uncertainty in crustal velocity is given by

$$\frac{\partial C_c}{\partial v_c} = \frac{(\rho_a - \rho_c)t_c}{2(\rho_a - \rho_w)} \tag{A5}$$

Parameter uncertainties are listed in Table 2. All crustal-corrected residual depth measurements include the uncertainties arising from these crustal correction errors.

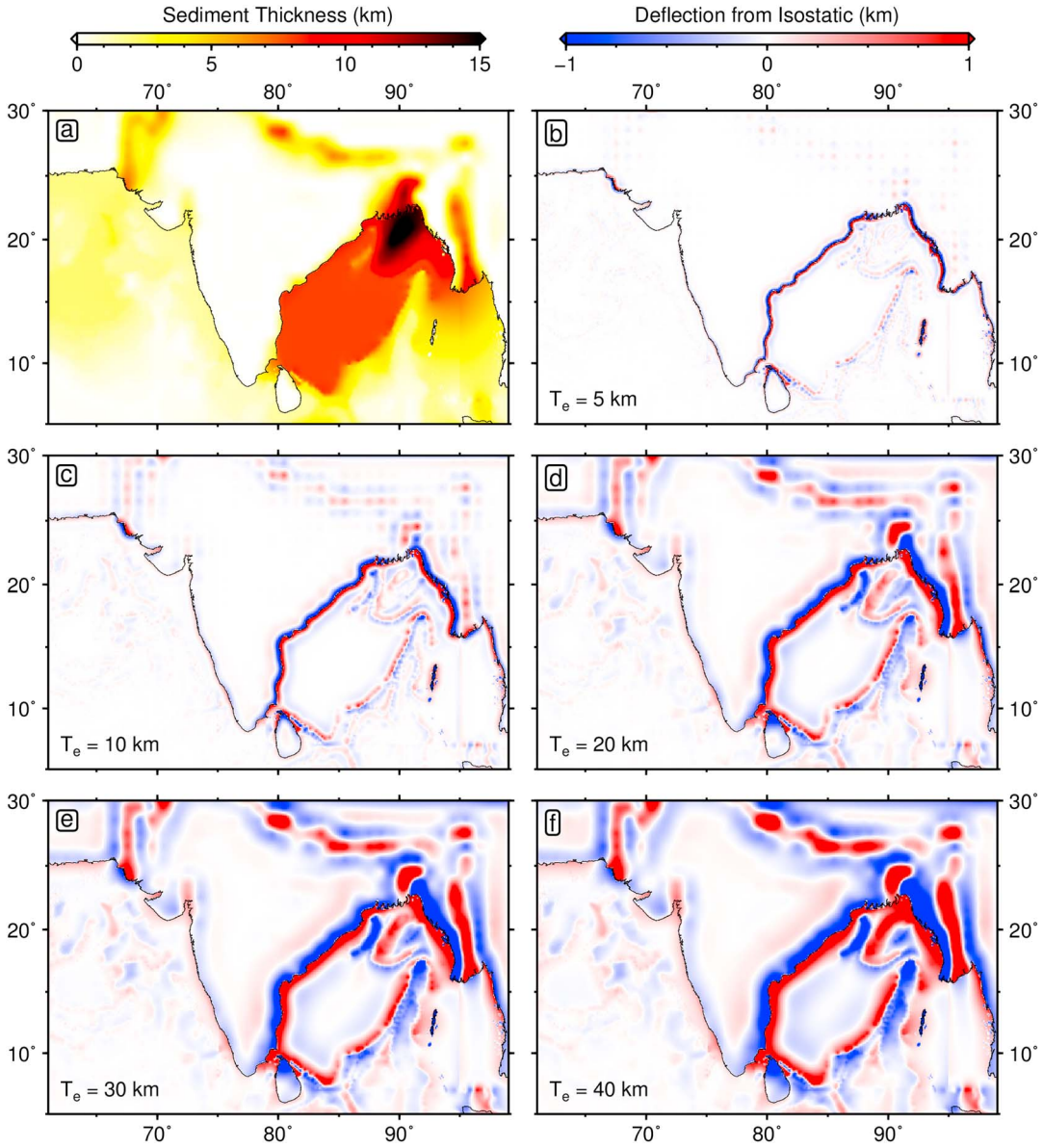

Figure B1. Flexural bending caused by Bengal Fan. (a) Sedimentary thickness variation [*Divins*, 2003]. (b–f) Water-loaded deflection with respect to an Airy isostatic model as a function of elastic thickness, T_e.

Appendix B: Flexural Analysis

The Bengal Fan provides a helpful case study which illustrates how flexural bending is generated by sedimentary loading. Figure B1a shows the variation of sediment thickness around the Indian sub-continent taken from the NGDC grid [*Divins*, 2003]. These thicknesses are converted into a sedimentary load using equation (7) which includes the effects of compaction. The water-loaded difference between flexurally and isostatically (i.e., Airy) generated bathymetry has been calculated for a range of elastic thickness values, T_e (Figures B1b–B1f). Significant flexural deflections are confined to regions with the steepest gradients of loading (e.g., coastlines), with minimal effects across the basin itself. Moreover, even for $T_e = 40$ km, flexural bending has wavelengths of order ~250 km, which is significantly shorter than the >1000 km wavelengths associated with observed dynamic topography [*Hoggard et al.*, 2016].

Appendix C: Residual Topography From Ship-Track Database

Many published residual topographic syntheses use global sedimentary and crustal thickness grids [e.g., *Colin and Fleitout*, 1990; *Panasyuk and Hager*, 2000; *Kaban et al.*, 2003; *Steinberger*, 2007; *Crosby and McKenzie*, 2009]. In order to supplement accurate residual depth point observations, a similar global synthesis is presented here that exploits corrections defined in the main text. Water depths were extracted from the database of *Smith and Sandwell* [1997] using only hull-mounted bathymetric measurements from a ship-track database. The sedimentary correction was applied using thicknesses taken from the NGDC global grid of *Divins* [2003]. This representation was infilled in locations with a lack of measurements using the synthesis of *Laske and Masters* [1997]. Comparison between our accurate sedimentary thickness measurements with these global grids shows that there are significant errors in locations with thick sedimentary piles, particularly in regions adjacent to continental margins and with significant basement topography [e.g., *Whittaker et al.*, 2013; *Wobbe et al.*, 2014]. These correlations are presented in the supporting information. Any regions with sedimentary thickness greater than 1.5 km within the global grid have been excised from the ship-track residual topography.

The crustal correction has been generally omitted due to the absence of a sufficiently accurate global crustal thickness grid for the oceanic realm. Compilations such as CRUST1.0 are constructed from a variety of data sources with variable resolution and accuracy that are subsequently extrapolated into regions with no original measurements [*Laske et al.*, 2013]. Here areas of known anomalous crustal thickness have been excised by detailed mapping carried out on bathymetric and gravity anomaly grids which clearly delimit seamounts, oceanic plateaux, fracture zones, and flexural moats. These data sources and exclusion polygons are included in the supporting information, and the resultant residual topography is plotted in Figure 10. An exception occurs in the North Atlantic Ocean in the vicinity of Iceland, where a crustal correction has been applied using the crustal thickness grid of *Winterbourne et al.* [2014].

Our spot measurements of residual depth correspond to 2297 points for 1° binning, in contrast to 11,127 from ship-track observations. Note that for 4° binning, spots measurements contribute 757 points, whereas ship-track observations yield 1039. There is a good agreement between residual depths calculated from spot measurements and ship-track observations (supporting information). The best-fit relationship follows a one-to-one ratio with 41% of measurements falling within 100 m of this relationship and 77% within 250 m. The Pearson's correlation coefficient is ~0.9.

Appendix D: Additional Residual Depth Maps

D1. Eastern North America

The western central Atlantic Ocean is shown in Figure D1. The east North American margin is characterized by negative residual depths, with drawdown of −1.2 km occurring south of Nova Scotia. Residual depth anomalies rise to −350 m near Maine and remain approximately constant southward in the vicinity of Georgia. Southeast Florida and the Bahamas have residual topography of +400 m. A large negative anomaly stretches out toward the Mid-Atlantic Ridge and surrounds an ~800 km wide swell of neutral to +500 m, known as the Bermuda Rise. The Bermuda seamount was active until at least ~30 Ma and is associated with the final stages of upwelling of a mantle plume [*Vogt and Jung*, 2007]. Seismic evidence based upon shear-wave splitting and mantle transition zone thinning suggests that vertical flow of hot buoyant material within the mantle is still ongoing, despite the apparent cessation of volcanism [*Benoit et al.*, 2013]. A low shear-wave velocity

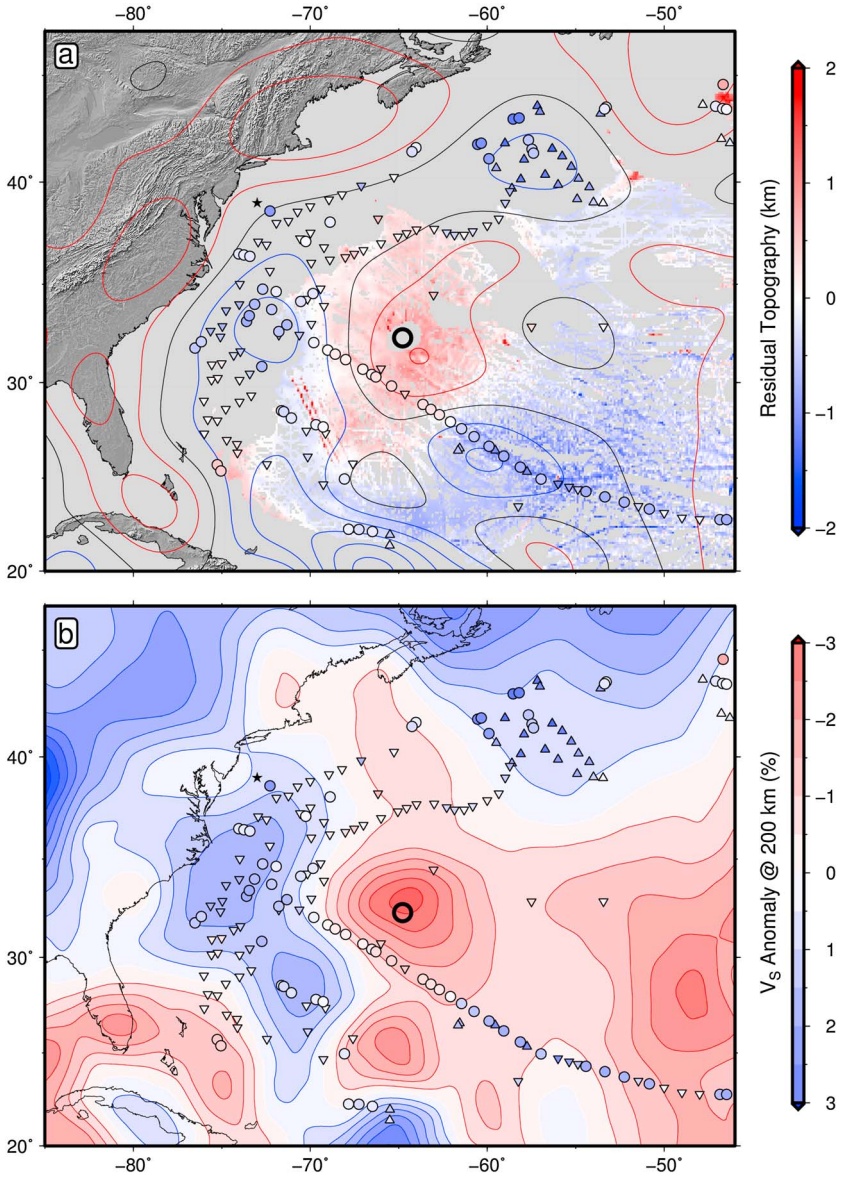

Figure D1. Residual topography of eastern North America. (a) Residual depth anomalies averaged in 1° bins. Symbols and ship-track data as in Figure 10; contours = non-hydrostatic free-air gravity anomalies from GOCO05S database, band-pass ($9000 > \lambda > 730$ km) filtered and plotted every 10 mGal [*Mayer-Guerr*, 2015]; black ring = Bermuda seamount [*Courtillot et al.*, 2003]; black star = COST B-2 well. (b) Horizontal slice at depth of 200 km through SL2013sv tomographic model contoured every 0.5% [*Schaeffer and Lebedev*, 2013]. Residual depth measurements as in Figure D1a.

anomaly has been imaged beneath the seamount [*Schaeffer and Lebedev*, 2013]. The Bermuda Rise is also visible in the long-wavelength gravity field, although the anomaly pattern appears to have been shifted to more negative values.

Recent uplift rates estimated from emergent coastline deposits are complicated by large-amplitude and ongoing vertical motions associated with glacial isostatic adjustment. This behavior occurs in addition to dynamic topography effects and can overprint it, although the growth and decay of ice sheets and their deformational timescales are significantly shorter. A mid-Pliocene (3.1 ± 0.2 Ma) shoreline, known as the Orangeburg Scarp, can be traced from Virginia down to south Georgia at elevations of 40–80 m above present-day sea-level [*Rovere et al.*, 2015]. Eocene and Miocene paleoshorelines along the New Jersey coastal plain have been compared to global sea-level curves and record 50–200 m of anomalous post-Eocene subsidence [*Spasojević et al.*, 2008].

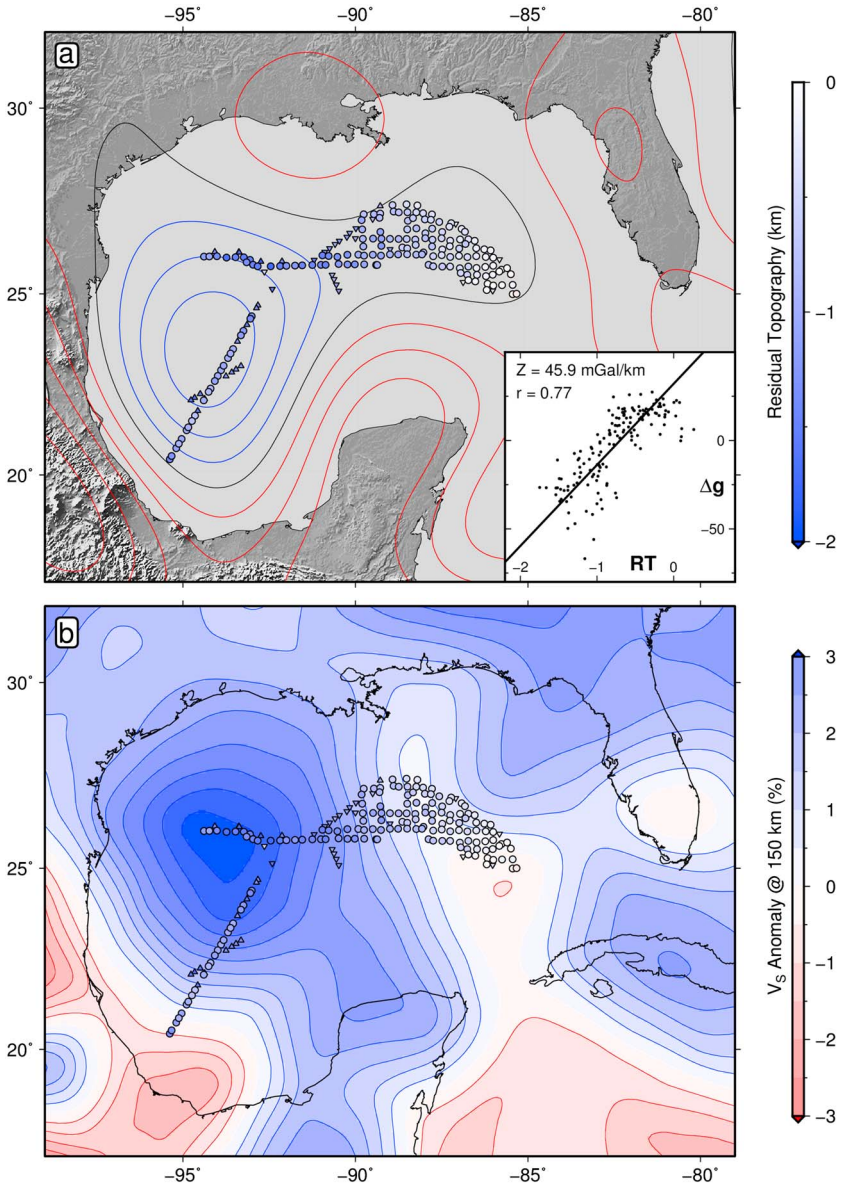

Figure D2. Residual topography of the Gulf of Mexico. (a) Residual depth anomalies averaged in 0.25° bins. Symbols as in Figure 10; contours = non-hydrostatic free-air gravity anomalies from GOCO05S database, low-pass (> 730 km) filtered and plotted every 10 mGal [*Mayer-Guerr*, 2015]. Inset shows unfiltered free-air gravity anomaly plotted as function of residual depth [*Sandwell et al.*, 2014]; solid line = best-fit linear admittance of $Z = 45.9$ mGal km^{-1} calculated using nonbiased linear regression method of *Marks and Sandwell* [1991]; $r = 0.77$ is Pearson's correlation coefficient. (b) Horizontal slice at depth of 150 km through SL2013sv tomographic model contoured every 0.5% [*Schaeffer and Lebedev*, 2013]. Residual depth measurements from Figure D2a.

Offshore New Jersey, the COST B-2 well was drilled in 1976 in the Baltimore Canyon Trough region and has an anomalous subsidence event of ~250 m initiating at 16 Ma and continuing until the present day [*Flament et al.*, 2013]. Mantle convective circulation models have related this event to dynamic topography associated with sinking of the Farallon slab into the lower mantle [*Spasojević et al.*, 2008; *Flament et al.*, 2013]. An alternative model predicts Neogene uplift for this region [*Moucha et al.*, 2008].

These observations underline the difficulties of reconstructing global sea-level curves from individual localities. The relationship published by *Miller et al.* [2005] was based on backstripping of five wells from the New Jersey area on the basis that this margin is tectonically stable. However, residual depth anomalies and other independent geological constraints show that this region is probably still deforming. Dynamic topographic

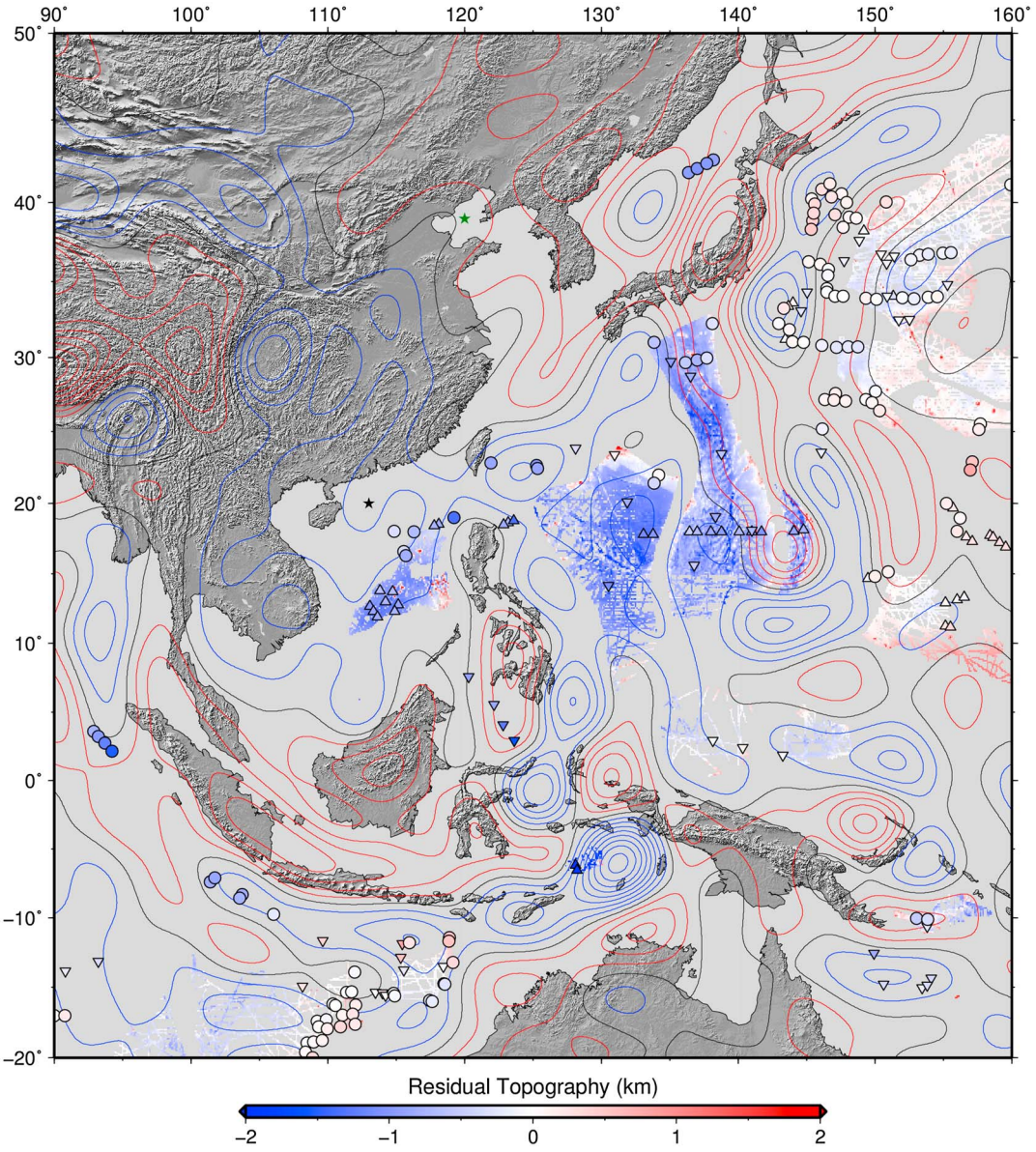

Figure D3. Residual topography of Southeast Asia. (a) Residual depth anomalies averaged in 1° bins. Symbols as in Figure 10; contours = non-hydrostatic free-air gravity anomalies from GOCO05S database, band-pass ($9000 > \lambda > 730$ km) filtered and plotted every 10 mGal [*Mayer-Guerr*, 2015]. Black star = borehole from South China Sea [*Wheeler and White*, 2000]; green star = borehole from Bohai Basin [*Wheeler and White*, 2002].

and glacio-isostatic adjustment effects are ubiquitous, and hence, sea-level curves based upon local measurements of vertical motions must be treated with caution [*Müller et al.*, 2008b; *Flament et al.*, 2013; *Austermann et al.*, 2013].

D2. Gulf of Mexico

The oceanic crust within the Gulf of Mexico was generated at a Jurassic spreading center [*Pindell and Kennan*, 2009]. Rifting occurred when the Yucatan block rotated counterclockwise away from the Louisiana margin along a major transform fault running north-south at the western margin that forms part of the Tamaulipas-Golden Lane-Chiapas fracture zone. Rifting is believed to have ended in Early Cretaceous times. Seismic reflection profiles were acquired using state-of-the-art, industry-standard acquisition and processing techniques. Imaging of Moho reflections is excellent despite the presence of a thick sedimentary package. These profiles have yielded a well-resolved pattern of residual depth anomalies (Figure D2). Unfortunately, the distribution of observed anomalies is limited in the north due to the presence of major allochthonous salt

diapirs of the Perdido, Sigsbee Escarpment, and Atwater Valley fold belts, which limit acoustic penetration and recovery of basement structure. There is a paucity of measurements south of United States of America territorial waters. Residual depth anomalies define a smooth gradient from zero to −1.5 km westward across the basin which yields a gradient of 1 m km^{-1}. This pattern is closely matched by long-wavelength gravity anomalies which coincide with fast shear-wave velocity anomalies within the upper mantle.

The timing of this drawdown is difficult to constrain due to complex halokinesis. Backstripped subsidence records from wells along the continental shelf are plentiful and have robust age and paleowater-depth constraints. However, these records are strongly affected by mid-Miocene to recent anomalous subsidence events generated by evacuation of Late Jurassic salt as it becomes gravitationally unstable and flows downslope [*Angeles-Aquino et al.*, 1994; *Peel et al.*, 1995]. This behavior is driven by marginal overburden and can be initiated by fractional increases in basinward tilt [*Rowan et al.*, 2004]. Drawdown within the central basin may be responsible for destabilizing this salt layer. This tilting is also consistent with the pattern of Miocene uplift of onshore Mexico and the Western United States derived from drainage analysis [*Stephenson et al.*, 2014].

D3. Southeast Asia

Southeast Asia is characterized by broadly negative residual topography (Figure D3). Anomalies within the South China Sea are approximately −600 m, decreasing southeastward to −900 m within the Sulu Sea and −1.6 km within the Celebes Sea south of the Philippines. The Banda Sea sits at −2.5 km and is the largest drawdown observed within the database. It is almost completely encircled by subduction zones that are probably the primary cause of downwelling. To the north of Papua New Guinea, the southern Philippine Sea has neutral residual topography, while most of the central basin is drawn down by about −800 m. East of the Marianas Trench, residual depths vary from neutral in the south up to +300 m off the eastern margin of Japan. Finally, behind the subduction zone within the Sea of Japan, negative anomalies of −900 m have been measured.

Estimates for the timing of drawdown within the South China Sea have been determined by backstripping multiple wells and correcting for tectonic subsidence caused by lithospheric extension and cooling [*Wheeler and White*, 2000; *Xie et al.*, 2006]. These analyses reveal ∼300 m of anomalous subsidence that initiated at 5–10 Ma and continues with a present-day rate of 0.1 mm yr^{-1}. Similar work from the Bohai Basin west of the Korean peninsula reveals an ∼400 m anomalous subsidence event at 8 Ma [*Wheeler and White*, 2002].

Acknowledgments

This research is supported by a BP-Cambridge collaboration. We are grateful to D. Al-Attar, J. Austermann, A. Bump, R. Corfield, A. Crosby, M. Falder, I. Frame, D. Glassey, S. Ghelichkhan, T. Heyn, N. Hodgson, A. Jackson, S. Kisin, P. Koelemeijer, D. Lyness, L. Mackay, D. McKenzie, F. Richards, T. Sabato Ceraldi, O. Shorttle, E. Stirling, S. Stephenson, and M. Thompson for their help. We thank B. Horn and K. McDermott from ION Geophysical Corporation for permission to publish partial seismic reflection profiles shown in Figure 2 from their IndiaSPAN™, East AfricaSPAN™, PelotasSPAN™, GulfSPAN™, and Greater BrasilSPAN™ data sets. B. Steinberger and S. Zhong provided insightful reviews. Figures were prepared using Generic Mapping Tools version 5 [*Wessel et al.*, 2013]. Routines from the SHTOOLS package were used in the spherical harmonic analysis. Residual depth measurements and seismic survey sources are in the supporting information and in the University of Cambridge online repository (https://doi.org/10.17863/CAM.8286). The authors declare no competing financial interests. Earth Sciences contribution esc.3794.

References

Abrams, L. J., R. S. Detrick, and P. J. Fox (1988), Morphology and crustal structure of the Kane Fracture Zone transverse ridge, *J. Geophys. Res.*, *93*(B4), 3195–3210.

Afilhado, A., L. Matias, H. Shiobara, A. Hirn, L. Mendes-Victor, and H. Shimamura (2008), From unthinned continent to ocean: The deep structure of the West Iberia passive continental margin at 38°N, *Tectonophysics*, *458*, 9–50, doi:10.1016/j.tecto.2008.03.002.

Airy, G. B. (1855), On the computation of the effect of the attraction of mountain-masses, as distributing the apparent astronomical latitude of stations in geodetic surveys, *Philos. Trans. R. Soc.*, *145*, 101–104.

Al-Hajri, Y., N. J. White, and S. Fishwick (2009), Scales of transient convective support beneath Africa, *Geology*, *37*(10), 883–886, doi:10.1130/G25703A.1.

Altenbernd, T., W. Jokat, I. Heyde, and V. Damm (2014), A crustal model for northern Melville Bay, Baffin Bay, *J. Geophys. Res. Solid Earth*, *119*, 8610–8632, doi:10.1002/2014JB011559.

Altenbernd, T., W. Jokat, I. Heyde, and V. Damm (2015), Geophysical evidence for the extent of crustal types and the type of margin along a profile in the northeastern Baffin Bay, *J. Geophys. Res. Solid Earth*, *120*, 7337–7360, doi:10.1002/2015JB012352.

Anderson, R. N., D. J. Spariosu, J. K. Weissel, and D. E. Hayes (1980), The interrelation between variations in magnetic anomaly amplitudes and basalt magnetization and chemistry along the Southeast Indian Ridge, *J. Geophys. Res.*, *85*(B7), 3883–3898, doi:10.1029/JB085iB07p03883.

Angeles-Aquino, F. J., J. Reyes-Nunez, J. M. Quezada-Muneton, and J. J. Meneses-Rocha (1994), Tectonic evolution, structural styles, and oil habitat in Campeche Sound, Mexico, *Gulf Coast Assoc. Geol. Soc. Trans.*, *44*, 53–62.

Angulo, R. J., G. C. Lessa, and M. C. de Souza (2006), A critical review of mid- to late-Holocene sea-level fluctuations on the eastern Brazilian coastline, *Quat. Sci. Rev.*, *25*, 486–506, doi:10.1016/j.quascirev.2005.03.008.

Antoine, J., and J. Ewing (1963), Seismic refraction measurements on the margins of the Gulf of Mexico, *J. Geophys. Res.*, *68*(7), 1975–1996, doi:10.1029/JZ068i007p01975.

Arai, R., T. Takahashi, S. Kodaira, Y. Kaiho, A. Nakanishi, G. Fujie, Y. Nakamura, Y. Yamamoto, Y. Ishihara, S. Miura, and Y. Kaneda (2016), Structure of the tsunamigenic plate boundary and low-frequency earthquakes in the southern Ryukyu Trench, *Nat. Commun.*, *7*, 12255, doi:10.1038/ncomms12255.

Arlot, S., and A. Celisse (2010), A survey of cross-validation procedures for model selection, *Stat. Surv.*, *4*, 40–79, doi:10.1214/09-SS054.

Athy, L. F. (1930), Density, porosity, and compaction of sedimentary rocks, *AAPG Bull.*, *14*(1), 1–24, doi:10.1306/3D93289E-16B1-11D7-8645000102C1865D.

Austermann, J., J. X. Mitrovica, K. Latychev, and G. A. Milne (2013), Barbados-based estimate of ice volume at Last Glacial Maximum affected by subducted plate, *Nat. Geosci.*, *6*(7), 553–557, doi:10.1038/ngeo1859.

Austin, J. A., and E. Uchupi (1982), Continental-oceanic crustal transition off Southwest Africa, *AAPG Bull.*, *66*(9), 1328–1347, doi:10.1306/03B5A79B-16D1-11D7-8645000102C1865D.

Ball, P. J. (2005), Break-up history and evolution of the southern passive margin of Australia, PhD thesis, Royal Holloway Univ. of London.

Barreto, A. M. F., F. H. R. Bezerra, K. Suguio, S. H. Tatumi, M. Yee, R. P. Paiva, and C. S. Munita (2002), Late Pleistocene marine terrace deposits in northeastern Brazil: Sea-level change and tectonic implications, *Palaeogeogr. Palaeoclimatol. Palaeoecol.*, *179*, 57–69, doi:10.1016/S0031-0182(01)00408-4.

Barton, A. J., and R. S. White (1997), Crustal structure of Edoras Bank continental margin and mantle thermal anomalies beneath the North Atlantic, *J. Geophys. Res.*, *102*(B2), 3109–3129, doi:10.1029/96JB03387.

Barton, P., T. Owen, and R. White (1990), The deep structure of the east Oman continental margin: Preliminary results and interpretation, *Tectonophysics*, *173*, 319–331, doi:10.1016/0040-1951(90)90227-Y.

Bauer, K., S. Neben, B. Schreckenberger, R. Emmermann, K. Hinz, N. Fechner, K. Gohl, A. Schulze, R. Trumbull, and K. Weber (2000), Deep structure of the Namibia continental margin as derived from integrated geophysical studies, *J. Geophys. Res.*, *105*(B11), 25,829–25,853.

Becker, J. J., et al. (2009), Global bathymetry and elevation data at 30 arc seconds resolution: SRTM30_PLUS, *Mar. Geod.*, *32*(4), 355–371, doi:10.1080/01490410903297766.

Ben-Avraham, Z., A. Ginzburg, J. Makris, and L. Eppelbaum (2002), Crustal structure of the Levant Basin, eastern Mediterranean, *Tectonophysics*, *346*, 23–43, doi:10.1016/S0040-1951(01)00226-8.

Benoit, M. H., M. D. Long, and S. D. King (2013), Anomalously thin transition zone and apparently isotropic upper mantle beneath Bermuda: Evidence for upwelling, *Geochem. Geophys. Geosyst.*, *14*, 4282–4291, doi:10.1002/ggge.20277.

Beslier, M.-O., M. Ask, and G. Boillot (1993), Ocean-continent boundary in the Iberia Abyssal Plain from multichannel seismic data, *Tectonophysics*, *218*, 383–393, doi:10.1016/0040-1951(93)90327-G.

Bezerra, F. H. R., A. M. F. Barreto, and K. Suguio (2003), Holocene sea-level history on the Rio Grande do Norte State coast, Brazil, *Mar. Geol.*, *196*, 73–89, doi:10.1016/S0025-3227(03)00044-6.

Brace, W. F., and J. D. Byerlee (1970), California earthquakes: Why only shallow focus?, *168*, 1573–15,755, doi:10.1126/science.168.3939.1573.

Breivik, A. J., R. Mjelde, P. Grogan, H. Shimamura, Y. Murai, and Y. Nishimura (2003), Crustal structure and transform margin development south of Svalbard based on ocean bottom seismometer data, *Tectonophysics*, *369*, 37–70, doi:10.1016/S0040-1951(03)00131-8.

Breivik, A. J., R. Mjelde, J. I. Faleide, and Y. Murai (2006), Rates of continental breakup magmatism and seafloor spreading in the Norway Basin-Iceland plume interaction, *J. Geophys. Res.*, *111*, B07102, doi:10.1029/2005JB004004.

Bry, M., and N. White (2007), Reappraising elastic thickness variation at oceanic trenches, *J. Geophys. Res.*, *112*, B08414, doi:10.1029/2005JB004190.

Buck, W. R., C. Small, and W. B. F. Ryan (2009), Constraints on asthenospheric flow from the depths of oceanic spreading centers: The East Pacific Rise and the Australian-Antarctic Discordance, *Geochem. Geophys. Geosyst.*, *10*, Q09007, doi:10.1029/2009GC002373.

Bullock, A. D., and T. A. Minshull (2005), From continental extension to seafloor spreading: Crustal structure of the Goban Spur rifted margin, southwest of the UK, *Geophys. J. Int.*, *163*, 527–546, doi:10.1111/j.1365-246X.2005.02726.x.

Bunce, E. T., and P. Molnar (1977), Seismic reflection profiling and basement topography in the Somali Basin: Possible fracture zones between Madagascar and Africa, *J. Geophys. Res.*, *82*(33), 5305–5311.

Canales, J. P., R. Detrick, S. Bazin, A. Harding, and J. Orcutt (1998), Off-axis crustal thickness across and along the East Pacific Rise within the MELT area, *Science*, *280*, 1218–1221, doi:10.1126/science.280.5367.1218.

Canales, J. P., G. Ito, R. S. Detrick, and J. Sinton (2002), Crustal thickness along the western Galapagos Spreading Center and the compensation of the Galapagos hotspot swell, *Earth Planet. Sci. Lett.*, *203*, 311–327, doi:10.1016/S0012-821X(02)00843-9.

Canales, J. P., R. S. Detrick, D. R. Toomey, and W. S. D. Wilcock (2003), Segment-scale variations in the crustal structure of 150–300 kyr old fast spreading oceanic crust (East Pacific rise, 8°15′N–10°5′N) from wide-angle seismic refraction profiles, *Geophys. J. Int.*, *152*(3), 766–794, doi:10.1046/j.1365-246X.2003.01885.x.

Carbotte, S. M., M. R. Nedimović, J. P. Canales, G. M. Kent, A. J. Harding, and M. Marjanović (2008), Variable crustal structure along the Juan de Fuca Ridge: Influence of on-axis hot spots and absolute plate motions, *Geochem. Geophys. Geosyst.*, *9*, Q08001, doi:10.1029/2007GC001922.

Caress, D. W., M. K. McNutt, R. S. Detrick, and J. C. Mutter (1995), Seismic imaging of hotspot-related crustal underplating beneath the Marquesas Islands, *Nature*, *373*(2), 600–603, doi:10.1038/373600a0.

Carlson, R. L., and C. N. Herrick (1990), Densities and porosities in the oceanic crust and their variations with depth and age, *J. Geophys. Res.*, *95*(B6), 9153–9170, doi:10.1029/JB095iB06p09153.

Carlson, R. L., A. F. Gangi, and K. R. Snow (1986), Empirical reflection travel time versus depth and velocity versus depth functions for the deep-sea sediment column, *J. Geophys. Res.*, *91*(B8), 8249–8266, doi:10.1029/JB091iB08p08249.

Cazenave, A., and B. Lago (1991), Long wavelength topography, seafloor subsidence and flattening, *Geophys. Res. Lett.*, *18*(7), 1257–1260.

Cazenave, A., K. Dominh, C. J. Allegre, and J. G. Marsh (1986), Global relationship between oceanic geoid and topography, *J. Geophys. Res.*, *91*(B11), 11,439–11,450, doi:10.1029/JB091iB11p11439.

Cazenave, A., K. Dominh, M. Rabinowicz, and G. Ceuleneer (1988), Geoid and depth anomalies over ocean swells and troughs: Evidence of an increasing trend of the geoid to depth ratio with age of plate, *J. Geophys. Res.*, *93*(B7), 8064–8077, doi:10.1029/JB093iB07p08064.

Chambat, F., Y. Ricard, and B. Valette (2010), Flattening of the Earth: Further from hydrostaticity than previously estimated, *Geophys. J. Int.*, *183*, 727–732, doi:10.1111/j.1365-246X.2010.04771.x.

Charvis, P., A. Laesanpura, J. Gallart, A. Hirn, J.-C. Lépine, B. de Voogd, T. A. Minshull, Y. Hello, and B. Pontoise (1999), Spatial distribution of hotspot material added to the lithosphere under La Réunion, from wide-angle seismic data, *J. Geophys. Res.*, *104*(B2), 2875–2893, doi:10.1029/98JB02841.

Chetty, P., and R. Green (1977), Seismic refraction observations in the Transkei Basin and adjacent areas, *Mar. Geophys. Res.*, *3*, 197–208.

Chian, D., and K. E. Louden (1994), The continent-ocean crustal transition across the southwest Greenland margin, *J. Geophys. Res.*, *99*(B5), 9117–9135.

Chian, D., K. E. Louden, and I. Reid (1995), Crustal structure of the Labrador Sea conjugate margin and implications for the formation of nonvolcanic continental margins, *J. Geophys. Res.*, *100*(B12), 24,239–24,253, doi:10.1029/95JB02162.

Chian, D., I. D. Reid, and H. R. Jackson (2001), Crustal structure beneath Orphan Basin and implications for nonvolcanic continental rifting, *J. Geophys. Res.*, *106*(B6), 10,923–10,940, doi:10.1029/2000JB900422.

Christensen, N. I. (1982), Seismic velocities, in *Handbook of Physical Properties of Rocks*, vol. 2, edited by R. S. Carmichael, pp. 57–74, CRC Press, Boca Raton, Fla.

Christeson, G. L., S. P. S. Gulick, H. J. A. van Avendonk, L. L. Worthington, R. S. Reece, and T. L. Pavlis (2010), The Yakutat terrane: Dramatic change in crustal thickness across the Transition fault, Alaska, *Geology*, *38*(10), 895–898, doi:10.1130/G31170.1.

Christeson, G. L., H. J. A. Van Avendonk, I. O. Norton, J. W. Snedden, D. R. Eddy, G. D. Karner, and C. A. Johnson (2014), Deep crustal structure in the eastern Gulf of Mexico, *J. Geophys. Res. Solid Earth*, *119*, 6782–6801, doi:10.1002/2014JB011045.

Christie, D. M., D. G. Pyle, R. B. Pedersen, and D. J. Miller (2004), Leg 187 synthesis: Evolution of the Australian Antarctic Discordance, the Australian Antarctic depth anomaly, and the Indian/Pacific mantle isotopic boundary, in *Proceedings of the Ocean Drilling Program, Scientific Results*, chap. 1, vol. 187, edited by R. B. Pedersen, D. M. Christie, and D. J. Miller, pp. 1–41.

Cochran, J. R. (1983), A model for development of Red Sea, *AAPG Bulletin*, *67*(1), 41–69, doi:10.1306/03B5ACBE-16D1-11D7-8645000102C1865D.

Cochran, J. R., and M. Talwani (1977), Free-air gravity anomalies in the world's oceans and their relationship to residual elevation, *Geophys. J. R. Astron. Soc.*, *50*, 495–552.

Coffin, M., P. Rabinowitz, and R. Houtz (1986), Crustal structure in the Western Somali Basin, *Geophys. J. R. Aston. Soc.*, *86*, 331–369.

Colin, P., and L. Fleitout (1990), Topography of the ocean floor: Thermal evolution of the lithosphere and interaction of deep mantle heterogeneities with the lithosphere, *Geophys. Res. Lett.*, *17*(11), 1961–1964.

Collier, J. S., and A. B. Watts (2001), Lithospheric response to volcanic loading by the Canary Islands: Constraints from seismic reflection data in their flexural moat, *Geophys. J. Int.*, *147*, 660–676, doi:10.1046/j.0956-540x.2001.01506.x.

Collier, J. S., T. J. Henstock, C. Peirce, and A. B. Watts (1998), A detailed geophysical study in the Canary Basin (eastern Atlantic): Implications for the internal structure of 130 Ma oceanic crust, *Geophys. J. Int.*, *135*, 943–963, doi:10.1046/j.1365-246X.1998.00675.x.

Collier, J. S., T. A. Minshull, J. O. S. Hammond, R. B. Whitmarsh, J.-M. Kendall, V. Sansom, C. I. Lane, and G. Rumpker (2009), Factors influencing magmatism during continental breakup: New insights from a wide-angle seismic experiment across the conjugate Seychelles-Indian margins, *J. Geophys. Res.*, *114*, B03101, doi:10.1029/2008JB005898.

Contreras-Reyes, E., I. Grevemeyer, E. R. Flueh, and C. Reichert (2008), Upper lithospheric structure of the subduction zone offshore of southern Arauco peninsula, Chile, at ~38°S, *J. Geophys. Res.*, *113*, B07303, doi:10.1029/2007JB005569.

Contreras-Reyes, E., I. Grevemeyer, A. B. Watts, L. Planert, E. Flueh, and C. Peirce (2010), Crustal intrusion beneath the Louisville hotspot track, *Earth Planet. Sci. Lett.*, *289*, 323–333, doi:10.1016/j.epsl.2009.11.020.

Contreras-Reyes, E., J. Becerra, H. Kopp, C. Reichert, and J. Díaz-Naveas (2014), Seismic structure of the north-central Chilean convergent margin: Subduction erosion of a paleomagmatic arc, *Geophys. Res. Lett.*, *41*, 1523–1529, doi:10.1002/2013GL058954.

Contreras-Reyes, E., J. a. Ruiz, J. Becerra, H. Kopp, C. Reichert, A. Maksymowicz, and C. Arriagada (2015), Structure and tectonics of the central Chilean margin (31°–33°S): Implications for subduction erosion and shallow crustal seismicity, *Geophys. J. Int.*, *203*, 776–791, doi:10.1093/gji/ggv309.

Contrucci, I., F. Klingelhöfer, J. Perrot, R. Bartolome, M. Gutscher, M. Sahabi, J. Malod, and J.-P. Rehault (2004a), The crustal structure of the NW Moroccan continental margin from wide-angle and reflection seismic data, *Geophys. J. Int.*, *159*, 117–128, doi:10.1111/j.1365-246X.2004.02391.x.

Contrucci, I., et al. (2004b), Deep structure of the West African continental margin (Congo, Zaire, Angola), between 5°S and 8°S, from reflection/refraction seismics and gravity data, *Geophys. J. Int.*, *158*, 529–553, doi:10.1111/j.1365-246X.2004.02303.x.

Cooper, A. K., M. S. Marlow, D. W. Scholl, and A. J. Stevenson (1992), Evidence for Cenozoic crustal extension in the Bering Sea region, *Tectonics*, *11*(4), 719–731.

Cordani, U. G. (1970), Idade do vulcanismo no Oceano Atlantico Sul, *Boletim IGA*, *1*, 9–75.

Corredor, F., J. H. Shaw, and F. Bilotti (2005), Structural styles in the deep-water fold and thrust belts of the Niger Delta, *AAPG Bull.*, *89*(6), 753–780, doi:10.1306/02170504074.

Courtillot, V., A. Davaille, J. Besse, and J. Stock (2003), Three distinct types of hotspots in the Earth's mantle, *Earth Planet. Sci. Lett.*, *205*(3–4), 295–308, doi:10.1016/S0012-821X(02)01048-8.

Craig, T. J., and A. Copley (2014), An explanation for the age independence of oceanic elastic thickness estimates from flexural profiles at subduction zones, and implications for continental rheology, *Earth Planet. Sci. Lett.*, *392*, 207–216, doi:10.1016/j.epsl.2014.02.027.

Crosby, A. G., and D. P. McKenzie (2009), An analysis of young ocean depth, gravity and global residual topography, *Geophys. J. Int.*, *178*, 1198–1219, doi:10.1111/j.1365-246X.2009.04224.x.

Crosby, A. G., D. P. McKenzie, and J. G. Sclater (2006), The relationship between depth, age and gravity in the oceans, *Geophys. J. Int.*, *166*, 553–573, doi:10.1111/j.1365-246X.2006.03015.x.

Crough, S. T. (1983a), The correction for sediment loading on the seafloor, *J. Geophys. Res.*, *88*(B8), 6449–6454, doi:10.1029/JB088iB08p06449.

Crough, S. T. (1983b), Hotspot swells, *Ann. Rev. Earth Planet. Sci.*, *11*, 165–193.

Crough, S. T., and R. D. Jarrard (1981), The Marquesas-Line Swell, *J. Geophys. Res.*, *86*(B12), 11,763–11,771.

Curray, J. R., G. G. Shor, R. W. Raitt, and M. Henry (1977), Seismic refraction and reflection studies of crustal structure of the Eastern Sunda and Western Banda Arcs, *J. Geophys. Res.*, *82*(17), 2479–2489.

Czarnota, K., M. J. Hoggard, N. J. White, and J. Winterbourne (2013), Spatial and temporal patterns of Cenozoic dynamic topography around Australia, *Geochem. Geophys. Geosyst.*, *14*, 634–658, doi:10.1029/2012GC004392.

Czuba, W., O. Ritzmann, Y. Nishimura, M. Grad, R. Mjelde, A. Guterch, and W. Jokat (2005), Crustal structure of northern Spitsbergen along the deep seismic transect between the Molloy Deep and Nordaustlandet, *Geophys. J. Int.*, *161*, 347–364, doi:10.1111/j.1365-246X.2005.02593.x.

Dalton, C. A., C. H. Langmuir, and A. Gale (2014), Geophysical and geochemical evidence for deep temperature variations beneath mid-ocean ridges, *Science*, *344*, 80–83.

Davies, D. R., and J. H. Davies (2009), Thermally-driven mantle plumes reconcile multiple hot-spot observations, *Earth Planet. Sci. Lett.*, *278*, 50–54, doi:10.1016/j.epsl.2008.11.027.

Davies, G. F., and F. Pribac (1993), Mesozoic Seafloor Subsidence and the Darwin Rise, Past and Present, in *The Mesozoic Pacific: Geology, Tectonics, and Volcanism—A Volume in Memory of Sy Schlanger, Geophys. Monogr. Ser.*, vol. 77, pp. 39–52, AGU, Washington, D. C.

de Voogd, B., C. Truffert, N. Chamot-Rooke, P. Huchon, S. Lallemant, and X. Pichon (1992), Two-ship deep seismic soundings in the basins of the Eastern Mediterranean Sea (Pasiphae cruise), *Geophys. J. Int.*, *109*, 536–552, doi:10.1111/j.1365-246X.1992.tb00116.x.

Dean, S. M., T. A. Minshull, R. B. Whitmarsh, and K. E. Louden (2000), Deep structure of the ocean-continent transition in the southern Iberia Abyssal Plain from seismic refraction profiles: The IAM-9 transect at 40°20′N, *J. Geophys. Res.*, *105*(B3), 5859–5885.

Delescluse, M., T. Funck, S. A. Dehler, K. E. Louden, and L. Watremez (2015), The oceanic crustal structure at the extinct, slow to ultraslow Labrador Sea spreading center, *J. Geophys. Res. Solid Earth*, *120*, 5249–5272, doi:10.1002/2014JB011739.

Delorey, A. A., R. A. Dunn, and J. B. Gaherty (2007), Surface wave tomography of the upper mantle beneath the Reykjanes Ridge with implications for ridge-hot spot interaction, *J. Geophys. Res.*, *112*, B08313, doi:10.1029/2006JB004785.

Den, N., W. J. Ludwig, S. Murauchi, J. I. Ewing, H. Hotta, N. T. Edgar, T. Yoshii, T. Asanuma, K. Hagiwara, T. Sato, and S. Ando (1969), Seismic-refraction measurements in the Northwest Pacific Basin, *J. Geophys. Res.*, *74*(6), 1421–1434.

Den, N., W. J. Ludwig, S. Murauchi, M. Ewing, H. Hotta, T. Asanuma, T. Yoshii, A. Kubotera, and K. Hagiwara (1971), Sediments and structure of the Eauripik-New Guinea Rise, *J. Geophys. Res.*, *76*, 4711–4723, doi:10.1029/JB076i020p04711.

Detrick, R. S., and G. M. Purdy (1980), The crustal structure of the kane fracture zone from seismic refreaction studies, *J. Geophys. Res.*, *85*(B7), 3759–3777.
Divins, D. L. (2003), *Total Sediment Thickness of the World's Oceans and Marginal Seas*, NOAA Natl. Geophys. Data Center, Boulder, Colo.
Dziewonski, A. M., T.-A. Chou, and J. H. Woodhouse (1981), Determination of earthquake source parameters from waveform data for studies of global and regional seismicity, *J. Geophys. Res.*, *86*(B4), 2825–2852, doi:10.1029/JB086iB04p02825.
Ebeniro, J. O., Y. Nakamura, D. S. Sawyer, and W. P. O'Brien (1988), Sedimentary and crustal structure of the northwestern Gulf of Mexico, *J. Geophys. Res.*, *93*(B8), 9075–9092.
Edwards, R. A., R. B. Whitmarsh, and R. A. Scrutton (1997), The crustal structure across the transform continental margin off Ghana, eastern equatorial Atlantic, *J. Geophys. Res.*, *102*(B1), 747–772, doi:10.1029/96JB02098.
Edwards, R. A., T. A. Minshull, E. R. Flueh, and C. Kopp (2008), Dalrymple Trough: An active oblique-slip ocean-continent boundary in the northwest Indian Ocean, *Earth Planet. Sci. Lett.*, *272*, 437–445, doi:10.1016/j.epsl.2008.05.007.
Egloff, F., R. Rihm, J. Makris, Y. Izzeldin, M. Bobsien, K. Meier, P. Junge, T. Noman, and W. Warsi (1991), Contrasting structural styles of the eastern and western margins of the southern Red Sea: The 1988 SONNE experiment, *198*, 329–353, doi:10.1016/0040-1951(91)90159-P.
Ehlers, B.-M., and W. Jokat (2009), Subsidence and crustal roughness of ultra-slow spreading ridges in the northern North Atlantic and the Arctic Ocean, *Geophys. J. Int.*, *177*, 451–462, doi:10.1111/j.1365-246X.2009.04078.x.
Ekström, G., M. Nettles, and A. M. Dziewoński (2012), The global CMT project 2004–2010: Centroid-moment tensors for 13,017 earthquakes, *Phys. Earth Planet. Inter.*, *200-201*, 1–9, doi:10.1016/j.pepi.2012.04.002.
Engdahl, E. R., and A. Villasenor (2002), Global seismicity: 1900–1999, in *International Handbook of Earthquake and Engineering Seismology*, Part A, chap. 41, edited by W. H. K. Lee et al., pp. 665–690, Academic Press.
Ewing, J., and M. Ewing (1959), Seismic-refraction measurements in the Atlantic Ocean basins, in the Mediterranean Sea, on the Mid-Atlantic Ridge, and in the Norwegian Sea, *Bull. Geol. Soc. Am.*, *70*, 291–318.
Ewing, M., L. V. Hawkins, and W. J. Ludwig (1970), Crustal structure of the Coral Sea, *J. Geophys. Res.*, *75*(11), 1953–1962, doi:10.1029/JB075i011p01953.
Fernández-Viejo, G., J. Gallart, J. A. Pulgar, J. Gallastegui, J. J. Danobeitia, and D. Cordoba (1998), Crustal transition between continental and oceanic domains along the North Iberian margin from wide angle seismic and gravity data, *Geophys. Res. Lett.*, *25*(23), 4249–4252.
Flament, N., M. Gurnis, and R. D. Müller (2013), A review of observations and models of dynamic topography, *Lithosphere*, *5*(2), 189–210, doi:10.1130/L245.1.
Fleming, A. (2008), Seismic workstation package, Geoscience, Australia.
Fleming, A. (2010), Acreage release data packages, Geoscience, Australia.
Fleming, A. (2011), Acreage release data package, Geoscience, Australia.
Flueh, E. R., M. A. Fisher, J. Bialas, J. R. Childs, D. Klaeschen, N. Kukowski, T. Parsons, D. W. Scholl, U. ten Brink, A. M. Tréhu, and N. Vidal (1998), New seismic images of hte Cascadia subduction zone from cruise SO108—ORWELL, *Tectonophysics*, *293*, 69–84.
Forste, C., S. L. Bruinsma, F. Flechtner, J.-C. Marty, J.-M. Lemoine, C. Dahle, O. Abrikosov, K. H. Neumayer, R. Biancale, F. Barthelmes, and G. Balmino (2012), A preliminary update of the direct approach GOCE processing and a new release of EIGEN-6C, *Abstract G31B-0923 presented at 2012 Fall Meeting, AGU*, San Francisco, Calif., 3–7 Dec.
Forsyth, D. W., R. L. Ehrenbard, and S. Chapin (1987), Anomalous upper mantle beneath the Australian-Antarctic discordance, *Earth Planet. Sci. Lett.*, *84*, 471–478, doi:10.1016/0012-821X(87)90011-2.
Forte, A. M., W. R. Peltier, A. M. Dziewonski, and R. L. Woodward (1993), Dynamic surface topography: A new interpretation based upon mantle flow models derived from seismic tomography, *Geophys. Res. Lett.*, *20*(3), 225–228, doi:10.1029/93GL00249.
Francis, T. J. G., and R. W. Raitt (1967), Seismic refraction measurements in the southern Indian Ocean, *J. Geophys. Res.*, *72*(12), 3015–3041.
Francis, T. J. G., and G. G. Shor (1966), Seismic refraction measurements in the Northwest Indian Ocean, *J. Geophys. Res.*, *71*(2), 427–449.
Francis, T. J. G., D. Davies, and M. N. Hill (1966), Crustal structure between Kenya and the Seychelles, *Philos. Trans. R. Soc. A*, *259*, 240–261, doi:10.1098/rsta.1966.0010.
Franke, D., S. Neben, S. Ladage, B. Schreckenberger, and K. Hinz (2007), Margin segmentation and volcano-tectonic architecture along the volcanic margin off Argentina/Uruguay, South Atlantic, *Mar. Geol.*, *244*, 46–67, doi:10.1016/j.margeo.2007.06.009.
French, S., V. Lekic, and B. Romanowicz (2013), Waveform tomography reveals channeled flow at the base of the oceanic asthenosphere, *Science*, *342*, 227–231.
Fromm, T., L. Planert, W. Jokat, T. Ryberg, J. H. Behrmann, M. H. Weber, and C. Haberland (2015), South Atlantic opening: A plume-induced breakup?, *Geology*, *43*(10), 931–934, doi:10.1130/G36936.1.
Fujie, G., S. Kodaira, M. Yamashita, T. Sato, T. Takahashi, and N. Takahashi (2013), Systematic changes in the incoming plate structure at the Kuril trench, *Geophys. Res. Lett.*, *40*, 88–93, doi:10.1029/2012GL054340.
Fujie, G., S. Kodaira, T. Sato, and T. Takahashi (2016), Along-trench variations in the seismic structure of the incoming Pacific plate at the outer rise of the northern Japan Trench, *Geophys. Res. Lett.*, *43*, 666–673, doi:10.1002/2015GL067363.
Funck, T., and K. E. Louden (1999), Wide-angle seismic transect across the Torngat Orogen, northern Labrador: Evidence for a Proterozoic crustal root, *J. Geophys. Res.*, *104*, 7463–7480, doi:10.1029/1999JB900010.
Funck, T., J. R. Hopper, H. C. Larsen, K. E. Louden, B. E. Tucholke, and W. S. Holbrook (2003), Crustal structure of the ocean-continent transition at Flemish Cap: Seismic refraction results, *J. Geophys. Res.*, *108*(B11), 2531, doi:10.1029/2003JB002434.
Funck, T., H. R. Jackson, K. E. Louden, S. A. Dehler, and Y. Wu (2004), Crustal structure of the northern Nova Scotia rifted continental margin (eastern Canada), *J. Geophys. Res.*, *109*, B09102, doi:10.1029/2004JB003008.
Funck, T., K. Gohl, V. Damm, and I. Heyde (2012), Tectonic evolution of southern Baffin Bay and Davis Strait: Results from a seismic refraction transect between Canada and Greenland, *J. Geophys. Res.*, *117*, B04107, doi:10.1029/2011JB009110.
Furumoto, A. S., G. P. Woollard, J. F. Campbell, and D. M. Hussong (1968), Variation in the thickness of the crust in the Hawaiian Archipelago, in *The Crust and Upper Mantle of the Pacific Area*, edited by L. Knopoff, C. L. Drake, and P. J. Hart, pp. 94–111, AGU, Washington, D. C.
Furumoto, B. Y. A. S., J. F. Campbell, and D. M. I. Hussong (1971), Seismic refraction surveys along the Hawaiian Ridge, Kauai to Midway Island, *Bull. Seismol. Soc. Am.*, *61*(1), 147–166.
Gailler, A., P. Charvis, and E. R. Flueh (2007), Segmentation of the Nazca and South American Plates along the Ecuador subduction zone from wide angle seismic profiles, *Earth Planet. Sci. Lett.*, *260*, 444–464, doi:10.1016/j.epsl.2007.05.045.
Gailler, A., F. Klingelhöfer, J.-L. Olivet, and D. Aslanian (2009), Crustal structure of a young margin pair: New results across the Liguro-Provencal Basin from wide-angle seismic tomography, *Earth Planet. Sci. Lett.*, *286*, 333–345, doi:10.1016/j.epsl.2009.07.001.
Gale, A., C. A. Dalton, C. H. Langmuir, Y. Su, and J.-G. Schilling (2013), The mean composition of ocean ridge basalts, *Geochem. Geophys. Geosyst.*, *14*, 489–518, doi:10.1029/2012GC004334.
Gardner, J. V. (1970), Submarine geology of the western Coral sea, *Bull. Geol. Soc. Am.*, *81*, 2599–2614, doi:10.1130/0016-7606(1970)81[2599:SGOTWC]2.0.CO;2.

Gass, I. G. (1977), The age and extent of the Red Sea oceanic crust, *Nature*, *265*(2), 722–724, doi:10.1038/265722a0.
Gerdom, M., A. Trehu, E. Flueh, and D. Klaeschen (2000), The continental margin off Oregon from seismic investigations, *Tectonophysics*, *329*, 79–97, doi:10.1016/S0040-1951(00)00190-6.
Gerlings, J., K. E. Louden, and H. R. Jackson (2011), Crustal structure of the Flemish Cap Continental Margin (eastern Canada): An analysis of a seismic refraction profile, *Geophys. J. Int.*, *185*, 30–48, doi:10.1111/j.1365-246X.2011.04931.x.
Gilbert, G. K. (1895), New light on isostasy, *J. Geol.*, *3*(3), 331–334, doi:10.1086/607194.
Girdler, R. W., and P. Styles (1974), Two stage red sea floor spreading, *Nature*, *247*(1), 7–11, doi:10.1038/247007a0.
Giresse, P., C.-T. Hoang, and G. Kouyoumontzakis (1984), Analysis of vertical movements deduced from a geochronological study of marine Pleistocene deposits, southern coast of Angola, *J. Afr. Earth Sci.*, *2*(2), 177–187, doi:10.1016/S0731-7247(84)80012-9.
Goldschmidt-Rokita, A., K. J. F. Hansch, H. B. Hirschleber, T. Iwasaki, T. Kanazawa, H. Shimamura, and M. A. Sellevoll (1994), The ocean/continent transition along a profile through the Lofoten basin, Northern Norway, *Mar. Geophys. Res.*, *16*, 201–224, doi:10.1007/BF01237514.
Golonka, J. (2004), Plate tectonic evolution of the southern margin of Eurasia in the Mesozoic and Cenozoic, *Tectonophysics*, *381*, 235–273, doi:10.1016/j.tecto.2002.06.004.
Greenroyd, C. J., C. Peirce, M. Rodger, A. B. Watts, and R. W. Hobbs (2007), Crustal structure of the French Guiana margin, West Equatorial Atlantic, *Geophys. J. Int.*, *169*, 964–987, doi:10.1111/j.1365-246X.2007.03372.x.
Greenroyd, C. J., C. Peirce, M. Rodger, A. B. Watts, and R. W. Hobbs (2008), Demerara Plateau—The structure and evolution of a transform passive margin, *Geophys. J. Int.*, *172*, 549–564, doi:10.1111/j.1365-246X.2007.03662.x.
Grevemeyer, I., E. R. Flueh, C. Reichert, J. Bialas, D. Kläschen, and C. Kopp (2001), Crustal architecture and deep structure of the Ninetyeast Ridge hotspot trail from active-source ocean bottom seismology, *Geophys. J. Int.*, *144*, 414–431, doi:10.1046/j.0956-540X.2000.01334.x.
Grevemeyer, I., C. R. Ranero, E. R. Flueh, D. Kläschen, and J. Bialas (2007), Passive and active seismological study of bending-related faulting and mantle serpentinization at the Middle America trench, *Earth Planet. Sci. Lett.*, *258*, 528–542, doi:10.1016/j.epsl.2007.04.013.
Griggs, D. T. (1939), A theory of mountain-building, *Am. J. Sci.*, *237*(9), 611–650, doi:10.2475/ajs.237.9.611.
Grose, C. J., and J. C. Afonso (2013), Comprehensive plate models for the thermal evolution of oceanic lithosphere, *Geochem. Geophys. Geosyst.*, *14*, 3751–3778, doi:10.1002/ggge.20232.
Guiraud, M., A. Buta-Neto, and D. Quesne (2010), Segmentation and differential post-rift uplift at the Angola margin as recorded by the transform-rifted Benguela and oblique-to-orthogonal-rifted Kwanza basins, *Mar. Pet. Geol.*, *27*(5), 1040–1068, doi:10.1016/j.marpetgeo.2010.01.017.
Gutscher, M. A., J. Malod, J. P. Rehault, I. Contrucci, F. Klingelhöfer, L. Mendes-Victor, and W. Spakman (2002), Evidence for active subduction beneath Gibraltar, *Geology*, *30*(12), 1071–1074, doi:10.1130/0091-7613(2002)030<1071:EFASBG>2.0.CO;2.
Hampel, A., N. Kukowski, J. Bialas, C. Huebscher, and R. Heinbockel (2004), Ridge subduction at an erosive margin: The collision zone of the Nazca Ridge in southern Peru, *J. Geophys. Res.*, *109*, B02101, doi:10.1029/2003JB002593.
Hartley, R. A., G. G. Roberts, N. White, and C. Richardson (2011), Transient convective uplift of an ancient buried landscape, *Nat. Geosci.*, *4*, 562–565, doi:10.1038/ngeo1191.
Hawkins, L., J. Hennion, J. Nafe, and H. Doyle (1965), Marine seismic refraction studies on the continental margin to the south of Australia, *Deep Sea Res.*, *12*, 479–495.
Hayes, D. E. (1988), Age-depth relationships and depth anomalies in the southeast Indian Ocean and South Atlantic Ocean, *J. Geophys. Res.*, *93*(B4), 2937–2954.
Heestand, R. L., and S. T. Crough (1981), The effect of hot spots on the oceanic age-depth relation, *J. Geophys. Res.*, *86*(B7), 6107–6114, doi:10.1029/JB086iB07p06107.
Hein, C. J., D. M. FitzGerald, J. T. de Menezes, W. J. Cleary, A. H. F. Klein, and M. B. Albernaz (2014), Coastal response to late-stage transgression and sea-level highstand, *Bull. Geol. Soc. Am.*, *126*(3-4), 459–480, doi:10.1130/B30836.1.
Henstock, T. J., R. S. White, and J. H. McBride (1996), Along-axis variability in crustal accretion at the Mid-Atlantic Ridge: Results from the OCEAN study, *J. Geophys. Res.*, *101*(B6), 13,673–13,688.
Herzberg, C., P. D. Asimow, N. Arndt, Y. Niu, C. M. Lesher, J. G. Fitton, M. J. Cheadle, and A. D. Saunders (2007), Temperatures in ambient mantle and plumes: Constraints from basalts, picrites, and komatiites, *Geochem. Geophys. Geosyst.*, *8*, Q02006, doi:10.1029/2006GC001390.
Herzberg, C. T., and P. D. Asimow (2015), PRIMELT3 MEGA.XLSM software for primarymagma calculation: Peridotite primarymagma MgO contents fromthe liquidus to the solidus, *Geochem. Geophys. Geosyst.*, *16*, 563–578, doi:10.1002/2014GC005631.
Hill, P., and A. Moore (2001), Geological framework of the South Tasman Rise and East Tasman Plateau, Record 2001/40, *Tech. Rep.*, Geoscience, Australia.
Hillier, J. K., and A. B. Watts (2005), Relationship between depth and age in the North Pacific Ocean, *J. Geophys. Res.*, *110*, B02405, doi:10.1029/2004JB003406.
Hippolyte, J.-C., C. Muller, N. Kaymakci, and E. Sangu (2010), *Dating of the Black Sea Basin: New nannoplankton ages from its inverted margin in the Central Pontides (Turkey)*, vol. 340, pp. 113–136, Geol. Soc. Spec. Publ., London, doi:10.1144/SP340.7.
Hirata, N., B. Y. Karp, T. Yamaguchi, T. Kanazawa, K. Suyehiro, J. Kasahara, H. Shiobara, M. Shinohara, and H. Kinoshita (1992), Oceanic crust in the Japan Basin of the Japan Sea by the 1990 Japan-USSR Expedition, *Geophys. Res. Lett.*, *19*, 2027–2030, doi:10.1029/92GL02094.
Hirsch, K. K., K. Bauer, and M. Scheck-Wenderoth (2009), Deep structure of the western South African passive margin—Results of a combined approach of seismic, gravity and isostatic investigations, *Tectonophysics*, *470*, 57–70, doi:10.1016/j.tecto.2008.04.028.
Hoggard, M. J., N. J. White, and D. Al-Attar (2016), Global dynamic topography observations reveal limited influence of large-scale mantle flow, *Nat. Geosci.*, *9*(6), 456–463, doi:10.1038/ngeo2709.
Hohertz, W. L., and R. L. Carlson (1998), An independent test of thermal subsidence and asthenosphere flow beneath the Argentine Basin, *Earth Planet. Sci. Lett.*, *161*, 73–83.
Holbrook, W., D. Lizarralde, S. McGeary, N. Bangs, and J. Diebold (1999), Structure and composition of the Aleutian island arc and implications for continental crustal growth, *Geology*, *27*(1), 31–34, doi:10.1130/0091-7613(1999)027<0031:SACOTA>2.3.CO;2.
Holbrook, W., H. Larsen, J. Korenaga, T. Dahl-Jensen, I. Reid, P. Kelemen, J. Hopper, G. Kent, D. Lizarralde, S. Bernstein, and R. Detrick (2001), Mantle thermal structure and active upwelling during continental breakup in the North Atlantic, *Earth Planet. Sci. Lett.*, *190*, 251–266, doi:10.1016/S0012-821X(01)00392-2.
Holbrook, W. S., E. C. Reiter, G. M. Purdy, D. Sawyer, P. L. Stoffa, J. A. Austin, and J. Makris (1994), Deep structure of the U.S. Atlantic continental margin, offshore South Carolina, from coincident ocean bottom and multichannel seismic data, *J. Geophys. Res.*, *99*(B5), 9155–9178.
Holbrook, W. S., T. M. Brocher, U. S. ten Brink, and J. A. Hole (1996), Crustal structure of a transform plate boundary: San Francisco Bay and the central California continental margin, *J. Geophys. Res.*, *101*(B10), 22,311–22,334, doi:10.1029/96JB01642.

Holmes, R. C., M. Tolstoy, J. R. Cochran, and J. S. Floyd (2008), Crustal thickness variations along the Southeast Indian Ridge (100°–116°E) from 2-D body wave tomography, *Geochem. Geophys. Geosyst.*, *9*, Q12020, doi:10.1029/2008GC002152.

Holmes, R. C., M. Tolstoy, A. J. Harding, J. A. Orcutt, and J. P. Morgan (2010), Australian Antarctic Discordance as a simple mantle boundary, *Geophys. Res. Lett.*, *37*, L09309, doi:10.1029/2010GL042621.

Hooft, E. E. E., R. S. Detrick, D. R. Toomey, J. A. Collins, and J. Lin (2000), Crustal thickness and structure along three contrasting spreading segments of the Mid-Atlantic Ridge, 33.5°–35°N, *J. Geophys. Res.*, *105*(B4), 8205–8226, doi:10.1029/1999JB900442.

Hooft, E. E. E., B. Brandsdóttir, R. Mjelde, H. Shimamura, and Y. Murai (2006), Asymmetric plume-ridge interaction around Iceland: The Kolbeinsey Ridge Iceland Seismic Experiment, *Geochem. Geophys. Geosyst.*, *7*, Q05015, doi:10.1029/2005GC001123.

Hopper, J. R., T. Dahl-Jensen, W. S. Holbrook, H. C. Larsen, D. Lizarralde, J. Korenaga, G. M. Kent, and P. Kelemen (2003), Structure of the SE Greenland margin from seismic reflection and refraction data: Implications for nascent spreading center subsidence and asymmetric crustal accretion during North Atlantic opening, *J. Geophys. Res.*, *108*(B5), 2269, doi:10.1029/2002JB001996.

Houtz, R., C. Windisch, and S. Murauchi (1980), Changes in the crust and upper mantle near the Japan-Bonin trench, *J. Geophys. Res.*, *85*(B1), 267–274, doi:10.1029/JB085iB01p00267.

Houtz, R. E., W. J. Ludwig, J. D. Milliman, and J. A. Grow (1977), Structure of the northern Brazilian continental margin, *Geol. Soc. Am. Bull.*, *88*, 711–719, doi:10.1130/0016-7606(1977)88<711.

Ito, G., and P. E. van Keken (2007), *Hotspots and Melting Anomalies*, vol. 7, pp. 371–435, Treatise on Geophys.

Ivandic, M., I. Grevemeyer, A. Berhorst, E. R. Flueh, and K. McIntosh (2008), Impact of bending related faulting on the seismic properties of the incoming oceanic plate offshore of Nicaragua, *J. Geophys. Res.*, *113*, B05410, doi:10.1029/2007JB005291.

Iwasaki, T., H. Shiobara, A. Nishizawa, T. Kanazawa, K. Suyehiro, N. Hirata, T. Urabe, and H. Shimamura (1989), A detailed subduction structure in the Kuril trench deduced from ocean bottom seismographic refraction studies, *Tectonophysics*, *165*, 315–336, doi:10.1016/0040-1951(89)90056-5.

Izzeldin, A. (1987), Seismic, gravity and magnetic surveys in the central part of the Red Sea: Their interpretation and implications for the structure and evolution of the Red Sea, *Tectonophysics*, *143*, 269–306, doi:10.1016/0040-1951(87)90214-9.

Jackson, H., J. Faleide, and O. Eldholm (1990), Crustal structure of the sheared southwestern Barents Sea continental margin, *Mar. Geol.*, *93*, 119–146, doi:10.1016/0025-3227(90)90080-4.

Jackson, M. P. A., M. R. Hudec, and K. A. Hegarty (2005), The great West African Tertiary coastal uplift: Fact or fiction? A perspective from the Angolan divergent margin, *Tectonics*, *24*, TC6014, doi:10.1029/2005TC001836.

Jacoby, W. R., W. Weigel, and T. Fedorova (2007), Crustal structure of the Reykjanes Ridge near 62°N, on the basis of seismic refraction and gravity data, *J. Geodyn.*, *43*, 55–72, doi:10.1016/j.jog.2006.10.002.

Jaffal, M., F. Klingelhöfer, L. Matias, F. Teixeira, and M. Amrhar (2009), Crustal structure of the NW Moroccan margin from deep seismic data (SISMAR Cruise), *C. R. Geosci.*, *341*, 495–503, doi:10.1016/j.crte.2009.04.003.

Johnson, H. P., and R. L. Carlson (1992), Variation of sea floor depth with age: A test of models based on drilling results, *Geophys. Res. Lett.*, *19*(19), 1971–1974, doi:10.1029/92GL01946.

Jokat, W., and M. C. Schmidt-Aursch (2007), Geophysical characteristics of the ultraslow spreading Gakkel Ridge, Arctic Ocean, *Geophys. J. Int.*, *168*, 983–998, doi:10.1111/j.1365-246X.2006.03278.x.

Jokat, W., O. Ritzmann, C. Reichert, and K. Hinz (2004), Deep crustal structure of the continental margin off the Explora Escarpment and in the Lazarev Sea, East Antarctica, *Mar. Geophys. Res.*, *25*, 283–304, doi:10.1007/s11001-005-1337-9.

Jones, S. M., N. J. White, and J. Maclennan (2002), V-shaped ridges around Iceland: Implications for spatial and temporal patterns of mantle convection, *Geochem. Geophys. Geosyst.*, *3*(10), 1059, doi:10.1029/2002GC000361.

Jordan, T. H. (1975), The continental tectosphere, *Rev. Geophys.*, *13*(3), 1–12.

Kaban, M. K., P. Schwintzer, I. M. Artemieva, and W. D. Mooney (2003), Density of the continental roots: Compositional and thermal contributions, *Earth Planet. Sci. Lett.*, *209*, 53–69, doi:10.1016/S0012-821X(03)00072-4.

Kaneda, K., S. Kodaira, A. Nishizawa, T. Morishita, and N. Takahashi (2010), Structural evolution of preexisting oceanic crust through intraplate igneous activities in the Marcus-Wake seamount chain, *Geochem. Geophys. Geosyst.*, *11*, doi:10.1029/2010GC003231.

Keen, C., et al. (1986), Deep structure of the US East Coast passive margin from Large Aperture Seismic Experiments (LASE), *Mar. Pet. Geol.*, *3*, 234–242, doi:10.1016/0264-8172(86)90047-4.

Kido, M., and T. Seno (1994), Dynamic topography compared with residual depth anomalies in oceans and implications for age-depth curves, *Geophys. Res. Lett.*, *21*(8), 717–720, doi:10.1029/94GL00305.

King, S. D., and C. Adam (2014), Hotspot swells revisited, *Phys. Earth Planet. Inter.*, *235*, 66–83, doi:10.1016/j.pepi.2014.07.006.

Kipf, A., F. Hauff, R. Werner, K. Gohl, P. van den Bogaard, K. Hoernle, D. Maicher, and A. Klügel (2014), Seamounts off the West Antarctic margin: A case for non-hotspot driven intraplate volcanism, *Gondwana Res.*, *25*, 1660–1679, doi:10.1016/j.gr.2013.06.013.

Klein, E. M., and C. H. Langmuir (1987), Global correlations of ocean ridge basalt chemistry with axial depth and crustal thickness, *J. Geophys. Res.*, *92*(B8), 8089–8115.

Klein, E. M., C. H. Langmuir, and H. Staudigel (1991), Geochemistry of basalts from the Southeast Indian Ridge, 115°E–138°E, *J. Geophys. Res.*, *96*(B2), 2089–2107, doi:10.1029/90JB01384.

Klingelhöfer, F., L. Géli, L. Matias, N. Steinsland, and J. Mohr (2000), Crustal structure of a super-slow spreading centre: A seismic refraction study of Mohns Ridge, 72°N, *Geophys. J. Int.*, *141*, 509–526, doi:10.1046/j.1365-246X.2000.00098.x.

Klingelhöfer, F., T. A. Minshull, D. K. Blackman, P. Harben, and V. Childers (2001), Crustal structure of Ascension Island from wide-angle seismic data: Implications for the formation of near-ridge volcanic islands, *Earth Planet. Sci. Lett.*, *190*, 41–56, doi:10.1016/S0012-821X(01)00362-4.

Klingelhöfer, F., Y. Lafoy, J. Collot, E. Cosquer, L. Géli, H. Nouzé, and R. Vially (2007), Crustal structure of the basin and ridge system west of New Caledonia (southwest Pacific) from wide-angle and reflection seismic data, *J. Geophys. Res.*, *112*, B11102, doi:10.1029/2007JB005093.

Klingelhöfer, F., C. Labails, E. Cosquer, S. Rouzo, L. Géli, D. Aslanian, J.-L. Olivet, M. Sahabi, H. Nouzé, and P. Unternehr (2009a), Crustal structure of the SW-Moroccan margin from wide-angle and reflection seismic data (the DAKHLA experiment). Part A: Wide-angle seismic models, *Tectonophysics*, *468*, 63–82, doi:10.1016/j.tecto.2008.07.022.

Klingelhöfer, F., C.-S. Lee, J.-Y. Lin, and J.-C. Sibuet (2009b), Structure of the southernmost Okinawa Trough from reflection and wide-angle seismic data, *Tectonophysics*, *466*, 281–288, doi:10.1016/j.tecto.2007.11.031.

Klingelhöfer, F., M.-A. Gutscher, S. Ladage, J.-X. Dessa, D. Graindorge, D. Franke, C. André, H. Permana, T. Yudistira, and A. Chauhan (2010), Limits of the seismogenic zone in the epicentral region of the 26 December 2004 great Sumatra-Andaman earthquake: Results from seismic refraction and wide-angle reflection surveys and thermal modeling, *J. Geophys. Res.*, *115*, B01304, doi:10.1029/2009JB006569.

Klingelhöfer, F., T. Berthet, S. Lallemand, P. Schnurle, C.-S. Lee, C.-S. Liu, K. McIntosh, and T. Theunissen (2012), P-wave velocity structure of the southern Ryukyu margin east of Taiwan: Results from the ACTS wide-angle seismic experiment, *Tectonophysics*, *578*, 50–62, doi:10.1016/j.tecto.2011.10.010.

Knesel, K. M., Z. S. Souza, P. M. Vasconcelos, B. E. Cohen, and F. V. Silveira (2011), Young volcanism in the Borborema Province, NE Brazil, shows no evidence for a trace of the Fernando de Noronha plume on the continent, *Earth Planet. Sci. Lett.*, *302*, 38–50, doi:10.1016/j.epsl.2010.11.036.

Knopoff, L. (1964), The convection current hypothesis, *Rev. Geophys.*, *2*(1), 89–122.

Kodaira, S., R. Mjelde, K. Gunnarsson, H. Shiobara, and H. Shimamura (1997), Crustal structure of the Kolbeinsey North Atlantic, obtained by use of ocean bottom seismographs, *J. Geophys. Res.*, *102*(B2), 3131–3151.

Kodaira, S., R. Mjelde, K. Gunnarsson, H. Shiobara, and H. Shimamura (1998a), Structure of the Jan Mayen microcontinent and implications for its evolution, *Geophys. J. Int.*, *132*, 383–400, doi:10.1046/j.1365-246X.1998.00444.x.

Kodaira, S., R. Mjelde, K. Gunnarsson, H. Shiobara, and H. Shimamura (1998b), Evolution of oceanic crust on the Kolbeinsey Ridge, north of Iceland, over the past 22 Myr, *Terra Nova*, *10*(1), 27–31, doi:10.1046/j.1365-3121.1998.00166.x.

Kopp, H., E. R. Flueh, D. Klaeschen, J. Bialas, and C. Reichert (2001), Crustal structure of the central Sunda margin at the onset of oblique subduction, *Geophys. J. Int.*, *147*, 449–474, doi:10.1046/j.0956-540X.2001.01547.x.

Kopp, H., D. Klaeschen, E. R. Flueh, J. Bialas, and C. Reichert (2002), Crustal structure of the Java margin from seismic wide-angle and multichannel reflection data, *J. Geophys. Res.*, *107*(B2), 2034, doi:10.1029/2000JB000095.

Kopp, H., C. Kopp, J. P. Morgan, E. R. Flueh, and W. Weinrebe (2003), Fossil hot spot-ridge interaction in the Musicians Seamount Province: Geophysical investigations of hot spot volcanism at volcanic elongated ridges, *J. Geophys. Res.*, *108*(B3), 2160, doi:10.1029/2002JB002015.

Kopp, H., E. R. Flueh, C. Papenberg, and D. Klaeschen (2004), Seismic investigations of the O'Higgins Seamount Group and Juan Fernandez Ridge: Aseismic ridge emplacement and lithosphere hydration, *Tectonics*, *23*, TC2009, doi:10.1029/2003TC001590.

Korenaga, J., W. S. Holbrook, G. M. Kent, P. B. Kelemen, R. S. Detrick, H.-C. Larsen, J. R. Hopper, and T. Dahl-Jensen (2000), Crustal structure of the southeast Greenland margin from joint refraction and reflection seismic tomography, *J. Geophys. Res.*, *105*(B9), 21,591–21,614, doi:10.1029/2000JB900188.

Korenaga, T., and J. Korenaga (2008), Subsidence of normal oceanic lithosphere, apparent thermal expansivity, and seafloor flattening, *Earth Planet. Sci. Lett.*, *268*, 41–51, doi:10.1016/j.epsl.2007.12.022.

Krabbenhöft, A., J. Bialas, H. Kopp, N. Kukowski, and C. Hübscher (2004), Crustal structure of the Peruvian continental margin from wide-angle seismic studies, *Geophys. J. Int.*, *159*, 749–764, doi:10.1111/j.1365-246X.2004.02425.x.

Ku, H. H. (1966), Notes on the use of propagation of error formulas, *J. Res. Natl. Bureau Standards C*, *70C*(4), 263–273, doi:10.6028/jres.070C.025.

Lafoy, Y., I. Brodien, R. Vially, and N. F. Exon (2005), Structure of the basin and ridge system west of New Caledonia (Southwest Pacific): A synthesis, *Mar. Geophys. Res.*, *26*, 37–50, doi:10.1007/s11001-005-5184-5.

Lanyon, R., R. Varne, and A. J. Crawford (1993), Tasmanian Tertiary basalts, the Balleny plume, and opening of the Tasman Sea (southwest Pacific Ocean), *Geology*, *21*(6), 555–558, doi:10.1130/0091-7613(1993)021<0555:TTBTBP>2.3.CO;2.

Larson, S. C. (1931), The shrinkage of the coefficient of multiple correlation, *J. Educat. Psychol.*, *22*(1), 45–55.

Larter, R. D., and P. F. Barker (1989), Seismic stratigraphy of the Antarctic Peninsula Pacific margin: A record of Pliocene-Pleistocene ice volume and paleoclimate, *Geology*, *17*(8), 731–734, doi:10.1130/0091-7613(1989)017<0731:SSOTAP>2.3.CO;2.

Larter, R. D., L. E. Vanneste, P. Morris, and D. K. Smythe (2003), Structure and tectonic evolution of the South Sandwich arc, *Geol. Soc. London Spec. Publ.*, *219*, 255–284, doi:10.1144/GSL.SP.2003.219.01.13.

Laske, G., and G. Masters (1997), A global digital map of sediment thickness, *EOS Trans. AGU*, *78*(46), Fall Meet. Suppl. F48397.

Laske, G., G. Masters, Z. Ma, and M. Pasyanos (2013), Update on CRUST1.0—A 1-degree global model of Earth's crust, *Abstract EGU2013-2658 presented at 2013 EGU General Assembly*, Vienna, Austria.

Lau, K. W. H., K. E. Louden, T. Funck, B. E. Tucholke, W. S. Holbrook, J. R. Hopper, and H. C. Larsen (2006a), Crustal structure across the Grand Banks-Newfoundland Basin Continental Margin—I. Results from a seismic refraction profile, *Geophys. J. Int.*, *167*, 127–156, doi:10.1111/j.1365-246X.2006.02988.x.

Lau, K. W. H., K. E. Louden, S. Deemer, J. Hall, J. R. Hopper, B. E. Tucholke, W. S. Holbrook, and H. C. Larsen (2006b), Crustal structure across the Grand Banks-Newfoundland Basin Continental Margin—II. Results from a seismic reflection profile, *Geophys. J. Int.*, *167*, 157–170, doi:10.1111/j.1365-246X.2006.02989.x.

Laughton, A., and C. Tramontini (1969), Recent studies of the crustal structure in the Gulf of Aden, *Tectonophysics*, *8*, 359–375, doi:10.1016/0040-1951(69)90043-2.

Lavier, L. L., M. S. Steckler, and F. Brigaud (2001), Climatic and tectonic control on the Cenozoic evolution of the West African margin, *Mar. Geol.*, *178*, 63–80, doi:10.1016/S0025-3227(01)00175-X.

Le Douaran, S., and B. E. Parsons (1982), A note on the correction of ocean floor depths for sediment loading, *J. Geophys. Res.*, *87*(B6), 4715–4722, doi:10.1029/JB087iB06p04715.

Le Pichon, X., R. E. Houtz, C. L. Drake, and J. E. Nafe (1965), Crustal structure of the mid-ocean ridges, *J. Geophys. Res.*, *70*(2), 319–339.

Le Stunff, Y., and Y. Ricard (1995), Topography and geoid due to lithospheric mass anomalies, *Geophys. J. Int.*, *122*(3), 982–990, doi:10.1111/j.1365-246X.1995.tb06850.x.

Lecroart, P., A. Cazenave, Y. Ricard, C. Thoraval, and D. G. Pyle (1997), Along-axis dynamic topography constrained by major-element chemistry, *Earth Planet. Sci. Lett.*, *149*, 49–56, doi:10.1016/s0012-821x(97)00062-9.

Leger, G. T., and K. E. Louden (1990), Seismic refraction measurements in the Central Indian Basin: Evidence for crustal thickening related to intraplate deformation, in *Proceedings of the Ocean Drilling Program, Scientific Results*, vol. 116, pp. 291–309, ODP Ocean Drilling Program, College Station, Tex.

Leinweber, V. T., F. Klingelhöfer, S. Neben, C. Reichert, D. Aslanian, L. Matias, I. Heyde, B. Schreckenberger, and W. Jokat (2013), The crustal structure of the Central Mozambique continental margin—Wide-angle seismic, gravity and magnetic study in the Mozambique Channel, Eastern Africa, *Tectonophysics*, *599*, 170–196, doi:10.1016/j.tecto.2013.04.015.

Leitchenkov, G., J. Guseva, V. Gandyukhin, G. Grikurov, Y. Kristoffersen, M. Sand, A. Golynsky, and N. Aleshkova (2008), Crustal structure and tectonic provinces of the Riiser-Larsen Sea area (East Antarctica): Results of geophysical studies, *Mar. Geophys. Res.*, *29*, 135–158, doi:10.1007/s11001-008-9051-z.

Leitner, B., A. M. Trehu, and N. J. Godfrey (1998), Crustal structure of the northwestern Vizcaino block and Gorda Escarpment, offshore northern California, and implications for postsubduction deformation of a paleoaccretionary margin, *J. Geophys. Res.*, *103*(B10), 23,795–23,812, doi:10.1029/98JB02050.

Leprêtre, A., F. Klingelhöfer, D. Graindorge, P. Schnurle, M. O. Beslier, K. Yelles, J. Déverchère, and R. Bracene (2013), Multiphased tectonic evolution of the Central Algerian margin from combined wide-angle and reflection seismic data off Tipaza, Algeria, *J. Geophys. Res. Solid Earth*, *118*, 3899–3916, doi:10.1002/jgrb.50318.

Leroy, S., et al. (2010), Contrasted styles of rifting in the eastern Gulf of Aden: A combined wide-angle, multichannel seismic, and heat flow survey, *Geochem. Geophys. Geosyst.*, *11*, Q07004, doi:10.1029/2009GC002963.

Ligi, M., E. Bonatti, G. Bortoluzzi, A. Cipriani, L. Cocchi, F. Caratori Tontini, E. Carminati, L. Ottolini, and A. Schettino (2012), Birth of an ocean in the Red Sea: Initial pangs, *Geochem. Geophys. Geosyst.*, *13*, Q08009, doi:10.1029/2012GC004155.

Limond, W., F. Gray, G. Grau, J. Fail, L. Montadert, and P. Patriat (1974), A seismic study in the Bay of Biscay, *Earth Planet. Sci. Lett.*, *23*, 357–368, doi:10.1016/0012-821X(74)90125-3.

Lithgow-Bertelloni, C., and P. G. Silver (1998), Dynamic topography, plate driving forces and the African superswell, *Nature*, *395*(9), 269–272, doi:10.1038/26212.

Lizarralde, D., and W. S. Holbrook (1997), U.S. mid-Atlantic margin structure and early thermal evolution, *J. Geophys. Res.*, *102*(B10), 22,855–22,875, doi:10.1029/96JB03805.

Lizarralde, D., W. S. Holbrook, S. McGeary, N. Bangs, and J. B. Diebold (2002), Crustal construction of a volcanic arc, wide-angle seismic results from the western Alaska Peninsula, *J. Geophys. Res.*, *107*(B8), 2164, doi:10.1029/2001JB000230.

Lizarralde, D., et al. (2007), Variation in styles of rifting in the Gulf of California, *Nature*, *448*, 466–469, doi:10.1038/nature06035.

Louden, K. E. (1995), Variations in crustal structure related to intraplate deformation: Evidence from seismic refraction and gravity profiles in the Central Indian Basin, *Geophys. J. Int.*, *120*, 375–392, doi:10.1111/j.1365-246X.1995.tb01826.x.

Louden, K. E., B. E. Tucholke, and G. N. Oakey (2004), Regional anomalies of sediment thickness, basement depth and isostatic crustal thickness in the North Atlantic Ocean, *Earth Planet. Sci. Lett.*, *224*, 193–211, doi:10.1016/j.epsl.2004.05.002.

Lucazeau, F., et al. (2008), Persistent thermal activity at the Eastern Gulf of Aden after continental break-up, *Nat. Geosci.*, *1*, 854–858, doi:10.1038/ngeo359.

Ludwig, W. J., and P. D. Rabinowitz (1980), Geophysical characteristics of ocean crust: IPOD candidate site PAC 5, central eastern Pacific Ocean Basin, *Mar. Geol.*, *35*, 111–127.

Ludwig, W. J., J. E. Nafe, E. S. W. Simpson, and S. Sacks (1968), Seismic-refraction measurements on the Southeast African Continental Margin, *J. Geophys. Res.*, *73*(12), 3707–3719, doi:10.1029/JB073i012p03707.

Ludwig, W. J., S. Murauchi, M. Ewing, H. Hotta, R. E. Houtz, T. Yoshii, T. Asanuma, K. Hagiwara, T. Sato, and S. Ando (1971), Structure of Bowers Ridge, Bering Sea, *J. Geophys. Res.*, *76*(26), 6350–6366.

Ludwig, W. J., S. Murauchi, N. Den, P. Buhl, H. Hotta, M. Ewing, T. Asanuma, T. Yoshii, and N. Sakajiri (1973), Structure of East China Sea-West Philippine Sea Margin off southern Kyushu, Japan, *J. Geophys. Res.*, *78*(14), 2526–2536, doi:10.1029/JB078i014p02526.

Makris, J., J. Papoulia, S. McPherson, and L. Warner (2012), Mapping of sediments and crust offshore Kenya, east Africa: A wide aperture refraction/reflection survey, in *SEG Annual Meeting*.,10.1190/segam2012-0426.1

Maksymowicz, A., E. Contreras-Reyes, I. Grevemeyer, and E. R. Flueh (2012), Structure and geodynamics of the post-collision zone between the Nazca-Antarctic spreading center and South America, *Earth Planet. Sci. Lett.*, *345-348*, 27–37, doi:10.1016/j.epsl.2012.06.023.

Marks, K. M., and D. T. Sandwell (1991), Analysis of geoid height versus topography for oceanic plateaus and swells using nonbiased linear regression, *J. Geophys. Res.*, *96*(B5), 8,045–8,055, doi:10.1029/91JB00240.

Marks, K. M., D. T. Sandwell, P. R. Vogt, and S. A. Hall (1991), Mantle downwelling beneath the Australian-Antarctic discordance zone: Evidence from geoid height versus topography, *Earth Planet. Sci. Lett.*, *103*, 325–338, doi:10.1016/0012-821X(91)90170-M.

Martínez, F., B. Taylor, and A. M. Goodliffe (1999), Contrasting styles of seafloor spreading in the Woodlark Basin: Indications of rift-induced secondary mantle convection, *J. Geophys. Res.*, *104*(B6), 12,909–12,926, doi:10.1029/1999JB900068.

Martinez-Loriente, S., V. Sallares, E. Gracia, R. Bartolome, J. J. Danobeitia, and N. Zitellini (2014), Seismic and gravity constraints on the nature of the basement in the Africa-Eurasia plate boundary: New insights for the geodynamic evolution of the SW Iberian margin, *J. Geophys. Res. Solid Earth*, *119*, 127–149, doi:10.1002/2013JB010264.

Matthews, S., O. Shorttle, and J. Maclennan (2016), The temperature of the Icelandic mantle from olivine-spinel aluminum exchange thermometry, *Geochem. Geophys. Geosyst.*, *17*, 4725–4752, doi:10.1002/2016GC006497.

Mayer-Guerr, T. (2015), The combined satellite gravity field model GOCO05s, *EGU General Assembly 2015*, held 12–17 April, 2015 in Vienna, Austria. id.12364.

McBride, J. H., R. S. White, T. J. Henstock, and R. W. Hobbs (1994), Complex structure along a Mesozoic sea-floor spreading ridge: BIRPS deep seismic reflection, Cape Verde abyssal plain, *Geophys. J. Int.*, *119*, 453–478.

McKenzie, D. P. (1967), Some remarks on heat flow and gravity anomalies, *J. Geophys. Res.*, *72*(24), 6261–6273, doi:10.1029/JZ072i024p06261.

McKenzie, D. P., and M. J. Bickle (1988), The volume and composition of melt generated by extension of the lithosphere, *J. Petrol.*, *29*(3), 625–679, doi:10.1093/petrology/29.3.625.

McKenzie, D. P., and D. Fairhead (1997), Estimates of the effective elastic thickness of the continental lithosphere from Bouguer and free air gravity anomalies, *J. Geophys. Res.*, *102*(B12), 27,523–27,552, doi:10.1029/97JB02481.

McKenzie, D. P., J. Roberts, and N. Weiss (1973), Numerical models of convection in the Earth's mantle, *Tectonophysics*, *19*, 89–103, doi:10.1016/0040-1951(73)90034-6.

McNutt, M. K., and K. M. Fischer (1987), The South Pacific superswell, in *Seamounts, Islands, and Atolls*, vol. 43, pp. 25–33, AGU, Washington, D. C.,10.1029/GM043p0025.

Menard, H. W. (1965), Sea floor relief and mantle convection, *Phys. Chem. Earth*, *6*, 315–364, doi:10.1016/0079-1946(65)90017-0.

Menard, H. W. (1969), Elevation and subsidence of oceanic crust, *Earth Planet. Sci. Lett.*, *6*, 275–284.

Menard, H. W. (1973), Depth anomalies and the bobbing motion of drifting islands, *J. Geophys. Res.*, *78*(23), 5128–5137, doi:10.1029/JB078i023p05128.

Mihoubi, A., P. Schnurle, Z. Benaissa, M. Badsi, R. Bracene, H. Djelit, L. Geli, F. Sage, A. Agoudjil, and F. Klingelhöfer (2014), Seismic imaging of the eastern Algerian margin off Jijel: Integrating wide-angle seismic modelling and multichannel seismic pre-stack depth migration, *Geophys. J. Int.*, *198*, 1486–1503, doi:10.1093/gji/ggu179.

Miller, K. G., M. A. Kominz, J. V. Browning, J. D. Wright, G. S. Mountain, M. E. Katz, P. J. Sugarman, B. S. Cramer, N. Christie-Blick, and S. F. Pekar (2005), The phanerozoic record of global sea-level change, *Science*, *310*, 1293–1298, doi:10.1126/science.1116412.

Millett, J. M., M. J. Hole, D. W. Jolley, N. Schofield, and E. Campbell (2016), Frontier exploration and the North Atlantic Igneous Province: New insights from a 2.6 km offshore volcanic sequence in the NE Faroe-Shetland Basin, *J. Geol. Soc.*, *173*(2), 320–336, doi:10.1144/jgs2015-069.

Minshull, T. A., and R. S. White (1996), Thin crust on the flanks of the slow-spreading Southwest Indian Ridge, *Geophys. J. Int.*, *125*, 139–148, doi:10.1111/j.1365-246X.1996.tb06541.x.

Minshull, T. A., N. J. Bruguier, and J. M. Brozena (1998), Ridge-plume interactions or mantle heterogeneity near Ascension Island?, *Geology*, *26*(2), 115–118, doi:10.1130/0091-7613(1998)026<0115:RPIOMH>2.3.CO;2.
Minshull, T. A., N. J. Bruguier, and J. M. Brozena (2003), Seismic structure of the Mid-Atlantic Ridge, 8–9°S, *J. Geophys. Res.*, *108*(B11), 2513, doi:10.1029/2002JB002360.
Minshull, T. A., M. R. Muller, and R. S. White (2006), Crustal structure of the Southwest Indian Ridge at 66°E: Seismic constraints, *Geophys. J. Int.*, *166*, 135–147, doi:10.1111/j.1365-246X.2006.03001.x.
Minshull, T. A., C. I. Lane, J. S. Collier, and R. B. Whitmarsh (2008), The relationship between rifting and magmatism in the northeastern Arabian Sea, *Nat. Geosci.*, *1*, 463–467, doi:10.1038/ngeo228.
Mithal, R., and J. C. Mutter (1989), A low-velocity zone within the layer 3 region of 118 Myr old oceanic crust in the estern North Atlantic, *Geophys. J.*, *97*, 275–294, doi:10.1111/j.1365-246X.1989.tb00501.x.
Mjelde, R., P. Digranes, M. Van Schaack, H. Shimamura, H. Shiobara, S. Kodaira, O. Naess, N. Sorenes, and E. Vagnes (2001), Crustal structure of the outer Vøring Plateau, offshore Norway, from ocean bottom seismic and gravity data, *J. Geophys. Res.*, *106*(B4), 6769–6791, doi:10.1029/2000JB900415.
Mjelde, R., T. Raum, B. Myhren, H. Shimamura, Y. Murai, T. Takanami, R. Karpuz, and U. Naess (2005), Continent-ocean transition on the Vøring Plateau, NE Atlantic, derived from densely sampled ocean bottom seismometer data, *J. Geophys. Res.*, *110*, B05101, doi:10.1029/2004JB003026.
Morris, E., R. S. Detrick, T. A. Minshull, J. C. Mutter, R. S. White, W. Su, and P. Buhl (1993), Seismic structure of oceanic crust in the western North Atlantic, *J. Geophys. Res.*, *98*(B8), 13,879–13,903.
Moscoso, E., I. Grevemeyer, E. Contreras-Reyes, E. R. Flueh, Y. Dzierma, W. Rabbel, and M. Thorwart (2011), Revealing the deep structure and rupture plane of the 2010 Maule, Chile earthquake ($M_w = 8.8$) using wide angle seismic data, *Earth Planet. Sci. Lett.*, *307*, 147–155, doi:10.1016/j.epsl.2011.04.025.
Mosteller, F., and J. W. Tukey (1977), Data analysis and regression: A second course in statistics, in *Addison-Wesley Series in Behavioural Science: Quantitative Methods*, Addison-Wesley, Reading, Mass.
Moucha, R., A. M. Forte, J. X. Mitrovica, D. B. Rowley, S. Quéré, N. A. Simmons, and S. P. Grand (2008), Dynamic topography and long-term sea-level variations: There is no such thing as a stable continental platform, *Earth Planet. Sci. Lett.*, *271*, 101–108, doi:10.1016/j.epsl.2008.03.056.
Moulin, M., D. Aslanian, J.-L. Olivet, I. Contrucci, L. Matias, L. Géli, F. Klingelhöfer, H. Nouzé, J.-P. Réhault, and P. Unternehr (2005), Geological constraints on the evolution of the Angolan margin based on reflection and refraction seismic data (ZaïAngo project), *Geophys. J. Int.*, *162*, 793–810, doi:10.1111/j.1365-246X.2005.02668.x.
Mouthereau, F., A. B. Watts, and E. Burov (2013), Structure of orogenic belts controlled by lithosphere age, *Nat. Geosci.*, *6*(9), 785–789, doi:10.1038/ngeo1902.
Muller, M., C. Robinson, T. Minshull, R. White, and M. Bickle (1997), Thin crust beneath ocean drilling program borehole 735B at the Southwest Indian Ridge?, *Earth Planet. Sci. Lett.*, *148*, 93–107, doi:10.1016/S0012-821X(97)00030-7.
Muller, M. R., T. A. Minshull, and R. S. White (2000), Crustal structure of the Southwest Indian Ridge at the Atlantis II Fracture Zone, *J. Geophys. Res.*, *105*(B11), 25,809–25,828.
Müller, R. D., M. Sdrolias, C. Gaina, and W. R. Roest (2008a), Age, spreading rates, and spreading asymmetry of the world's ocean crust, *Geochem. Geophys. Geosyst.*, *9*, Q04006, doi:10.1029/2007GC001743.
Müller, R. D., M. Sdrolias, C. Gaina, B. Steinberger, and C. Heine (2008b), Long-term sea-level fluctuations driven by ocean basin dynamics, *Science*, *319*, 1357–1362, doi:10.1126/science.1151540.
Murauchi, S., et al. (1968), Crustal structure of the Philippine Sea, *J. Geophys. Res.*, *73*(10), 3143–3171, doi:10.1029/JB073i010p03143.
Murauchi, S., W. J. Ludwig, N. Den, H. Hotta, T. Asanuma, T. Yoshii, A. Kubotera, and K. Hagiwara (1973), Structure of the Sulu Sea and the Celebes Sea, *J. Geophys. Res.*, *78*(17), 3437–3447, doi:10.1029/JB078i017p03437.
Nakamura, Y., D. Sawyer, and F. Shaub (1988), Deep crustal structure of the Northwestern Gulf of Mexico, *Gulf Coast Assoc. Geol. Soc. Trans.*, *38*, 207–215.
Nakiboglu, S. M. (1982), Hydrostatic theory of the Earth and its mechanical implications, *Phys. Earth Planet. Inter.*, *28*, 302–311, doi:10.1016/0031-9201(82)90087-5.
Navin, D. A., C. Peirce, and M. C. Sinha (1998), The RAMESSES experiment—II. Evidence for accumulated melt beneath a slow spreading ridge from wide-angle refraction and multichannel reflection seismic profiles, *Geophys. J. Int.*, *135*, 746–772, doi:10.1046/j.1365-246X.1998.00709.x.
Netzeband, G., K. Gohl, C. Hübscher, Z. Ben-Avraham, G. Dehghani, D. Gajewski, and P. Liersch (2006), The Levantine Basin—Crustal structure and origin, *Tectonophysics*, *418*, 167–188, doi:10.1016/j.tecto.2006.01.001.
Nishizawa, A., K. Kaneda, A. Nakanishi, N. Takahashi, and S. Kodaira (2006), Crustal structure of the ocean-island arc transition at the mid Izu-Ogasawara (Bonin) arc margin, *Earth Planets Space*, *58*, e33–e36.
Nishizawa, A., K. Kaneda, Y. Katagiri, and M. Oikawa (2014), Wide-angle refraction experiments in the Daito Ridges region at the northwestern end of the Philippine Sea plate, *Earth Planets Space*, *66*, 25, doi:10.1186/1880-5981-66-25.
Niu, X., A. Ruan, J. Li, T. A. Minshull, D. Sauter, Z. Wu, X. Qiu, M. Zhao, Y. J. Chen, and S. Singh (2015), Along-axis variation in crustal thickness at the ultraslow spreading Southwest Indian Ridge (50°E) from a wide-angle seismic experiment, *Geochem. Geophys. Geosyst.*, *16*, 468–485, doi:10.1002/2014GC005645.
Nyblade, A. A., and S. W. Robinson (1994), The African superswell, *Geophys. Res. Lett.*, *21*(9), 765–768, doi:10.1029/94GL00631.
Oikawa, M., K. Kaneda, and A. Nishizawa (2010), Seismic structures of the 154–160 Ma oceanic crust and uppermost mantle in the Northwest Pacific Basin, *Earth Planets Space*, *62*, e13–e16, doi:10.5047/eps.2010.02.011.
Okay, A. I., A. M. C. Sengor, and N. Gorur (1994), Kinematic history of the opening of the Black Sea and its effect on the surrounding regions, *Geology*, *22*, 267–270.
Olafsson, I., E. Sundvor, O. Eldholm, and K. Grue (1992), More Margin: Crustal structure from analysis of expanded spread profiles, *Mar. Geophys. Res.*, *14*, 137–162, doi:10.1007/BF01204284.
Panasyuk, S. V., and B. H. Hager (2000), Inversion for mantle viscosity profiles constrained by dynamic topography and the geoid, and their estimated errors, *Geophys. J. Int.*, *143*, 821–836, doi:10.1046/j.0956-540X.2000.01286.x.
Páramo, P., W. S. Holbrook, H. E. Brown, D. Lizarralde, J. Fletcher, P. Umhoefer, G. Kent, A. Harding, A. Gonzalez, and G. Axen (2008), Seismic structure of the southern Gulf of California from Los Cabos block to the East Pacific Rise, *J. Geophys. Res.*, *113*, B03307, doi:10.1029/2007JB005113.
Pari, G. (2001), Crust 5.1-based inference of the Earth's dynamic surface topography: Geodynamic implications, *Geophys. J. Int.*, *144*, 501–516.

Pari, G., and W. R. Peltier (2000), Subcontinental mantle dynamics: A further analysis based on the joint constraints of dynamic surface topography and free-air gravity, *J. Geophys. Res.*, *105*(B3), 5635–5662, doi:10.1029/1999JB900349.
Parnell-Turner, R., N. White, T. Henstock, B. Murton, J. Maclennan, and S. M. Jones (2014), A continuous 55-million-year record of transient mantle plume activity beneath Iceland, *Nat. Geosci.*, *7*, 914–919, doi:10.1038/ngeo2281.
Parsiegla, N., J. Stankiewicz, K. Gohl, T. Ryberg, and G. Uenzelmann-Neben (2009), Southern African continental margin: Dynamic processes of a transform margin, *Geochem. Geophys. Geosyst.*, *10*, Q03007, doi:10.1029/2008GC002196.
Parsons, B., and J. G. Sclater (1977), An analysis of the variation of ocean floor bathymetry and heat flow with age, *J. Geophys. Res.*, *82*(5), 803–827.
Peel, F. J., C. J. Travis, and J. R. Hossack (1995), Genetic structural provinces and salt tectonics of the cenozoic offshore U.S. Gulf of Mexico: A preliminary analysis, in *Salt tectonics: A global perspective:AAPG Memoir 65,* chap. 7, edited by M. P. A. Jackson, D. G. Roberts, and S. Snelson, pp. 153–175, AAPG, Tulsa, Okla.
Pekeris, C. L. (1935), Thermal convection in the interior of the Earth, *Geophys. J.*, *3*(8), 343–367.
Phipps Morgan, J., W. J. Morgan, Y.-S. Zhang, and W. H. F. Smith (1995), Observational hints for a plume-fed, suboceanic asthenosphere and its role in mantle convection, *J. Geophys. Res.*, *100*(B7), 12,753–12,767, doi:10.1029/95JB00041.
Picard, R. R., and R. D. Cook (1984), Cross-validation of regression models, *J. Am. Stat. Assoc.*, *79*(387), 575–583, doi:10.1080/01621459.1984.10478083.
Pickup, S. L. B., R. B. Whitmarsh, C. M. R. Fowler, and T. J. Reston (1996), Insight into the nature of the ocean-continent transition off West-Iberia from a deep-multichannel seismic reflection profile, *Geology*, *24*(12), 1079–1082, doi:10.1130/0091-7613(1996)024<1079.
Pim, J., C. Peirce, A. B. Watts, I. Grevemeyer, and A. Krabbenhoeft (2008), Crustal structure and origin of the Cape Verde Rise, *Earth Planet. Sci. Lett.*, *272*, 422–428, doi:10.1016/j.epsl.2008.05.012.
Pin, Y., Z. Di, and L. Zhaoshu (2001), A crustal structure profile across the northern continental margin of the South China Sea, *Tectonophysics*, *338*, 1–21, doi:10.1016/S0040-1951(01)00062-2.
Pindell, J. L., and L. Kennan (2009), Tectonic evolution of the Gulf of Mexico, Caribbean and northern South America in the mantle reference frame: An update, *Geol. Soc. London Spec. Publ.*, *328*, 1–55, doi:10.1144/SP328.1.
Planert, L., E. R. Flueh, and T. J. Reston (2009), Along- and across-axis variations in crustal thickness and structure at the Mid-Atlantic Ridge at 5°S obtained from wide-angle seismic tomography: Implications for ridge segmentation, *J. Geophys. Res.*, *114*, B09102, doi:10.1029/2008JB006103.
Planert, L., H. Kopp, E. Lueschen, C. Mueller, E. R. Flueh, A. Shulgin, Y. Djajadihardja, and A. Krabbenhoeft (2010), Lower plate structure and upper plate deformational segmentation at the Sunda-Banda arc transition, Indonesia, *J. Geophys. Res.*, *115*, B08107, doi:10.1029/2009JB006713.
Potts, C. G., A. J. Calvert, and R. S. White (1986), Crustal structure of Atlantic fracture zones—III. The Tydeman fracture zone, *Geophys. J. R. Aston. Soc.*, *86*, 909–942.
Prada, M., V. Sallares, C. R. Ranero, M. G. Vendrell, I. Grevemeyer, N. Zitellini, and R. de Franco (2014), Seismic structure of the Central Tyrrhenian basin: Geophysical constraints on the nature of the main crustal domains, *J. Geophys. Res. Solid Earth*, *119*, 52–70, doi:10.1002/2013JB010527.
Pratt, J. H. (1855), On the attraction of the Himalaya Mountains, and of the elevated regions beyond them, upon the plumb-line in India, *Philos. Trans. R. Soc.*, *145*, 53–100.
Priestley, K., and D. P. McKenzie (2013), The relationship between shear wave velocity, temperature, attenuation and viscosity in the shallow part of the mantle, *Earth Planet. Sci. Lett.*, *381*, 78–91.
Raitt, R. W. (1956), Seismic-refraction studies of the Pacific Ocean Basin. Part I: Crustal thickness of the central equatorial Pacific, *Bull. Geol. Soc. Am.*, *67*(12), 1623–1640, doi:10.1130/0016-7606(1956)67.
Ranero, C. R., and V. Sallarès (2004), Geophysical evidence for hydration of the crust and mantle of the Nazca Plate during bending at the north Chile trench, *Geology*, *32*(7), 549–552, doi:10.1130/G20379.1.
Ranero, C. R., T. J. Reston, I. Belykh, and H. Gnibidenko (1997), Reflective oceanic crust formed at a fast-spreading center in the Pacific, *Geology*, *25*(6), 499–502, doi:10.1130/0091-7613(1997)025<0499:ROCFAA>2.3.CO;2.
Ranero, C. R., J. Phipps Morgan, K. McIntosh, and C. Reichert (2003), Bending-related faulting and mantle serpentinization at the Middle America trench, *Nature*, *425*, 367–373, doi:10.1038/nature01961.
Raum, T., R. Mjelde, P. Digranes, H. Shimamura, H. Shiobara, S. Kodaira, G. Haatvedt, N. Sørenes, and T. Thorbjørnsen (2002), Crustal structure of the southern part of the Vøring Basin, mid-Norway margin, from wide-angle seismic and gravity data, *Tectonophysics*, *355*, 99–126, doi:10.1016/S0040-1951(02)00136-1.
Raum, T., R. Mjelde, H. Shimamura, Y. Murai, E. Brastein, R. Karpuz, K. Kravik, and H. Kolstø (2006), Crustal structure and evolution of the southern Vøring Basin and Vøring Transform Margin, NE Atlantic, *Tectonophysics*, *415*, 167–202, doi:10.1016/j.tecto.2005.12.008.
Rebesco, M., R. D. Larter, A. Camerlenghi, and P. F. Barker (1996), Giant sediment drifts on the continental rise west of the Antarctic Peninsula, *Geo-Mar. Lett.*, *16*, 65–75, doi:10.1007/BF02202600.
Reid, I., and H. R. Jackson (1997), Crustal structure of northern Baffin Bay: Seismic refraction results and tectonic implications, *J. Geophys. Res.*, *102*(B1), 523–542, doi:10.1029/96JB02656.
Richards, F. D., M. J. Hoggard, and N. J. White (2016), Cenozoic epeirogeny of the Indian peninsula, *Geochem. Geophys. Geosyst.*, *17*, 4920–4954, doi:10.1002/2016GC006545.
Rickers, F., A. Fichtner, and J. Trampert (2013), The Iceland-Jan Mayen plume system and its impact on mantle dynamics in the North Atlantic region: Evidence from full-waveform inversion, *Earth Planet. Sci. Lett.*, *367*, 39–51, doi:10.1016/j.epsl.2013.02.022.
Ritzmann, O., W. Jokat, R. Mjelde, and H. Shimamura (2002), Crustal structure between the Knipovich Ridge and the Van Mijenfjorden (Svalbard), *Mar. Geophys. Res.*, *23*, 379–401, doi:10.1023/B:MARI.0000018168.89762.a4.
Ritzmann, O., W. Jokat, W. Czuba, A. Guterch, R. Mjelde, and Y. Nishimura (2004), A deep seismic transect from Hovgård Ridge to northwestern Svalbard across the continental-ocean transition: A sheared margin study, *Geophys. J. Int.*, *157*, 683–702, doi:10.1111/j.1365-246X.2004.02204.x.
Ritzwoller, M. H., N. M. Shapiro, and G. M. Leahy (2003), A resolved mantle anomaly as the cause of the Australian-Antarctic Discordance, *J. Geophys. Res.*, *108*(B12), 2559, doi:10.1029/2003JB002522.
Roberts, G. G., and N. J. White (2010), Estimating uplift rate histories from river profiles using African examples, *J. Geophys. Res.*, *115*, B02406, doi:10.1029/2009JB006692.
Rodger, M., A. B. Watts, C. Greenroyd, C. Peirce, and R. Hobbs (2006), Evidence for unusually thin oceanic crust and strong mantle beneath the Amazon Fan, *Geology*, *34*(12), 1081–1084, doi:10.1130/G22966A.1.
Roland, E., D. Lizarralde, J. J. McGuire, and J. A. Collins (2012), Seismic velocity constraints on the material properties that control earthquake behavior at the Quebrada-Discovery-Gofar transform faults, East Pacific Rise, *J. Geophys. Res.*, *117*, B11102, doi:10.1029/2012JB009422.

Rossetti, D. F., F. H. R. Bezerra, and J. M. L. Dominguez (2013), Late Oligocene-Miocene transgressions along the equatorial and eastern margins of Brazil, *Earth Sci. Rev.*, *123*, 87–112, doi:10.1016/j.earscirev.2013.04.005.

Rovere, A., P. J. Hearty, J. Austermann, J. X. Mitrovica, J. Gale, R. Moucha, A. M. Forte, and M. E. Raymo (2015), Mid-Pliocene shorelines of the U.S. Atlantic Coastal Plain—An improved elevation database with comparison to Earth model predictions, *Earth Sci. Rev.*, *145*, 117–131, doi:10.1016/j.earscirev.2015.02.007.

Rovere, M., C. R. Ranero, R. Sartori, L. Torelli, and N. Zitellini (2004), Seismic images and magnetic signature of the Late Jurassic to Early Cretaceous Africa-Eurasia plate boundary off SW Iberia, *Geophys. J. Int.*, *158*, 554–568, doi:10.1111/j.1365-246X.2004.02339.x.

Rowan, M. G., F. J. Peel, and B. C. Vendeville (2004), Gravity-driven fold belts on passive margins, in *Thrust Tectonics and Hydrocarbon Systems: AAPG Memoir*, vol. 82, edited by K. R. McClay, pp. 157–182, AAPG, Tulsa, Okla.

Sage, F., B. Pontoise, J. Mascle, C. Basile, and L. Arnould (1997), Crustal structure and ocean-continent transition at marginal ridge: The Côte d'Ivoire-Ghana marginal ridge, *Geo-Mar. Lett.*, *17*, 40–48, doi:10.1007/PL00007206.

Sage, F., C. Basile, J. Mascle, B. Pontoise, and R. B. Whitmarsh (2000), Crustal structure of the continent-ocean transition off the Côte d'Ivoire-Ghana margin: Implications for thermal exchanges across the paleotransform boundary, *Geophys. J. Int.*, *143*, 662–678.

Sallarès, V., P. Charvis, E. R. Flueh, and J. Bialas (2003), Seismic structure of Cocos and Malpelo Volcanic Ridges and implications for hot spot-ridge interaction, *J. Geophys. Res.*, *108*(B12), 2564, doi:10.1029/2003JB002431.

Sandwell, D. T., R. D. Muller, W. H. F. Smith, E. Garcia, and R. Francis (2014), New global marine gravity model from CryoSat-2 and Jason-1 reveals buried tectonic structure, *Science*, *346*(6205), 65–67, doi:10.1126/science.1258213.

Schaeffer, A. J., and S. Lebedev (2013), Global shear speed structure of the upper mantle and transition zone, *Geophys. J. Int.*, *194*, 417–449, doi:10.1093/gji/ggt095.

Scherwath, M., E. Contreras-Reyes, E. R. Flueh, I. Grevemeyer, A. Krabbenhoeft, C. Papenberg, C. J. Petersen, and R. W. Weinrebe (2009), Deep lithospheric structures along the southern central Chile margin from wide-angle *P*-wave modelling, *Geophys. J. Int.*, *179*, 579–600, doi:10.1111/j.1365-246X.2009.04298.x.

Schnabel, M., D. Franke, M. Engels, K. Hinz, S. Neben, V. Damm, S. Grassmann, H. Pelliza, and P. R. Dos Santos (2008), The structure of the lower crust at the Argentine continental margin, South Atlantic at 44°S, *Tectonophysics*, *454*, 14–22, doi:10.1016/j.tecto.2008.01.019.

Schroeder, W. (1984), The empirical age-depth relation and depth anomalies in the Pacific Ocean Basin, *J. Geophys. Res.*, *89*(B12), 9873–9883, doi:10.1029/JB089iB12p09873.

Sclater, J. G., and J. Francheteau (1970), The implications of terrestrial heat flow observations on current tectonic and geochemical models of the crust and upper mantle of the Earth, *Geophys. J. R. Aston. Soc.*, *20*, 509–537.

Scott, C. L., D. J. Shillington, T. A. Minshull, R. A. Edwards, P. J. Brown, and N. J. White (2009), Wide-angle seismic data reveal extensive overpressures in the Eastern Black Sea Basin, *Geophys. J. Int.*, *178*, 1145–1163, doi:10.1111/j.1365-246X.2009.04215.x.

Seher, T., W. C. Crawford, S. C. Singh, M. Cannat, V. Combier, and D. Dusunur (2010), Crustal velocity structure of the Lucky Strike segment of the Mid-Atlantic Ridge at 37°N from seismic refraction measurements, *J. Geophys. Res.*, *115*, B03103, doi:10.1029/2009JB006650.

Shillington, D. J., W. S. Holbrook, H. J. A. Van Avendonk, B. E. Tucholke, J. R. Hopper, K. E. Louden, H. C. Larsen, and G. T. Nunes (2006), Evidence for asymmetric nonvolcanic rifting and slow incipient oceanic accretion from seismic reflection data on the Newfoundland margin, *J. Geophys. Res.*, *111*, B09402, doi:10.1029/2005JB003981.

Shillington, D. J., N. J. White, T. A. Minshull, G. R. H. Edwards, S. M. Jones, R. A. Edwards, and C. L. Scott (2008), Cenozoic evolution of the eastern Black Sea: A test of depth-dependent stretching models, *Earth Planet. Sci. Lett.*, *265*, 360–378, doi:10.1016/j.epsl.2007.10.033.

Shillington, D. J., A. Bécel, M. R. Nedimović, H. Kuehn, S. C. Webb, G. A. Abers, K. M. Keranen, J. Li, M. Delescluse, and G. A. Mattei-Salicrup (2015), Link between plate fabric, hydration and subduction zone seismicity in Alaska, *Nat. Geosci.*, *8*(12), 961–964, doi:10.1038/ngeo2586.

Shinohara, M., T. Fukano, T. Kanazawa, E. Araki, K. Suyehiro, M. Mochizuki, K. Nakahigashi, T. Yamada, and K. Mochizuki (2008), Upper mantle and crustal seismic structure beneath the Northwestern Pacific Basin using a seafloor borehole broadband seismometer and ocean bottom seismometers, *Phys. Earth Planet. Inter.*, *170*, 95–106, doi:10.1016/j.pepi.2008.07.039.

Shipley, T., L. Gahagan, K. Johnson, and M. Davis (2005), Seismic Data Centre, Univ. of Texas Inst. for Geophys. [Available at www-udc.ig.utexas.edu/sdc.]

Shor, G. G. (2013), Seismic refraction profile in Coral Sea, *Science*, *158*(3803), 911–913.

Shor, G. G., and D. J. Fornari (1976), Seismic refraction measurements in the Kamchatka Basin, Western Mediterranean Sea, *J. Geophys. Res.*, *81*(29), 5260–5266.

Shor, G. G., P. Dehlinger, H. K. Kirk, and W. S. French (1968), Seismic refraction studies off Oregon and Northern California, *J. Geophys. Res.*, *73*(6), 2175–2194.

Shor, G. G., H. K. Kirk, and H. W. Menard (1971), Crustal structure of the Melanesian Area, *J. Geophys. Res.*, *76*(11), 2562–2586, doi:10.1029/JB076i011p02562.

Singh, S. C., H. Carton, A. S. Chauhan, S. Androvandi, A. Davaille, J. Dyment, M. Cannat, and N. D. Hananto (2011), Extremely thin crust in the Indian Ocean possibly resulting from Plume-Ridge Interaction, *Geophys. J. Int.*, *184*, 29–42, doi:10.1111/j.1365-246X.2010.04823.x.

Smallwood, J. R., and C. E. Gill (2002), The rise and fall of the Faroe-Shetland Basin: Evidence from seismic mapping of the Balder Formation, *J. Geol. Soc.*, *159*, 627–630, doi:10.1144/0016-764902-064.

Smallwood, J. R., R. S. White, and T. A. Minshull (1995), Sea-floor spreading in the presence of the Iceland plume: The structure of the Reykjanes Ridge at 61°40'N, *J. Geol. Soc.*, *152*, 1023–1029, doi:10.1144/GSL.JGS.1995.152.01.24.

Smith, W. H. F., and D. T. Sandwell (1997), Global sea floor topography from satellite altimetry and ship depth soundings, *Science*, *277*(5334), 1956–1962, doi:10.1126/science.277.5334.1956.

Soule, D., W. S. D. Wilcock, D. R. Toomey, E. E. E. Hooft, and R. T. Weekly (2016), Near-axis crustal structure and thickness of the Endeavour Segment, Juan de Fuca Ridge, *Geophys. Res. Lett.*, *43*, 5688–5695, doi:10.1002/2016GL068182.

Spasojević, S., L. Liu, M. Gurnis, and R. D. Müller (2008), The case for dynamic subsidence of the U.S. East Coast since the Eocene, *Geophys. Res. Lett.*, *35*, L08305, doi:10.1029/2008GL033511.

Stein, C., and S. Stein (1992), A model for the global variation in oceanic depth and heat flow with lithospheric age, *Nature*, *359*(9), 123–139.

Steinberger, B. (2007), Effects of latent heat release at phase boundaries on flow in the Earth's mantle, phase boundary topography and dynamic topography at the Earth's surface, *Phys. Earth Planet. Inter.*, *164*, 2–20, doi:10.1016/j.pepi.2007.04.021.

Steinberger, B. (2016), Topography caused by mantle density variations: Observation-based estimates and models derived from tomography and lithosphere thickness, *Geophys. J. Int.*, *205*, 604–621, doi:10.1093/gji/ggw040.

Steinberger, B., H. Schmeling, and G. Marquart (2001), Large-scale lithospheric stress field and topography induced by global mantle circulation, *Earth Planet. Sci. Lett.*, *186*, 75–91, doi:10.1016/S0012-821X(01)00229-1.

Stephenson, S. N., G. G. Roberts, M. J. Hoggard, and A. C. Whittaker (2014), A Cenozoic uplift history of Mexico and its surroundings from longitudinal river profiles, *Geochem. Geophys. Geosyst.*, *15*, 4734–4758, doi:10.1002/2014GC005425.

Storey, M., R. A. Duncan, and C. Tegner (2007), Timing and duration of volcanism in the North Atlantic Igneous Province: Implications for geodynamics and links to the Iceland hotspot, *Chem. Geol.*, *241*, 264–281, doi:10.1016/j.chemgeo.2007.01.016.

Suckro, S. K., K. Gohl, T. Funck, I. Heyde, A. Ehrhardt, B. Schreckenberger, J. Gerlings, V. Damm, and W. Jokat (2012), The crustal structure of southern Baffin Bay: Implications from a seismic refraction experiment, *Geophys. J. Int.*, *190*, 37–58, doi:10.1111/j.1365-246X.2012.05477.x.

Sutton, G. H., G. L. Maynard, and D. M. Hussong (1971), Widespread occurrence of a high-velocity basal layer in the Pacific crust found with repetitive sources and sonobuoys, in *The Structure and Physical Properties of the Earth's Crust*, edited by J. G. Heacock, pp. 193–210, AGU, Washington, D. C.

Sykes, T. J. S. (1996), A correction for sediment load upon the ocean floor: Uniform versus varying sediment density estimations-implications for isostatic correction, *Mar. Geol.*, *133*, 35–49, doi:10.1016/0025-3227(96)00016-3.

Takahashi, N., K. Suyehiro, and M. Shinohara (1998), Implications from the seismic crustal structure of the northern Izu-Bonin arc, *Island Arc*, *7*, 383–394.

Thinon, I., L. Matias, J. Rehault, A. Hirn, L. Fidalgo-Gonzalez, and F. Avedik (2003), Deep structure of the Armorican Basin (Bay of Biscay): A review of Norgasis seismic reflection and refraction data, *J. Geol. Soc.*, *160*, 99–116, doi:10.1144/0016-764901-103.

Trehu, A. (1991), Tracing the subducted oceanic-crust beneath the central California continental-margin: Results from ocean bottom seismometers deployed during the 1986 Pacific gas and electric EDGE experiment, *J. Geophys. Res.*, *96*(B4), 6493–6506, doi:10.1029/90JB00494.

Tréhu, A. M., A. Ballard, L. M. Dorman, J. F. Gettrust, K. D. Klitgord, and A. Schreiner (1989), Structure of the lower crust beneath the Carolina Trough, U.S. Atlantic Continental Margin, *J. Geophys. Res.*, *94*(B8), 10,585–10,600, doi:10.1029/JB094iB08p10585.

Tsikalas, F., O. Eldholm, and J. I. Faleide (2005), Crustal structure of the Lofoten Vesterålen continental margin, off Norway, *Tectonophysics*, *404*, 151–174, doi:10.1016/j.tecto.2005.04.002.

Tsuji, T., Y. Nakamura, H. Tokuyama, M. F. Coffin, and K. Koda (2007), Oceanic crust and Moho of the Pacific Plate in the eastern Ogasawara Plateau region, *Island Arc*, *16*, 361–373, doi:10.1111/j.1440-1738.2007.00589.x.

Tucholke, B. E., R. E. Houtz, and W. J. Ludwig (1982), Sediment thickness and depth to basement in Western North Atlantic Ocean Basin, *Am. Assoc. Pet. Geol. Bull.*, *66*(9), 1384–1395, doi:10.1306/03B5A7AA-16D1-11D7-8645000102C1865D.

Tucholke, B. E., D. S. Sawyer, and J.-C. Sibuet (2007), Breakup of the Newfoundland-Iberia rift, in *Imaging, Mapping and Modelling Continental Lithosphere Extention and Breakup*, edited by G. D. Karner, G. Manatschal, and L. M. Pinheiro, *Geol. Soc. London, Spec. Publ., 282*, 9–46, doi:10.1144/SP282.2.

Turcotte, D. L., and E. R. Oxburgh (1969), Convection in a mantle with variable physical properties, *J. Geophys. Res.*, *74*(6), 1458–1474, doi:10.1029/JB074i006p01458.

Turcotte, D. L., and G. Schubert (2002), *Geodynamics*, 2nd ed., Cambridge Univ. Press, Cambridge, U. K.

Turner, I. M., C. Peirce, and M. C. Sinha (1999), Seismic imaging of the axial region of the Valu Fa Ridge, Lau Basin—The accretionary processes of an intermediate back-arc spreading ridge, *Geophys. J. Int.*, *138*, 495–519, doi:10.1046/j.1365-246X.1999.00883.x.

Underhill, J. R. (2001), Controls on the genesis and prospectivity of Paleogene palaeogeomorphic traps, East Shetland Platform, UK North Sea, *Mar. Pet. Geol.*, *18*, 259–281, doi:10.1016/S0264-8172(00)00067-2.

Van Avendonk, H. J. A., A. J. Harding, J. A. Orcutt, and J. S. McClain (2001), Contrast in crustal structure across the Clipperton transform fault from travel time tomography, *J. Geophys. Res.*, *106*(B6), 10,961–10,981, doi:10.1029/2000JB900459.

Van Avendonk, H. J. A., W. S. Holbrook, G. T. Nunes, D. J. Shillington, B. E. Tucholke, K. E. Louden, H. C. Larsen, and J. R. Hopper (2006), Seismic velocity structure of the rifted margin of the eastern Grand Banks of Newfoundland, Canada, *J. Geophys. Res.*, *111*, B11404, doi:10.1029/2005JB004156.

Vogt, P. R. (1971), Asthenosphere motion recorded by the ocean floor south of Iceland, *Earth Planet. Sci. Lett.*, *13*, 153–160, doi:10.1016/0012-821X(71)90118-X.

Vogt, P. R., and W.-Y. Jung (2007), Origin of the Bermuda volcanoes and the Bermuda Rise: History, observations, models, and puzzles, *Geol. Soc. Am. Spec. Pap.*, *430*, 553–591.

Vogt, U., J. Makris, B. M. O'Reilly, F. Hauser, P. W. Readman, A. W. B. Jacob, and P. M. Shannon (1998), The Hatton Basin and continental margin: Crustal structure from wide-angle seismic and gravity data, *J. Geophys. Res.*, *103*(B6), 12,545–12,566, doi:10.1029/98JB00604.

Voss, M., and W. Jokat (2007), Continent-ocean transition and voluminous magmatic underplating derived from *P*-wave velocity modelling of the East Greenland continental margin, *Geophys. J. Int.*, *170*, 580–604, doi:10.1111/j.1365-246X.2007.03438.x.

Walford, H. L., and N. J. White (2005), Constraining uplift and denudation of west African continental margin by inversion of stacking velocity data, *J. Geophys. Res.*, *110*, B04403, doi:10.1029/2003JB002893.

Walker, R. T., M. Telfer, R. L. Kahle, M. W. Dee, B. Kahle, J.-L. Schwenninger, R. A. Sloan, and A. B. Watts (2016), Rapid mantle-driven uplift along the Angolan margin in the late Quaternary, *Nat. Geosci.*, *9*(11), 909–914, doi:10.1038/ngeo2835.

Walther, C., and E. R. Flueh (2002), Remnant of the ancient Farallon Plate breakup: A low-velocity body in the lower oceanic crust off Nicoya Peninsula, Costa Rica—Evidence from wide-angle seismics, *Geophys. Res. Lett.*, *29*(19), 1939, doi:10.1029/2002GL015026.

Walther, C. H. E., E. R. Flueh, C. R. Ranero, R. Von Huene, and W. Strauch (2000), Crustal structure across the Pacific margin of Nicaragua: Evidence for ophiolitic basement and a shallow mantle sliver, *Geophys. J. Int.*, *141*, 759–777, doi:10.1046/j.1365-246X.2000.00134.x.

Wang, T. K., M.-K. Chen, C.-S. Lee, and K. Xia (2006), Seismic imaging of the transitional crust across the northeastern margin of the South China Sea, *Tectonophysics*, *412*, 237–254, doi:10.1016/j.tecto.2005.10.039.

Watremez, L., S. Leroy, S. Rouzo, E. D'Acremont, P. Unternehr, C. Ebinger, F. Lucazeau, and A. Al-Lazki (2011), The crustal structure of the north-eastern Gulf of Aden continental margin: Insights from wide-angle seismic data, *Geophys. J. Int.*, *184*, 575–594, doi:10.1111/j.1365-246X.2010.04881.x.

Watts, A. B. (2001), *Isostasy and Flexure of the Lithosphere*, Cambridge Univ. Press, Cambridge, U. K.

Watts, A. B., and E. B. Burov (2003), Lithospheric strength and its relationship to the elastic and seismogenic layer thickness, *Earth Planet. Sci. Lett.*, *213*, 113–131, doi:10.1016/S0012-821X(03)00289-9.

Watts, A. B., and N. M. Ribe (1984), On geoid heights and flexure of the lithosphere at seamounts, *J. Geophys. Res.*, *89*(B13), 11,152–11,170, doi:10.1029/JB089iB13p11152.

Watts, A. B., J. H. Bodine, and N. M. Ribe (1980), Observations of flexure and the geological evolution of the Pacific Ocean basin, *Nature*, *283*, 532–537, doi:10.1038/283532a0.

Watts, A. B., D. P. McKenzie, B. E. Parsons, and M. Roufosse (1985a), The relationship between gravity and bathymetry in the Pacific Ocean, *Geophys. J. R. Aston. Soc.*, *83*, 263–298, doi:10.1111/j.1365-246X.1985.tb05166.x.

Watts, A. B., U. S. ten Brink, P. Buhl, and T. M. Brocher (1985b), A multichannel seismic study of lithospheric flexure across the Hawaiian—Emperor seamount chain, *Nature*, *315*, 105–111, doi:10.1038/315105a0.

Watts, A. B., M. Rodger, C. Peirce, C. J. Greenroyd, and R. W. Hobbs (2009), Seismic structure, gravity anomalies, and flexure of the Amazon continental margin, NE Brazil, *J. Geophys. Res.*, *114*, B07103, doi:10.1029/2008JB006259.
Weigel, W., and I. Grevemeyer (1999), The Great Meteor seamount: Seismic structure of a submerged intraplate volcano, *Geodynamics*, *28*, 27–40, doi:10.1016/S0264-3707(98)00030-1.
Weigel, W., et al. (1995), Investigations of the East Greenland continental margin between 70° and 72°N by deep seismic sounding and gravity studies, *Mar. Geophys. Res.*, *17*, 167–199.
Weir, N. R. W., R. S. White, B. Brandsdóttir, P. Einarsson, H. Shimamura, and H. Shiobara (2001), Crustal structure of the northern Reykjanes Ridge and Reykjanes Peninsula, southwest Iceland, *J. Geophys. Res.*, *106*(B4), 6347–6368, doi:10.1029/2000JB900358.
Weissel, J. K., and A. B. Watts (1979), Tectonic evolution of the Coral Sea Basin, *J. Geophys. Res.*, *84*(B9), 4572–4582, doi:10.1029/JB084iB09p04572.
Wessel, P., W. H. F. Smith, R. Scharroo, J. Luis, and F. Wobbe (2013), Generic mapping tools: Improved version released, *EOS Trans. AGU*, *94*(45), 409–410, doi:10.1002/2013EO450001.
Wheeler, P., and N. White (2000), Quest for dynamic topography: Observations from Southeast Asia, *Geology*, *28*(11), 963–966, doi:10.1130/0091-7613(2000)28<963:QFDTOF>2.0.CO;2.
Wheeler, P., and N. J. White (2002), Measuring dynamic topography: An analysis of Southeast Asia, *Tectonics*, *21*(5), 1040, doi:10.1029/2001.
White, R. S., and D. P. McKenzie (1989), Magmatism at rift zones: The generation of volcanic continental margins, *J. Geophys. Res.*, *94*(B6), 7685–7729.
White, R. S., and L. K. Smith (2009), Crustal structure of the Hatton and the conjugate east Greenland rifted volcanic continental margins, NE Atlantic, *J. Geophys. Res.*, *114*, B02305, doi:10.1029/2008JB005856.
White, R. S., D. P. McKenzie, and R. K. O'Nions (1992), Oceanic crustal thickness from seismic measurements and rare earth element inversions, *J. Geophys. Res.*, *97*(B13), 19,683–19,715.
White, R. S., J. W. Bown, and J. R. Smallwood (1995), The temperature of the Iceland plume and origin of outward-propagating V-shaped ridges, *J. Geol. Soc.*, *152*(6), 1039–1045, doi:10.1144/GSL.JGS.1995.152.01.26.
Whitmarsh, R. B., R. S. White, S. J. Horsefield, J.-C. Sibuet, M. Recq, and V. Louvel (1996), The ocean-continent boundary off the western continental margin of Iberia: Crustal structure west of Galicia Bank, *J. Geophys. Res.*, *101*(B12), 28,291–28,314, doi:10.1029/96JB02579.
Whittaker, J. M., R. D. Mller, and M. Gurnis (2010), Development of the Australian-Antarctic depth anomaly, *Geochem. Geophys. Geosyst.*, *11*, Q11006, doi:10.1029/2010GC003276.
Whittaker, J. M., A. Goncharov, S. E. Williams, R. D. Müller, and G. Leitchenkov (2013), Global sediment thickness data set updated for the Australian-Antarctic Southern Ocean, *Geochem. Geophys. Geosyst.*, *14*, 3297–3305, doi:10.1002/ggge.20181.
Wilson, P. G., J. P. Turner, and G. K. Westbrook (2003), Structural architecture of the ocean-continent boundary at an oblique transform margin through deep-imaging seismic interpretation and gravity modelling: Equatorial Guinea, West Africa, *Tectonophysics*, *374*, 19–40, doi:10.1016/S0040-1951(03)00326-3.
Winterbourne, J. R., A. G. Crosby, and N. J. White (2009), Depth, age and dynamic topography of oceanic lithosphere beneath heavily sedimented Atlantic margins, *Earth Planet. Sci. Lett.*, *287*, 137–151, doi:10.1016/j.epsl.2009.08.019.
Winterbourne, J. R., N. J. White, and A. G. Crosby (2014), Accurate measurements of residual topography from the oceanic realm, *Tectonics*, *33*, 982–1015, doi:10.1002/2013TC003372.
Wobbe, F., A. Lindeque, and K. Gohl (2014), Anomalous South Pacific lithosphere dynamics derived from new total sediment thickness estimates off the West Antarctic margin, *Global Planet. Change*, *123*, 139–149, doi:10.1016/j.gloplacha.2014.09.006.
Worzel, J. L., and J. S. Watkins (1973), Evolution of the northern Gulf Coast deduced from geophysical data, *Gulf Coast Assoc. Geol. Soc. Trans.*, *23*, 84–91.
Wu, Y., K. E. Louden, T. Funck, H. R. Jackson, and S. A. Dehler (2006), Crustal structure of the central Nova Scotia margin off Eastern Canada, *Geophys. J. Int.*, *166*, 878–906, doi:10.1111/j.1365-246X.2006.02991.x.
Wu, Z., J. Li, A. Ruan, H. Lou, W. Ding, X. Niu, and X. Li (2012), Crustal structure of the northwestern sub-basin, South China Sea: Results from a wide-angle seismic experiment, *Sci. China Earth Sci.*, *55*(1), 159–172, doi:10.1007/s11430-011-4324-9.
Wyllie, M. R. J., A. R. Gregory, and L. W. Gardner (1956), Elastic wave velocities in heterogeneous and porous media, *Geophysics*, *21*(1), 41–70.
Xie, X. N., R. D. Müller, S. Li, Z. Gong, and B. Steinberger (2006), Origin of anomalous subsidence along the Northern South China Sea margin and its relationship to dynamic topography, *Mar. Pet. Geol.*, *23*, 745–765, doi:10.1016/j.marpetgeo.2006.03.004.
Yang, T., and M. Gurnis (2016), Dynamic topography, gravity and the role of lateral viscosity variations from inversion of global mantle flow, *Geophys. J. Int.*, *207*, 1186–1202, doi:10.1093/gji/ggw335.
Yoshii, T., W. J. Ludwig, N. Den, S. Murauchi, M. Ewing, H. Hotta, P. Buhl, T. Asanuma, and N. Sakajiri (1973), Structure of Southwest Japan Margin off Shikoku, *J. Geophys. Res.*, *78*(14), 2517–2525, doi:10.1029/JB078i014p02517.
Yuen, D. A., D. M. Reuteler, S. Balachandar, V. Steinbach, A. V. Malevsky, and J. J. Smedsmo (1994), Various influences on three-dimensional mantle convection with phase transitions, *Phys. Earth Planet. Inter.*, *86*, 185–203, doi:10.1016/0031-9201(94)05068-6.
Zelt, C. A., and R. B. Smith (1992), Seismic traveltime inversion for 2-D crustal velocity structure, *Geophys. J. Int.*, *108*, 16–34.
Zhong, S., M. Ritzwoller, N. Shapiro, W. Landuyt, J. Huang, and P. Wessel (2007), Bathymetry of the Pacific Plate and its implications for thermal evolution of lithosphere and mantle dynamics, *J. Geophys. Res.*, *112*, B06412, doi:10.1029/2006JB004628.
Zonenshain, L. P., and X. Pichon (1986), Deep basins of the Black Sea and Caspian Sea as remnants of Mesozoic back-arc basins, *Tectonophysics*, *123*, 181–211, doi:10.1016/0040-1951(86)90197-6.

Erratum

In the originally published version of this article, several instances of text and figures were incorrectly typeset. The following have since been corrected and this version may be considered the authoritative version of record.

In section 6, geoid was changed to geoid height anomalies.

Figure 10 was replaced with the correct version.

In Figure 10 caption, band-pass ($9000 > \lambda > 730$ km) was changed to low-pass (>730 km).

Figure 11 was replaced with the correct version.

In Figure 11 caption, low-pass (>730 km) was changed to band-pass (9000>λ>730 km), and Z = 35 ± 10 mGal km^{-1} was changed to Z = 30 ± 10 mGal km^{-1}.

Figure 12 was replaced with the correct version.

In Figure 12 caption, Z = 35 ± 10 mGal km^{-1} was replaced with Z = 30 ± 10 mGal km^{-1}.

Figure 13 was replaced with the correct version.

In Figure 13 caption, Z = 35 ± 10 mGal km^{-1} was replaced with Z = 30 ± 10 mGal km^{-1}.

In section 7.3, Z = 35±10mGal/km was replaced with Z = 30±10mGal/km.

In section 7.4, Z = 35 ± 10 mGal km^{-1} was replaced with Z = 30 ± 10 mGal km^{-1}.

Figure 14 was replaced with the correct version.

In Figure 14 caption, band-pass (9000>λ>730 km) was updated with low-pass (>730 km), and Z = 35 ± 10 mGal km^{-1} was replaced with Z = 30 ± 10 mGal km^{-1}.

Figure 15 was replaced with the correct version.

In Figure 15 caption, band-pass (9000>λ>730 km) was updated with low-pass (>730 km).

Figure D1 was replaced with the correct version.

Figure D2 was replaced with the correct version.

In Figure D2 caption, band-pass (9000>λ>730 km) was updated with low-pass (>730 km),

Figure D3 was replaced with the correct version.

In Figure D3 caption, 20 mGal was updated with 10 mGal.